RCA Review

June 1974 Volume 35 No. 2
RCARCI 35(2) 165-330 (1974)

RCA Review, published quarterly in March, June, September and December by RCA Research and Engineering, RCA Corporation, Princeton, New Jersey 08540. Entered as second class matter July 3, 1950 under the Act of March 3, 1879. Second-class postage paid at Princeton, New Jersey, and at additional mailing offices. Effective Jan. 1, 1971, subscription rates as follows: United States and Canada: one year $6.00, two years $10.50, three years $13.50; in other countries, one year $6.40, two years $11.30, three years $14.70. Single copies (except for special issues) up to five years old $3.00.

RCA Review

A technical journal published quarterly by RCA Research and Engineering in cooperation with the subsidiaries and divisions of RCA.

Contents

June 1974 Volume 35 Number 2

An Electronic License Plate for Motor Vehicles

Fred Sterzer
RCA Laboratories, Princeton, N. J. 08540

Abstract—A multi-purpose electronic license plate for use on motor vehicles is proposed. The license plate is compact (~6 × 12 × ½ inch), and its manufacturing cost in large quantities should be only a few dollars. The license plate can be used for the following purposes: (1) electronic identification of vehicles for traffic control, anti-theft protection, automatic toll billing, etc., (2) transmission of messages to and from the vehicle, and (3) cooperative collision-avoidance systems.

1. Introduction

The U.S. transportation system is heavily based on motorized highway vehicles. There are approximately 117 million of these vehicles in the country today traveling over one trillion miles annually. The benefits of our highway system are enormous, but unfortunately we have to pay a heavy price for these benefits. There are over 16 million highway traffic accidents every year resulting in approximately 5 million personal injuries and about 55,000 fatalities; motor vehicles are the major contributors to air pollution in the country, over 2 million motor vehicles are stolen annually, etc.

Electronics can play a major role in reducing or eliminating some

of the disadvantages associated with our present highway transportation system. Several electronics-based innovations that promise major improvements in highway safety, air pollution, and traffic flow are already being put into widespread use. These include seat-belt interlocks, anti-skid brakes, electronic ignition, and computer-controlled traffic signals.

The present paper proposes a new electronic concept with broad implication in such areas as highway safety, traffic control, anti-theft protection, and vehicle inspection. This concept is based on the use of compact, inexpensive electronic license plates mounted on the rear of every motorized highway vehicle. Each license plate provides the following three functions: (1) when electronically interrogated, the license plate responds with a code representing an identifying number assigned to the vehicle to which the plate is attached, (2) the plate is the receiver and transmitter for messages to and from the vehicle, and (3) the plate serves as a transponder for use in cooperative collision-avoidance radars.

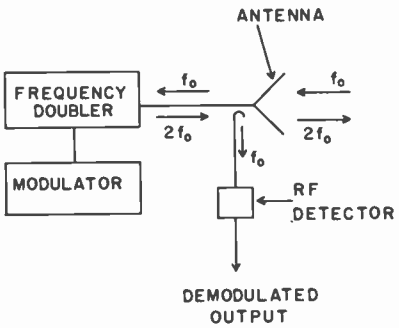

Fig. 1—Block diagram of the electronic license plate.

2. Description of the Electronic License Plate

There are several possible technical approaches to realizing the proposed electronic license plate. The approach described here is based on the work on second-harmonic reflectors by Johnson, Kaplan, Klensch, Rosen, Shefer, and Staras of RCA Laboratories.[1-3] A block diagram of the plate is shown in Fig. 1. The plate consists of the following major components: a printed-circuit antenna covered by a visual display of the license number of the vehicle, a frequency doubler, a modulator, and an rf detector. The manufacturing cost of the plate in multi-million quantities should be of the order of a few dollars.

2.1 The Antenna

Electronic communications between the vehicle and its surroundings takes place at two harmonically related microwave frequencies. Communications from the surroundings to the vehicle is at frequency f_o while communications from the vehicle to its surroundings is at twice this frequency ($2f_o$). From considerations based on antenna size, beam width, rf spectrum allocation, and rf absorption in air, it appears that a frequency of approximately 10 GHz is optimum for f_o.

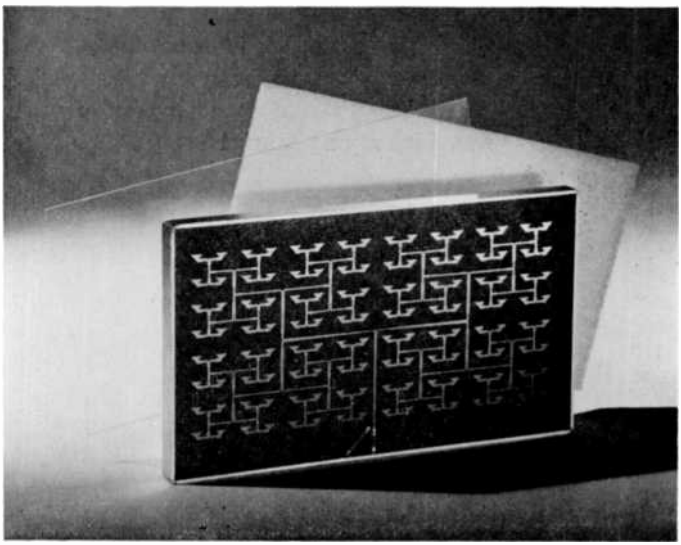

Fig. 2—Photograph of printed-circuit license plate antenna with radome removed. The size of the antenna is 5.7 × 10 inches (courtesy J. Rosen, RCA Laboratories).

Fig. 2 shows a photograph of a printed-circuit antenna suitable for use in the proposed electronic license plate. This antenna, which is approximately the size of a conventional license plate, is sufficiently broadband to be able to handle both incoming 10-GHz and outgoing 20-GHz radiation. The radome for the printed circuit antenna is a sheet of plastic embossed with the license plate of the vehicle, as shown in Fig. 3.

2.2 The Second-Harmonic Generator[1]

The second-harmonic generator consists of a Schottky barrier silicon diode embedded in a circuit that is printed on the same dielectric

board as the antenna. X-band 8-12 GHz radiation received by the antenna is doubled in frequency in the second harmonic generator and the resulting Ku-band 12-24 GHz frequencies are re-radiated by the antenna.

2.3 The Modulator[3]

The modulator is a COS/MOS circuit that generates a binary code representing the identifying number assigned to the vehicle to which the plate is attached, as well as special coded messages. The output of the modulator is an on-off keyed voltage that modulates the bias on the Schottky barrier diode in the second-harmonic generator. Thus, when the license plate is interrogated with a cw X-band signal, the plate responds with a Ku-band signal that is on-off modulated with codes representing the identifying number of the vehicle and the special messages.

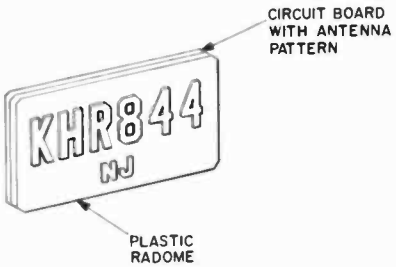

Fig. 3—Printed-circuit antenna with plastic radome. The radome displays the license number of the vehicle.

2.4 The RF Detector

The detector consists of a Schottky barrier silicon diode embedded in a circuit that is printed on the same dielectric board as the antenna. Part of the X-band radiation received by the antenna is sampled by a printed circuit directional coupler and demodulated in the detector.

3. Uses of the Electronic License Plate

In the discussion of the uses of the proposed electronic license plate, it is assumed that every motorized highway vehicle will be required by law to carry such a plate. Most of the important uses of the plate require this to be the case.

3.1 Electronic Vehicle Identification

The identifying number of any vehicle carrying the electronic license plate, as well as additional special codes, can be read electronically by means of interrogators that can be mounted on automobiles, on the side of roads, buried in roadways, etc. A suitable interrogator is described in detail in Ref. [3]. Applications of this feature of the plate include the following:

1. Interrogators spaced throughout a city and connected by means of a communications network to a central office could form the basis for an automatic vehicle monitoring (AVM) system for special vehicles such as buses, police cars, ambulances, trucks, and cabs. The potential social and economic benefits of such an AVM system are very large[4]—improved scheduling of buses, speedier arrival of police cars at the scene of a crime or an accident; more efficient dispatching of ambulances, cabs, trucks; better control of trucks to reduce hijacking;[5] etc.

2. All highway vehicles could be electronically monitored by law-enforcement agencies for stolen vehicles, vehicles with unanswered summonses for traffic violations, etc. The monitoring interrogators would communicate with a computer containing a list of 'wanted' vehicles, and would sound an alarm when a vehicle with a wanted license plate is identified. By equipping the interrogators with a doppler speed sensor, it would be possible to automatically record the identifying number of any vehicle that exceeds by a significant amount the posted speed limit, etc.

3. Entry to certain locations could be automatically restricted to special classes of vehicles that are electronically identified by codes added to their identifying number. For example, parts of downtown areas of a city could be restricted to public transportation vehicles and to police and emergency vehicles during part of each working day, entry to company parking lots could be restricted to employee automobiles, etc.

4. Vehicles with special codes could bypass toll lanes, thus reducing congestion at toll plazas. An interrogation at each toll lane would identify each vehicle as it passes by, the identification number of the vehicle would be recorded, and the owner of the vehicle would be periodically billed for accumulated toll charges.

5. Vehicle inspection stations could be automated to test vehicles to manufacturers' specifications. As a vehicle enters an inspection station, an interrogator would read the identifying number of the vehicle, identify the type and model number of the vehicle from the

identifying number,* and automatically program the inspection equipment to check for compliance with the manufacturers' specifications for the particular type and model vehicle.

3.2 Transmission of Messages to and from the Vehicle

The electronic license plate provides an electronic communications link for sending messages to and from the vehicle. Messages sent to the vehicle must be encoded on the fundamental frequency f_o; messages sent from the vehicle are encoded on the second-harmonic frequency $2f_o$. Outgoing messages are converted to appropriate on-off codes and applied to the doubler diode of the license plate. When the vehicle is interrogated at frequency f_o, the harmonic signal re-radiated from the license plate is coded with the identifying number of the vehicle followed by the coded message.

1. Messages sent to the Vehicle

Messages can be sent to vehicles from X-band transmitters mounted on the roadside or on police cars or other special vehicles. Examples of general traffic safety messages that could be transmitted are warning signals telling the driver that he is driving too fast (exceeding posted speed limit by an unsafe amount; ice, snow, fog, accident, etc., ahead), or that his vehicle is proceeding the wrong way into a one-way street.[6] Messages could also be addressed to certain vehicles or groups of vehicles based on their identifying number, such as warning messages to unauthorized vehicles entering restricted areas, messages to police cars that a speeding vehicle with a particular identifying number passed a short-time ago, etc.

2. Messages sent from the Vehicle

Messages coded on the second harmonic diode of the license plate can be read by roadside or vehicle-mounted interrogators. The most important types of messages that would be sent from vehicles are likely to be distress calls for help.

3.3 Cooperative Harmonic Collision-Avoidance Radar

The cooperative harmonic collision-avoidance radar is a new type of vehicle-mounted radar that shows great promise of being capable of sharply reducing highway accidents, particularly rear-end collisions.[1, 2] This radar eliminates the clutter and blinding problem faced by con-

* The identifying number given to each vehicle will contain in coded form the type and model number of the vehicle.

ventional automotive radars by using a receiver that is tuned to the second harmonic of the transmitted frequency. The harmonic radar therefore "sees" only objects equipped with second-harmonic reflectors such as vehicles carrying the proposed electronic license plate; clutter returns from roadways, highway signs, overpasses, trees, etc., as well as signals emitted from other collision avoidance radars are automatically rejected.

The electronic license plate meets all of the requirements for a second-harmonic reflector to be used in a highway collision-avoidance system based on second-harmonic radars. Thus, once an electronic license plate is in nationwide use, it would become practical to equip highway vehicles with harmonic collision-avoidance radars.

4. Discussion

The economic viability of the electronic license plate concept can be demonstrated by considering just one of the areas that would be affected by the plate, namely, highway safety. As stated in the introduction, there are over 16 million traffic accidents annually in the United States resulting in approximately 5 million personal injuries and about 55,000 fatalities. The total annual cost to society of these accidents is about 50 billion dollars,[7] i.e., over $400 annually per motorized highway vehicle. Operation of vehicles at excessive speeds (including 'speeds too fast for conditions') and rear-end collisions are each responsible for accidents causing losses of approximately 10 billion dollars annually, or over $80 annually per vehicle. The estimated annual cost of operating an electronic license plate system is about 2 billion dollars (~$3/vehicle/year for the license plate, ~$7/vehicle/year for the radar, and ~$7/vehicle/year for the highway interrogation and warning system). Thus, an electronic license plate system would be cost effective if it reduced the losses due to all highway accidents by more than 4%, or the losses due to either speeding or rear-end collisions by more than 20%. Use of just the collision avoidance feature of the plate should reduce losses due to rear-end collisions by more than 20%.[1] Taken together with the other safety-related features of the plate (see Table 1), the overall reduction in losses is likely to exceed 4% by a large amount.

It can be argued that even if the electronic license plate system did indeed offer large economic benefits, such a system should not be implemented because it would represent an infringement on the civil liberties of the drivers of motorized highway vehicles. This argument fails to take into account that motorized highway vehicles have

Table 1—Safety related features of the electronic license plate system.

Cause or Consequence of Highway Accidents	Preventive or Moderating Action of Electronic License Plate System
Exceeding posted speed limit	• Warning signals sent to drivers exceeding speed limits • Automatic recording of any vehicle that persists in exceeding the posted speed limit, so that drivers would know that if they persist in speeding, they would almost certainly get caught
Speeds too fast for conditions	• Warning signals sent to drivers (bl) • Harmonic collision avoidance radar causes brakes to be automatically applied if closing rate to vehicle in front is too high
Rear-end collisions	Harmonic collision avoidance radar causes brakes to be automatically applied if rear-end collision threatens
Driving the wrong way in a one-way street	Warning signals sent to drivers
Stolen vehicles (the accident rate of stolen vehicles is ten times the average accident rate)	Automatic monitoring for stolen vehicles
Defective vehicles	Automated vehicle inspection station
Injured people at scene of accidents	Quicker response of ambulances and other emergency vehicles

always been closely controlled by governments (licensing of drivers and vehicles, clearly visible license plates for vehicles, mandatory safety equipments, speed limits, etc.). Motorized highway vehicles are simply too dangerous to be left alone with a minimum of control. In the United States alone, motorized highway vehicles have killed nearly 2 million persons since 1900, a number far larger than the total number of U. S. military casualties in all wars. Currently in the United States, motor vehicles on the average kill someone every 10 minutes and injure someone every 6 seconds. Increased control over motor vehicles would be a cheap price to pay for reducing this slaughter.

Acknowledgments

The author thanks Henry C. Johnson, Gerald S. Kaplan, Richard J. Klensch, Jerome Rosen, Joshua Shefer, and Harold Staras for many helpful discussions.

References:

[1] J. Shefer and R. J. Klensch, "Harmonic Radar Helps Autos Avoid Collisions," **IEEE Spectrum**, Vol. 10, p. 38, May 1973.

[2] J. Shefer, et al, "A New Kind of Radar for Collision Avoidance," SAE Automotive Engineering Congress and Exposition, Detroit, Mich., Feb. 26, 1974.

[3] R. J. Klensch, et al, "A Microwave Automatic Vehicle Identification System," **RCA Rev.,** Vol. 34, No. 4, Dec. 1973.

[4] S. Ritter, et al, "Speeding of the Deployment of Emergency Vehicles," **IEEE Spectrum,** Vol. 10, p. 56, Dec. 1973.

[5] G. S. Larson, "Electronic Systems for Enroute Truck Security," paper presented at the Intersociety Conf. on Transportation, Denver, Colo., Sept. 23-27, 1973.

[6] A. S. Clorfeine, "Driving Under the Influence of Electronics," **IEEE Spectrum,** Vol. 10, p. 32, May 1973.

[7] **Societal Costs of Motor Vehicle Accidents,** Department of Transportation Preliminary Report, April 1972.

The Electro-Optic Transfer Function in Nematic Liquids*

Alan Sussman

RCA Solid State Division, Somerville, N.J. 08876

Abstract—The steady-state optical behavior of nematic liquids under electrical excitation is reviewed in detail. The phenomena observed depend on dielectric type, geometrical configuration, conductance and operating frequency. The distinction between field effects (mostly reorientation) and conductance effects (mostly hydrodynamic) is usually considered intrinsic in materials of positive dielectric anisotropy but selectable by choice of conductance/frequency in materials of negative dielectric anisotropy. It is shown that this distinction is not so clear cut. Criteria for optical measurements are outlined for reorientation, diffraction, and scattering phenomena in three geometric configurations useful in both device and material evaluation. The use of a photoconductor control electrode is analyzed.

Introduction

When an electric field is applied across transparent plane-parallel electrodes containing mesomorphic liquids, many complex phenomena occur that depend on the optical, dielectric, and elastic properties of the liquid, the geometry of the test situation, and the nature of the electrical signal.[1] The electro-optic transfer function is a way of specifying such optical changes. An ever increasing interest in liquid-

* Presented in part as an invited paper at the Optical Society of America annual meeting, Rochester, N.Y. Oct. 1973.

crystal electro-optic phenomena particularly, but not entirely, in the field of display devices has caused a corresponding growth of the literature[2]; hence, this review is limited to steady-state properties of nematic liquids.

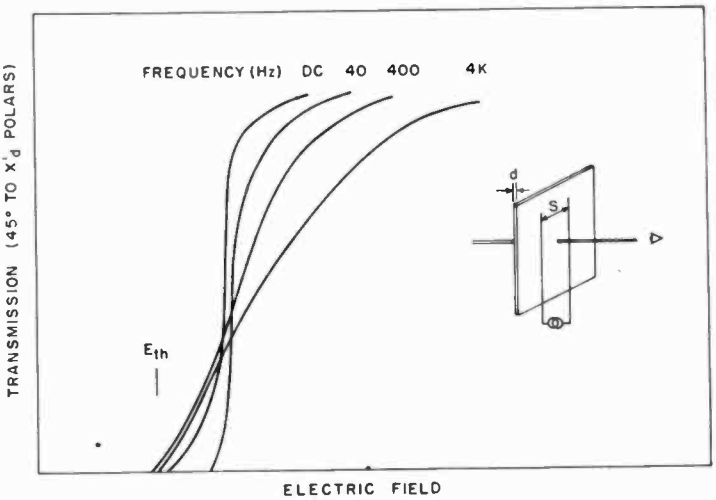

Fig. 1—Field effect (lateral electrode geometry). The change in optical orientation properties with frequency is a result of changing field penetration. The dielectric relaxation frequency is 80 Hz. This material of positive dielectric anisotropy does not show any turbulent flow (R.A. Soref[9]).

It is convenient to divide nematic liquids into two classes depending on the dielectric anisotropy—positive for those in which the molecular orientation described by a vector, called the director, tends to align parallel to an electric field, and negative when that alignment is perpendicular to the field. Those phenomena in which reorientation is the major result are considered "field effects". This designation is not arbitrary, since it also separates these dielectric effects from those whose mechanism has additionally a hydrodynamic flow, i.e., realignment or disruption of the liquid by material transport. Sometimes, material parameters completely specify electro-optical performance, while in other cases, the two regimes are selectable by choosing the frequency of excitation.

In materials of positive dielectric anisotropy, most electro-optic phenomena are frequency independent field effects; hydrodynamic effects, occurring with certain boundary conditions result in stable (laminar) flow,[3] and no turbulent-flow reorientation is observed.[4]

In the storage effect,[12] on the other hand, a write mode is obtained below the dielectric relaxation frequency. This is a hydrodynamically produced turbulent flow that disturbs the (cholesteric) order. An erase mode is produced at high frequencies, where the ordered structure is restored by dielectric reorientation forces.

Depending on the geometry, dielectric reorientations are sometimes accompanied by hydrodynamic transients, i.e., a backflow.[13] (The reorientation caused by hydrodynamic flow is well known.[14]) Such backflow transients, under certain conditions, can give rise to turbulent effects similar to dynamic scattering; the latter term should be reserved specifically for the sequence: domains, domain instability, and scattering, produced by conductance hydrodynamics.

Another important frequency is the inverse of the time it takes for an ion to traverse the whole of the way across the electrode distance $t_{tr} = V^2/\mu d$, where V is the voltage, μ the mobility, and d the electrode spacing.[15] Unlike the dielectric relaxation frequency, $f(\text{transit}^{-1})$ depends on voltage and cell thickness. It effectively separates ac from dc effects whose hydrodynamic mechanisms are related to electrode effects.[16] Note that for high enough voltages and/or small enough spacing, $f(\text{transit}^{-1})$ can exceed the electrical operating frequency. This condition is particularly favorable for loss of conducting ions by electrosorption; such effects have been noted, especially in nematics with low (initial) conductivity.[17]

Differences in threshold behavior when other than sinusoidal excitation is used in dynamic scattering[18] have been observed.[19]

Modifications to the threshold-voltage characteristic may also be obtained by adding a high-frequency signal to the low-frequency drive.[20] This adds a dielectric orienting field that tends to suppress hydrodynamic flow, thereby increasing the low-frequency voltage required to cause a given scattering as compared to that required without the high frequency.

Geometric Considerations in Optical Measurements

Careful consideration must be given to using an appropriate geometry when taking measurements, particularly if the results are to be used to evaluate the visual performance of a display system.

In dielectric reorientation effects (such as voltage-controlled birefringence,[21] twisted nematic structure effects,[22] and guest-host effects[23]), the optical changes are basically variations in either optical density or wavelength of absorption. As such, the optical measurements are quite straightforward. The plane-parallel-geometry structures may be considered neutral density filters, with angle-dependent transmission or

wavelength characteristics. It is necessary to apply corrections for refraction because of index mismatch,[24] which is particularly important for measurements on optical parameters where a liquid crystal is used as a switch to couple into a waveguide,[25] to modulate and switch in a waveguide,[26] or to control total reflectance at a prism/liquid-crystal interface.[27]

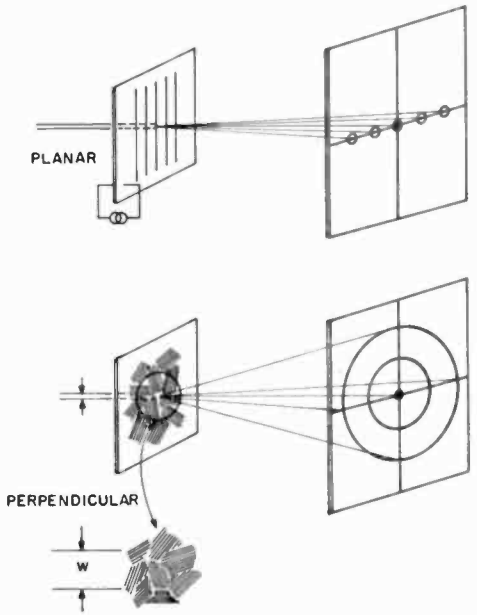

Fig. 2—Diffraction by domains. A nematic orientation that is originally planar usually results in a well-ordered domain structure that behaves like a phase grating, and a diffraction pattern consisting of a series of spots is obtained (top). When the orientation is originally perpendicular, clusters of domains may give rise to diffraction spots or rings depending on the relative diameter of the probe (w) and the dimensions of the domain clusters.

When scattering or diffraction phenomena are studied, however, the geometry becomes particularly important, both because of the rich nature of the optical processes and because of the more varied ways in which such processes are applied to display devices. In the case of diffraction by domains,[28] different results may be obtained depending on the original orientation of the fluid and the relation between the beam probe size and the domain cluster size.

When domains are observed in configurations where the surfaces induce planar orientation,[29] they exhibit the properties of a phase grating, and unpolarized laser illumination at normal incidence produces a spot diffraction pattern[30] (Fig. 2, upper part).

If, however, the orientation is originally perpendicular, the first electro-optic effect is the conversion to a planar orientation in the bulk, followed at higher voltage by the domains, whose cylindrical axes may not be correlated over large distances, and "clusters" result. The diffraction pattern will be a ring if the probe diameter (w) is large compared to the cluster size (Fig. 2, lower part).

To measure the angle dependence of scattering in a transmission-type display, three general schemes may be employed. In Fig. 3 they are illustrated schematically, and qualitative electro-optic transfer curves are given for each.

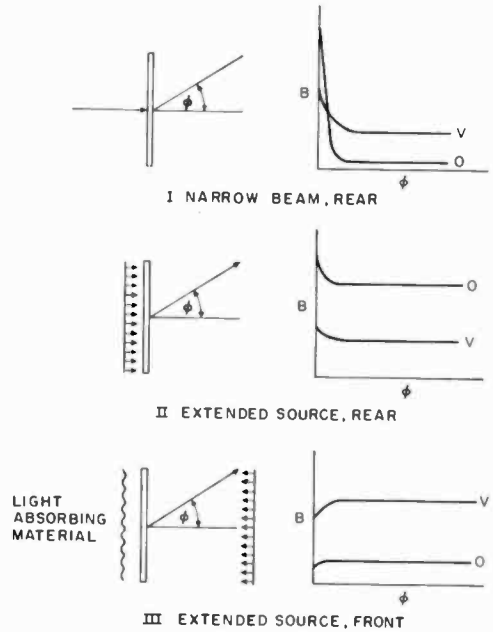

Fig. 3—Influence of geometrical parameters on scattering electro-optic transfer function measurements. Three cases are illustrated, with their corresponding electro-optic transfer functions (highly schematic).

Type I—Narrow Beam, Rear

In type I, a laser beam is used as a coherent probe; such a configuration has given a good deal of information on the ordering of the nematic liquid,[31] on domains,[32] and on the structural modifications that occur during dynamic scattering.[33] Both the angle of incidence and the detector angle can be varied; such data can be reported in compact

graphical form.[34] This configuration is also applicable to optical data processing[35] and holographic information-storage techniques.[36]

With illumination normal to the plane of the structure (Fig. 3, top) and no voltage applied (0 curve), only a small inherent scattering may be measured off-axis.[31] On-axis, of course, the unscattered beam is virtually undiminished in intensity. With the application of voltage V, there is finite scattering into off-axis angles (increase in signal), but an attenuation of the on-axis brightness signal; a contrast ratio as high as 10^4 has been measured for spatial filtering applications.[37]

Type II—Extended Source, Rear

Type II has an extended-area source behind the cell, with the detector in front. The liquid-crystal plane when excited reduces the intensity, and may be thought of as a variable density screen, similar to type I before the crossover, with the liquid crystal plane integrating the light, which arrives at all angles. This is a rather uninteresting configuration, although some knowledge of the angle dependence of the scattering is needed when the liquid-crystal plane is used for a viewing screen,[38] as a variable optical stop, or as an image plane for projection.

Type III—Extended Source, Front

In type III the illumination is from the viewing side, with a light-absorbing screen behind. This configuration is not used frequently in digital displays, because the scattering to the rear is not particularly efficient.[17] By illuminating the screen from the back, full use is made of the scattering in the propagation direction, i.e., toward the viewer. A unique configuration for display devices is to illuminate from the rear through a screen consisting of blackened vanes adjusted so as to give the maximum viewing angle with minimum total thickness of the system.[39]

A similar configuration, but with a mirror surface as the rear electrode, has a wide application in watch and clock displays. Best results are obtained when the viewer sees reflected in the mirror a light-absorbing surface. The on-state is particularly bright because both transmitted light and scattered light are reflected back toward the viewer. A type III electro-optic transfer curve is thereby obtained.

If, however, the mirror reflects a bright surface, it is possible that contrast reversal will occur, i.e., the type II configuration. For some angles and brightnesses, a no-contrast result is possible. In the case

of field effects, particularly the twisted structure, type III effects are especially subtle when the angle of incidence is varied.

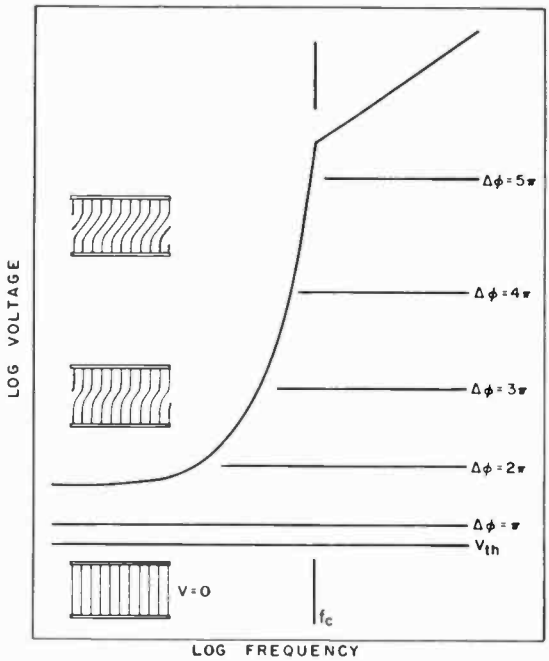

Fig. 4—Retardation as a function of voltage. The continuing reorientation of the structure (left side) with increasing voltage results in an ever increasing retardation, i.e., birefringence. The retardation $\Delta\phi$ continues to increase unless another electro-optic regime ensues; viz, below the dielectric relaxation frequency, domains, and above, chevron distorions (M. Hareng, et al[21]).

Field Effects—Negative Dielectric Anisotropy

With an orientation that is originally perpendicular to the electrodes, and material of negative dielectric anisotropy, an electric field interacts with the fluid to cause a tilt in the optical axis, beginning at the center of the cell, when a threshold voltage is reached.[21] This tilt results in birefringence that continues to increase with increasing voltage, unless, of course, the threshold voltage for another phenomenon is exceeded, e.g., domains at low frequency or "chevrons" at high frequency[40] (Fig. 4). As the field increases, the tilt angle continues to increase as does the retardation, measured as a phase difference $\Delta\phi$.[41] To get uniform retardation over large areas, the surface may be prepared to give a slight bias, i.e., a uniform but small tilt off-normal.[42]

The electro-optic transfer function at a fixed angle between crossed polarizers is shown in Fig. 5. By swinging between two voltages, it is possible to modulate the color equivalent to a phase retardation at one wavelength (first voltage) to produce a color equivalent to a different wavelength (second voltage). This is the basis for a matrix-

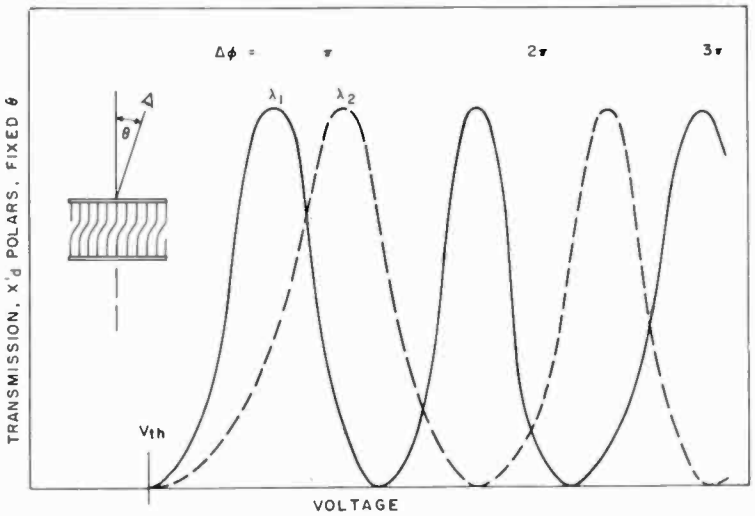

Fig. 5—Electro-optic transfer as a function of voltage. At a fixed viewing angle, the transmission of monochromatic light between crossed polarizers undergoes a series of maxima, which occur with increasing voltage and represent phase retardations of π, 2π, ... etc (M. Hareng, et al[21]).

addressed color crossed-array display[43] where the angle dependence of the color produced by the phase retardation (or transmission of light between crossed polarizers when monochromatic light is used, as shown in Fig. 6) has been avoided by using a projection system. Interdigitated electrodes may be used to create small areas of different retardation, the overall area being angle independent.[44]

The angle dependence can be used to make accurate measurements of the electrode spacing in liquid crystal cells.[45]

Advantage may be taken of the property of certain pleichroic dyes in which the wavelength of absorption in the crystal is different along different crystalline axes. If such a dye is dissolved in and follows the alignment of the liquid crystal of the previous example[46] with the analyzer removed, the absorption in the voltage-off state would depend on the extinction coefficient perpendicular to the dye crystal axis; when the structure is changed by application of voltage, the absorption

becomes converted to that related to the extinction coefficient parallel to the crystal axis. If one of these absorptions is not in the visible, no polarizer is required to see the color change, and the angle dependence results in a change in optical density at the visible wavelength.

Discussion of the chevron regime, although also a field effect, is described in the section on diffraction.

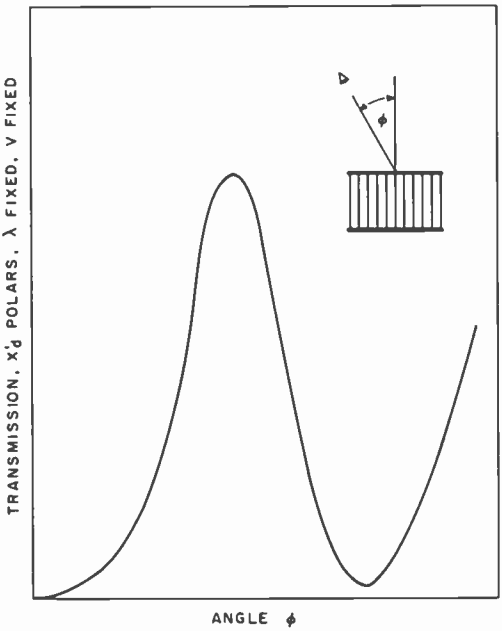

Fig. 6—Transmission as a function of viewing angle. At a constant voltage, and for a fixed wavelength, the transmission between crossed polarizers shows an angular dependence. At angles other than normal, a correction for refraction by the glass is necessary (zero voltage is illustrated).[44]

Field Effect—Positive Dielectric Anisotropy

Since materials of positive anisotropy turn their orientation parallel to the direction of a field, a necessary requirement is an off-state of uniform planar alignment. Then, a change analogous to that just discussed may be obtained by the application of a field; above a threshold voltage, the parallel orientation (beginning at the center) eventually becomes indistinguishable optically from one that is perpendicularly aligned. Between crossed polarizers, the result is a lessening of the retardation with increasing voltage, with an electro-optic transfer function similar to that of Fig. 5. The change is maximum when the

polarizer axes are normal to the planar axes. At any voltage, the transmission is angle dependent.[47] with a symmetry related to whether or not the angle is varied in a plane containing the undisturbed liquid orientation.

Incorporation of a pleiochroic dye and elimination of the analyzer results in voltage-controlled optical absorption, the guest-host effect.[48]

The "twisted" nematic structure has unique optical properties: the plane of linearly polarized light, of wavelength shorter than the distance over which the twist makes one revolution, is rotated following the twist.[49] In static patterns a 90° rotation is maximum, greater angles being unstable. Placed between crossed polarizers, such a cell would cause maximum transmission. The converse would be true if the polarizers were initially parallel.

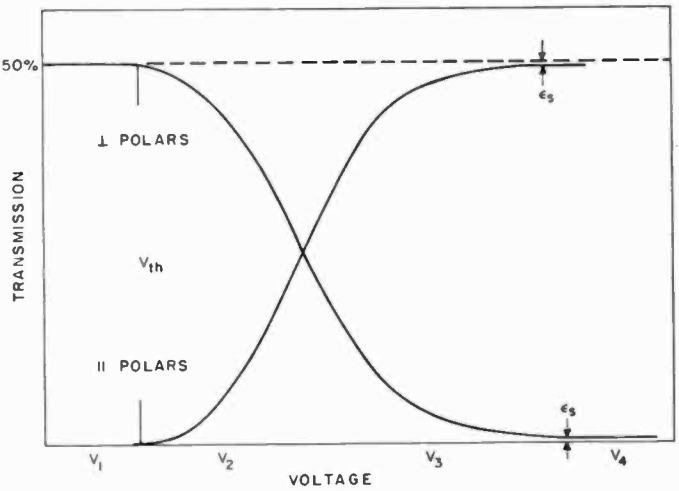

Fig. 7—Electro-optic transfer function of twisted structure. Above threshold, increasing the voltage casuses the structure to lose the ability to rotate the plane of polarized light; eventually, the optical behavior of the structure approaches that of a perpendicular homeotropic nematic. The difference (ϵ_s), however, is still finite at three times threshold.[52]

If the material has a positive dielectric anisotropy, then an electric field can convert the twisted structure to one that eventually has the optical properties of a perpendicularly oriented one.[22] A threshold voltage, as shown in Fig. 7, is present; only at sufficiently high voltages is the difference between the still-twisted and the non-twisted structure undetectable. As in the voltage-controlled birefringence, the tilt of the

orientation continues with increasing voltage, being greatest at the midpoint between the electrodes (Fig. 8, top). This causes birefringent color changes, but an overshadowing optical effect occurs because of the modifications to the twist. Initially, the twist may be considered uniform throughout the cell thickness (Fig. 8, bottom). With increas-

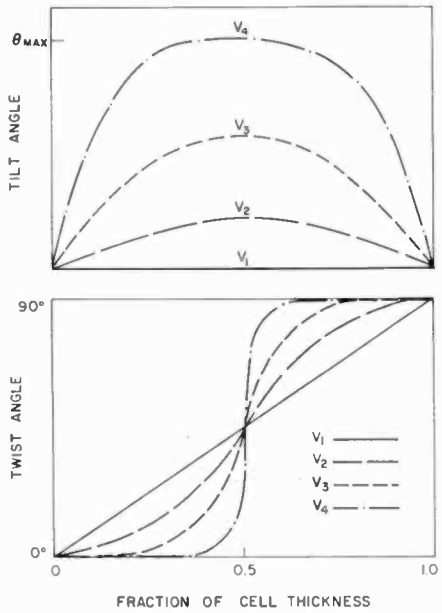

Fig. 8—Variation of tilt and twist angles throughout twisted structure as a function of voltage. Top figure shows symmetric tilt occuring as the voltage increases (as in Fig. 7). Bottom figure shows the symmetric twist that, while uniform at voltages below threshold, becomes distorted with increasing voltage. When most of the twist occurs over a distance small compared to the wavelength of light, the structure can no longer rotate the plane of polarization.[52]

ing voltage, the twist becomes distorted. Above that value of voltage corresponding to the optical threshold, the total distributed twist is converted to distortions near the wall, so that the rotation conditions cannot be met[50] and the optical density of the structure changes. Eventually, increasing voltages result in almost total loss of rotation; for a cell between crossed polarizers initially, the optical transmission would increase from that of the parallel polarizers to one that approaches that of the crossed polarizers. The coherence of light so rotated is not affected greatly.[51]

Fig. 9 shows calculated curves[52] for angle-dependent transmission

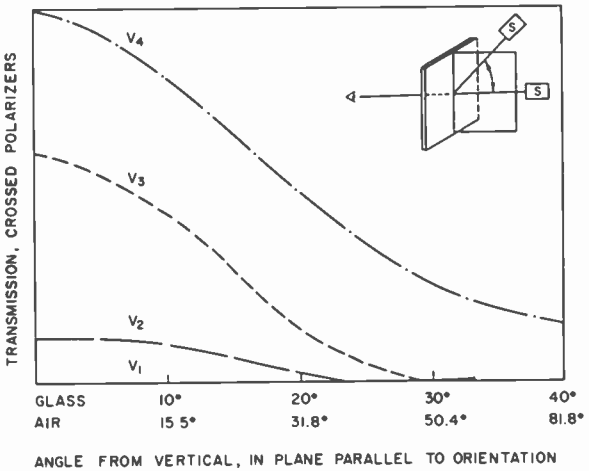

Fig. 9—Electro-optic transfer coefficient along surface orientation for twisted structure. With the source (S) in a plane perpendicular to the electrodes and parallel to the optic axis of the nematic orientation at that electrode, the optical transmission is a monotonic function of angle and voltage (calculated curves).[52]

in which the light being measured emerges perpendicular to the electrode face, while the source (S) is rotated in a plane that is perpendicular to the electrode and contains the orientation of one of the electrodes. Note that the results are relatively monotonic. If however, the source is in a plane rotated so as to be 45° to the orientation direction in the electrode face, the results are complex (Fig. 10).* Type I, II, and III measurements may be expected to yield such complex results.

Type II is at present the basis for most digital applications. If a specular back is used (behind the polarizer), the reflected brightness is maximized, but at the expense of curtailed viewing angle; in Type III configuration, with a scattering back plane acting as a (partially depolarized) source of illumination, the optical results would be expected to be similar to those with Type II.

Hydrodynamic Effects—Diffraction by Domains

Liquid-crystal hydrodynamic phenomena are extremely complex, and the mechanisms for their production are far from being completely

* The reason is again that the light in the probe beam now is resolved into birefringent components. In these calculations, the index of the glass was assumed to be equal to the higher index of the nematic liquid and the necessary refraction for other than normal incidence corrected for. Note that this results in a considerable difference between the geometrical beam/glass angle and the actual beam/liquid angle.

elucidated. The differences between positive and negative dielectric anisotropy material are more distinct than in the field effects. The negative materials are more likely to produce striking opto-hydrodynamic changes. There are, however, indications that positive materials may participate in similar although more subdued effects.[53]

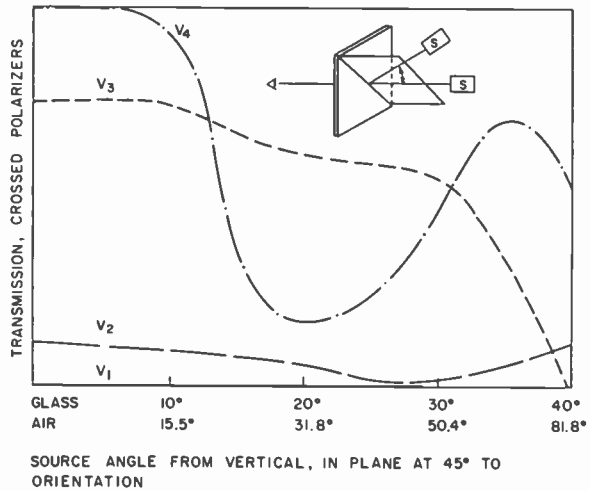

Fig. 10—Electro-optic transfer coefficient at 45° to surface orientation for twisted structure. When the source (S) is in a plane perpendicular to the electrodes but not parallel to the optic axis of the nematic in the electrode (director), the variation of transmission between crossed polarizers as a function of angle and voltage is no longer simple, because of anisotropic propagation within the liquid (calculated curves).[52]

The following is a typical series of events when a material of negative dielectric anisotropy, originally in the planar orientation, is subject to an electric field of a frequency between the dielectric relaxation frequency and the inverse transit-time frequency. Dielectrically, the field should cause no change; above a threshold voltage, however, a periodic pattern of light and dark lines appears. These domains,[54] associated with vortical liquid flow,[55] have a spacing proportional to the electrode separation. The refractive properties are not unlike an array of cylindrical lenses, with alternate convergent and divergent bands, which are the domain boundaries, visible in ordinary light. This focal length decreases with increasing voltage and represents the change in curvature of each lens due to increased velocity of the fluid. (The number density of domains need not change.)

The periodic pattern also exhibits the properties of a phase grating, and a diffraction pattern may be observed (Fig. 2). When the voltage is raised, the steady-state result is a higher domain periodicity, i.e.,

new domains have made their appearance. There being no smooth way for a new domain to decrease the periodicity, a transient diffraction occurs, which relaxes into a new equilibrium steady-state pattern whose intensity distribution may be correlated with the spatial frequency of the domain.[30] Such new domains, by the nature of the symmetry of the electrode configuration, might be expected to also have a symmetrical flow pattern. With further increase in voltage, the new domains apparently cannot enter into an orderly array, and the turbulent properties of dynamic scattering begin to appear. Optically speaking, the structure behaves like a deep phase screen, i.e., at each position there is a phase retardation resulting in a path difference which may be several wavelengths.[33]

At frequencies below the inverse transit time, the electrode effects may no longer be geometrically symmetric;[17] the domain periodicity is nonuniform because a second diffraction pattern, harmonically unrelated to the original set, has made its appearance.[15]

The stability of the hydrodynamic modes of cylindrical domains has been investigated using a model with the appropriate boundary conditions.[56] The results indicate a stability curve with two branches—one on which the domain spacing remains constant with voltage, the other on which the spacing varies inversely with the voltage (as just described). These appear in Figure 11. Under certain conditions, which may be depend on material parameters as well as electrode spacing, dc excitation does not result in dynamic scattering, but only in a continuing increase in domain periodicity.[57] This result is shown in Fig. 12. Here, the simplified experimental data show the intensity distribution of a diffraction ring. The original orientation was perpendicular to the electrodes, so that the domain clusters would be expected. In this case, an unusual domain structure was observed.[58] A tree-like pattern, as shown in the upper inset of Fig. 11, allowed an almost continuous variation in domain spacing as the voltage changed. The new domains appeared as new branches and the growth was quite smooth. When the voltage was increased, the diffraction pattern would become diffuse for an instant, then relax into the sharp diffraction rings, as shown in Fig. 12. The intensity profile of the highly reflected domains was a sharp as that for less diffracted ones, indicating an improvement in diffraction efficiency with increasing voltage.

At frequencies above the dielectric relaxation frequency, another diffraction with a threshold makes its appearance (see Fig. 4). This is the "chevron" regime,[59] which is not hydrodynamic in origin but depends on interaction between the anisotropic dielectric properties of the fluid and the field. It represents a sinusoidal modulation of the

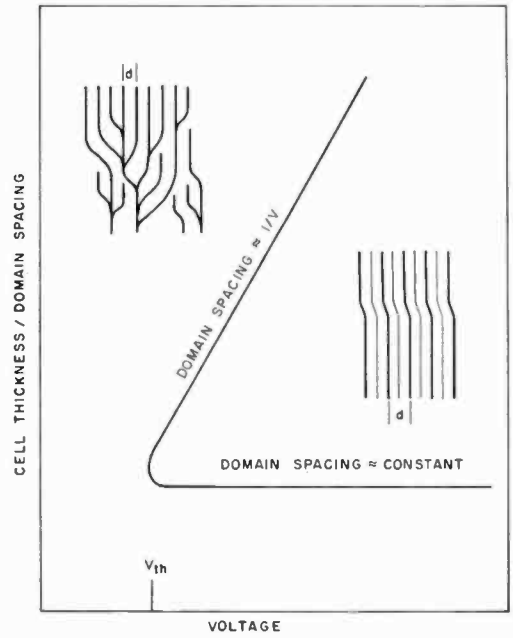

Fig. 11—Domain spacing as influenced by hydrodynamic regime. The periodicity of domains shows a voltage variation that depends on hydrodynamic modes, represented by two branches of the stability curves.[56] Insets: right, domains are cylindrical; left, a tree structure allows a continuous variation of the spacing d.[58]

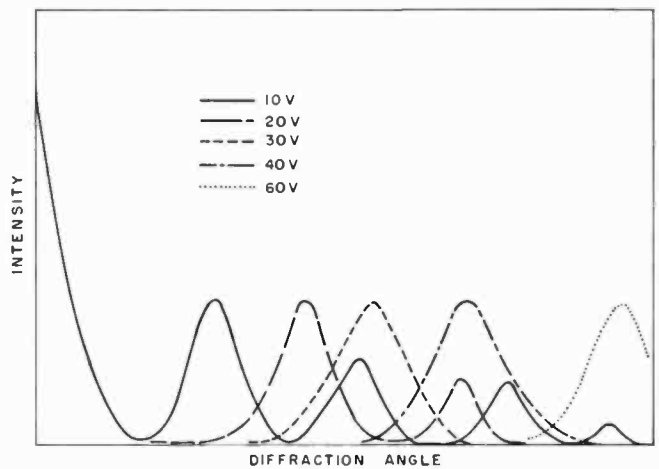

Fig. 12—Voltage dependence of diffraction by domains. The intensity distribution of the diffraction rings (for a single wavelength) with increasing dc voltage demonstrates a constant intensity profile even at 60 volts where the diffraction angle is nearly 50°. No dynamic scattering occurs.[57]

director, with a threshold field proportional to the square root of the frequency, and results in a phase-grating condition.[40] The spatial frequency of these domains is much greater than that of the low-frequency domains; the diffraction also gives rise to angle-dependent chromatic effects. The model based on a symmetric periodic slit grating, which is satisfactory for low-frequency domains, must be corrected for refraction within the liquid.[60] An added stabilizing field, at frequencies above threshold for chevrons, causes an increase in period.[61]

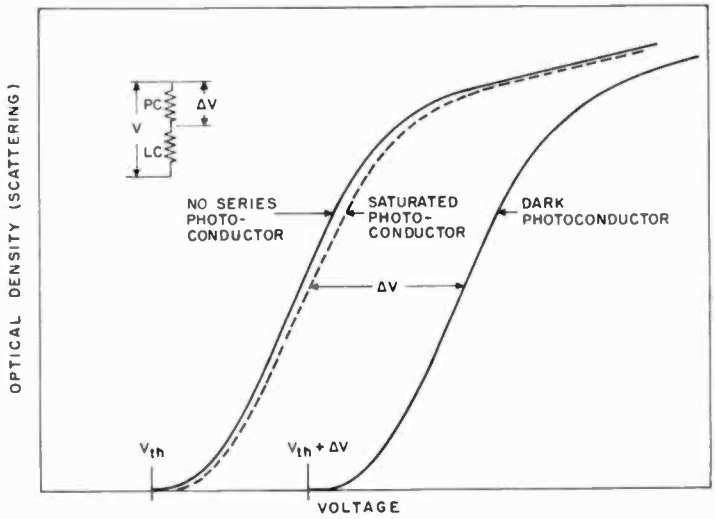

Fig. 13—Photoconductor control of dynamic scattering. Electro-optic transfer function is shown in the dark and under saturated photoconductor conditions. For the liquid crystal to be below threshold voltage in the dark, the value of the applied voltage must not exceed the original threshold voltage (V_{th}) plus the voltage drop across the dark photoconductor (ΔV). With suitable choice of photoconductor parameters, the light-saturated photoconductor allows the liquid-crystal response to behave almost as if no photoconductor were present.

Dynamic Scattering

As domains become increasingly unstable with increasing voltage, the phenomenon known as dynamic scattering[18] occurs. Fig. 13 shows a a typical electro-optic transfer function. Note the lack of saturation of scattering with voltage in the type I case. At higher voltages, changes in flow patterns occur at definite thresholds, and result in changed optical, electrical, and kinetic properties.[62] Another phenomenon, caused by certain patterns of flow, particularly near the dielectric relaxation

frequency, converts an originally perpendicularly oriented off-state to one that is (temporarily) planar.[63]

The angular dependence of the scattering has been observed as a function of voltage,[64] and the results in Fig. 14 are typical. (The

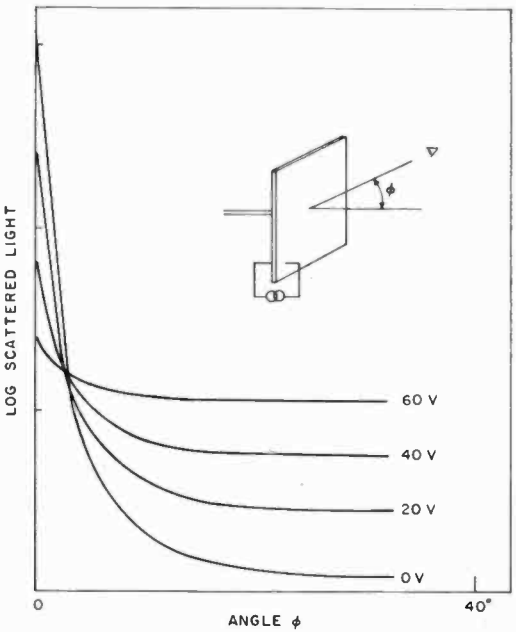

Fig. 14—Angular dependence of dynamic scattering as a function of voltage. Under narrow beam condition (Type I), the scattering of the original beam near the optic axis results in a reduction in transmission; off-axis, however, the scattering results in an increase in light detected. (The crossovers do not necessarily occur at the same angle.)

crossover, however, is not always found at the same angle for every voltage.) The effect of increasing cell thickness is an increase in the voltage at which equivalent scattering occurs; the threshold is unchanged. The angular dependence is also relatively independent of thickness.[34] The scattering at a particular value of thickness, angle, and voltage has a direct dependence on the optical anisotropy of the nematic compound under study.[65] The scattering for any compound is independent of the current density[66] as long as the measurement is made sufficiently far from the dielectric relaxation frequency.

When polarized light is used, the angular scattering dependence is a function of the angle between the polarizer and the direction of the (original) planar orientation.[31]

Photoconductor Control

The incorporation of a photoconductor layer in series[67] with the liquid crystal layer allows direct conversion from optical input to optical output; such devices hold promise of usefulness in the field of image and data processing,[43] optical conversion,[68] and storage.[69] As of this review, photoconductor control of dynamic scattering and storage effects only have been reported. Optimum performance of such devices is achieved when the resistance of the photoconductor is matched to that of the liquid crystal, so that the voltage drop across the photoconductor, ΔV, leaves the voltage across the liquid crystal below the threshold value when the photoconductor is unilluminated; correspondingly, when the photoconductor is illuminated, the voltage drop should be as low as possible, allowing full scattering operation of the liquid crystal. Fig. 13 shows the electro-optic transfer functions for the dynamic scattering discussed above for the series photoconductor saturated and in the dark. The optimum applied voltage, as will be seen later, is $V_{th} + \Delta V$.

The relationship between the photoconductor and liquid resistance in the dark and under illumination has been treated for the case of pure resistance. There are reported cases in which the electro-optic response depends on whether the illumination falling on the photoconductor reaches it from the liquid-crystal side or from the transparent-conductor side. This rectification is not observed in all liquid-crystal photonconductor systems.[70] However, the generality of the above discussion is not affected.

To achieve sufficient control over the photoconductor, with either a bulk or barrier photoconductor, requires a photon flux of $10^{11}/cm^2$.[71] This value is comparable to the flux required for other processes, such as Xerographic or electroluminescent outputs. When the photoconductor is nonohmic, higher minimum exposures may be required.

Operation in the transmission mode allows direct insertion of the image plane into an optical crystal. This, of course, requires the photoconductor to operate outside the spectral range of the projection source. In reflectance modes, the photoconductor may be isolated from the secondary illumination by means of an insulating and/or opaque dielectric layer.[72] Such a configuration requires ac operation, which happily circumvents some of the electrochemical problems associated with dc.[73]

Using the somewhat artificial assumption that equal increments of illumination result in equal changes in ΔV, Fig. 15 was developed. The liquid-crystal scattering is plotted against the illumination up to the value at which the photoconductor "saturates", i.e., when increasing light no longer significantly changes ΔV. If the values are properly

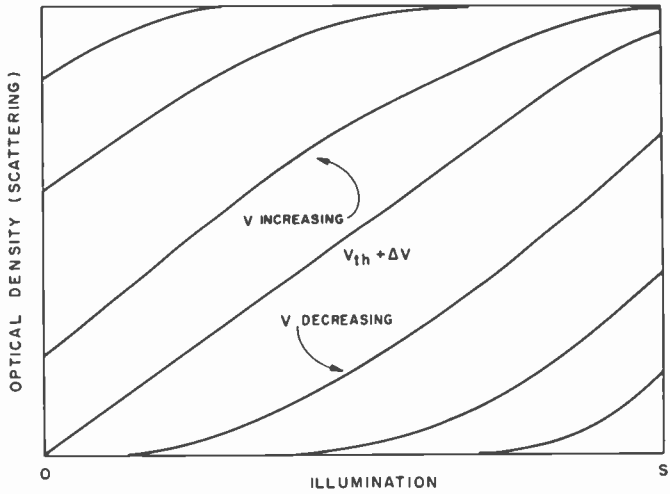

Fig. 15—Dynamic scattering range as a function of light intensity and applied voltage. The operating voltage $V_{th} + \Delta V$ may be optimized. At lower than optimum voltages, the maximum scattering (S) with a properly selected photoconductor, is reduced. At even lower voltage, the scattering reaches a saturation value, but is not zero even at low light levels (calculated curves).

chosen, the behavior of the liquid crystal should approach that observed with no series photoconductor. At voltages above and below the optimum, $V_{th} + \Delta V$, the scattering curve was estimated from Fig. 13. Note that for voltages lower than optmium, maximum scattering cannot be obtained; at the lowest voltages, the scattering is not zero even when the photoconductor is unilluminated. The shape of the original scattering–voltage curve has a significant effect on the dynamic range. For example, a steep electro-optic function, which is desirable for matrix addressing or digital display, will reduce the halftone range in the photoconductor combination, as might be expected.

References:

[1] Several review articles, emphasizing electro-optic properties of liquid crystals are available: R. A. Soref, "Liquid Crystal Light Control Experiments," in **The Physics of Opto-Electronic Materials,** ed. W. A. Albers, Jr., Plenum Press, New York (1971); A. Sussman, "Electro-Optic Liquid Crystal Devices: Principles and Applications," **IEEE Trans. Parts, Hybrids, and Packaging,** Vol. PHP8, p. 24 (1972); and A. Sussman, "Liquid Crystals in Display Systems," in **Liquid Crystalline Systems,** ed. G. W. Gray and P. A. Winsor, Ellis Horwood, London (in press).

[2] For example in 1969, there were 70 papers listed in Physics Abstracts. In 1970, 250; in 1971, 315; and in 1972, 390.

[3] P. DeGennes, "Electrohydrodynamic Effects in Nematic Liquid Crystals I. DC Effects," in **Comments on Solid State Physics,** Vol. 3, p. 35 (1970); and P. A. Penz, Electrohydrodynamic Solutions for Nematic Liquid Crystals with Positive Dielectric Anisotropy," **Mol. Cryst.,** Vol. 23, p. 1 (1973).

[4] W. H. DeJeu, C. J. Gerritsma, and Th. W. Lathouwers, "Instabilities in Electric Fields of Nematic Liquid Crystals with Positive Dielectric Anisotropy: Domains, Loop Domains, and Reorientation," **Chem. Phys. Lett.**, Vol. 14, p. 503 (1972).

[5] G. H. Heilmeier and W. Helfrich, "Orientational Oscillations in Nematic Liquid Crystals," **Appl. Phys. Lett.**, Vol. 16, p. 155 (1970).

[6] H. S. Harned and B. B. Owen, **The Physical Chemistry of Electrolytic Solutions**, 2nd ed., Reinhold Publishing Co., New York, 1950, Chap. 4.

[7] A. Sussman, "Ionic Equilibrium and Ionic Conductance in the System Tetra-iso-pentyl Ammonium Nitrate p-Azoxyanisole," **Mol. Cryst. and Liq. Cryst.**, Vol. 14, p. 182 (1971).

[8] D. Meyerhofer, A. Sussman, and R. Williams, "Electro-Optic and Hydrodynamic Properties of Nematic Liquid Films with Free Surfaces," **J. Appl. Phys.**, Vol. 43, p. 3685 (1972).

[9] R. A. Soref, "Transverse Field Effects in Nematic Liquid Crystals," **Appl. Phys. Lett.**, Vol. 22, p. 165 (1973); and N. V. Madhusudana, P. P. Karat, and S. Chandrasekhar, "Some Electrohydrodynamic Distortion Patterns in Nematic Liquid Crystals," **Current Science**, Vol. 42, p. 147 (1973).

[10] W. Haas, J. Adams, and J. B. Flannery, "New Electro-Optic Effect in a Room-Temperature Nematic Liquid Crystal," **Phys. Rev. Lett.**, Vol. 25, p. 326 (1970).

[11] W. Helfrich, "A Simple Method to Observe the Piezoelectricity of Liquid Crystals," **Phys. Lett.**, Vol. 35A, p. 393 (1971).

[12] G. H. Heilmeier and J. Goldmacher, "A New Electric Field Controlled Reflective Optical Storage Effect in Mixed Liquid Crystal Systems," **Proc. IEEE**, Vol. 57, p. 34 (1969).

[13] F. Brochard, "Backflow Effects in Nematic Liquid Crystals," **Mol. Cryst. and Liq. Cryst.**, Vol. 23, p. 51 (1973).

[14] W. Helfrich, "Molecular Theory of Flow Alignment of Nematic Liquid Crystals," **J. Chem. Phys.**, Vol. 50, p. 100 (1969); and "Conduction-Induced Alignment of Nematic Liquid Crystals: Basic Model and Stability Considerations," **J. Chem. Phys.**, Vol. 51, p. 4092 (1969).

[15] D. Meyerhofer and A. Sussman, "The Electrohydrodynamic Instabilities in Nematic Liquid Crystals in Low-Frequency Fields," **Appl. Phys. Lett.**, Vol. 20, p. 337 (1972).

[16] N. Felici, "Phenomenes Hydro et Aerodynamiques dans la Conduction des Dielectric Fluides," **Rev. Gen. Elect.**, Vol. 78, p. 717 (1969); A. Sussman, "Contribution of the Ionic Double Layer to the DC Hydrodynamic Instabilities in Nematic Liquids," Paper presented at Fourth International Liquid Crystal Conf., Kent, Ohio, Aug. 1972; and R. J. Turnbull, "Theory of Electrohydrodynamic Behaviour of Nematic Liquids in a Constant Field," **J. Phys. D: Appl. Phys.**, Vol. 6, p. 1745 (1973).

[17] A. Derzhanski and A. G. Petrov, "Inverse Currents and Contact Behaviour of Some Nematic Liquid Crystals," **Phys. Lett.**, Vol. 36A, p. 307 (1971).

[18] G. H. Heilmeier, L. A. Zanoni, and L. A. Barton, "Dynamic Scattering: A New Electro-Optic Effect in Certain Classes of Nematic Liquid Crystals," **Proc. IEEE**, Vol. 56, p. 1162 (1968).

[19] W. H. DeJeu, "Instabilities of Nematic Liquid Crystals in Pulsating Electric Fields," **Phys. Lett.**, Vol. 37A, p. 365 (1971); and Orsay Liquid Crystal Group, "Transition Between Conduction and Dielectric Regimes of the Electrohydrodynamic Instabilities in a Nematic Liquid Crystal," **Phys. Lett.**, Vol. 39A, p. 181 (1972).

[20] P. Wild and J. Nehring, "Turn-on Time Reduction and Contrast Enhancement in Matrix-addressed Liquid Crystal Valves," **Appl. Phys. Lett.**, Vol. 19, p. 335 (1971); and C. Stein and R. Kashnow, "A Two-Frequency Coincidence Addressing Scheme for Nematic-Liquid-Crystal Display," **Appl. Phys. Lett.**, Vol. 19, p. 343 (1971).

[21] M. Schiekel and K. Fahrenschon, "Deformation of Nematic Liquid Crystals with Vertical Orientation in Electrical Fields," **Appl. Phys. Lett.**, Vol. 19, p. 391 (1971); R. A. Soref and M. J. Rafuse, "Electrically Controlled Birefringence of Thin Nematic Films," **J. Appl. Phys.**, Vol. 43, p. 2029 (1972); F. J. Kahn, "Electric-field-Induced Orientational Deformation of Nematic Liquid Crystals: Tunable Birefringence," **Appl. Phys. Lett.**, Vol. 20, p. 199, (1972); and M. Hareng, E. Leiba, and G. Assouline, "Effet du Champ Electrique sur la Biréfringence de Cristaux Liquides Nématiques," **Mol. Cryst. and Liq. Cryst.**, Vol. 17, p. 361 (1972).

[22] M. Schadt and W. Helfrich, "Voltage-Dependent Optical Activity of a Twisted Nematic Liquid Crystal," **Appl. Phys. Lett.**, Vol. 28, p. 127 (1971).

[23] G. H. Heilmeier and L. A. Zanoni, "Guest-Host Interactions in Nematic Liquid Crystals. A New Electro-Optic Effect," **Appl. Phys. Lett.**, Vol. 13, p. 91 (1968).

[24] I. Haller, H. A. Huggins, and M. J. Freiser, "On the Measurement of Indices of Refraction of Nematic Liquids," **Mol. Cryst. and Liq. Cryst.**, Vol. 16, p. 53 (1972).

[25] D. J. Channin, "Optical Waveguide Modulation Using Nematic Liquid Crystals," **Appl. Phys. Lett.**, Vol. 22, p. 365 (1973).

[26] J. P. Sheridan, J. M. Schnur, and T. G. Giallorenzi, "Electro-Optic Switching in Low-Loss Liquid Crystal Waveguides," **Appl. Phys. Lett.**, Vol. 22, p. 560 (1973).

[27] R. A. Kashnow and C. R. Stein, "Total-Reflection Liquid-Crystal Electro-Optic Device," **Appl. Optics,** Vol. 12, p. 2309 (1973).

[28] G. Assouline, A. Dmitrieff, M. Hareng, and E. Leiba, "Diffraction d'un Faisceau Laser par un Cristal Liquide Nématique Souvris à un champ Electrique," **C. R. Acad. Sci.**, Vol. B271, p. 857 (1970).

[29] W. Helfrich, "Orientation Pattern of Domains in Nematic p-azoxyanisole," **J. Chem. Phys.**, Vol. 51, p. 2755 (1969).

[30] T. O. Carroll, "Liquid-Crystal Diffraction Grating," **J. Appl. Phys.**, Vol. 43, p. 767 (1972).

[31] C. Deutsch and P. N. Keating, "Scattering of Coherent Light from Nematic Liquid Crystals in the Dynamic Scattering Mode," **J. Appl. Phys.**, Vol. 40, p. 4049 (1969); and Orsay Liquid Crystal Group, "Viscosity Measurements by Quasi-Elastic Light Scattering in p-azoxyanisole," **Mol. Cryst. and Liq. Cryst.**, Vol. 13, p. 187 (1971).

[32] P. A. Penz, "Order Parameter Distribution for the Electrohydrodynamic Mode of a Nematic Liquid Crystal," **Mol. Cryst. and Liq. Cryst.**, Vol. 15, p. 151 (1971).

[33] E. Jakeman and P. N. Pusey, "Light Scattering from Electrohydrodynamic Turbulence in Liquid Crystals," **Phys. Lett.**, Vol. 44A, p. 456 (1973); and F. Scudieri, M. Bertolotti, and R. Bartolino, "Light Scattered by a Liquid Crystal: A New Quasi-Themal Source," **Applied Optics,** Vol. 13, p. 181 (1974).

[34] D. Meyerhofer and E. F. Pasierb, "Light Scattering Characteristics in Liquid Crystal Storage Materials," **Mol. Cryst. and Liq. Cryst.**, Vol. 20, p. 279 (1973).

[35] R. B. MacAnally, "Liquid Crystal Displays for Matched Filtering," **Appl. Phys. Lett.**, Vol. 18, p. 54 (1971).

[36] G. W. Taylor and W. F. Kosonocky, "Ferroelectric Light Valves for Optical Memories," **Ferroelectrics,** Vol. 3, p. 81 (1972).

[37] H. J. Caulfield and R. A. Soref, "Optical Contrast Enhancement in Liquid Crystal Devices by Spatial Filtering," **Appl. Phys. Lett.**, Vol. 18, p. 5 (1971).

[38] E. Tomkins, "Liquid Crystal Viewing Screen," Opt. Soc. Am. Meeting, Tucson, Ariz. (1971).

[39] A. Sussman, "Illumination Scheme for Liquid Crystal Displays," U.S. Patent pending.

[40] R. A. Kashnow and H. S. Cole, "Electrohydrodynamic Instabilities in a High-Purity Nematic Liquid Crystal," **J. Appl. Phys.**, Vol. 42, p. 2134 (1971).

[41] M. Hareng, G. Assouline, and E. Leiba, "La Biréfringence Electriquement Contrôlée dans les Cristaux Liquides Nématiques," **Appl. Optics,** Vol. 11, p. 2920 (1972).

[42] L. T. Creagh and A. R. Kmetz, "Performance Advantages of Liquid Crystal Displays with Surfactant-produced Homogeneous Alignment," Soc. for Information Display, 1972 International Symp. Dig. Tech. Papers (Lewis Winner, New York), p. 90; and F. J. Kahn, "Orientation of Liquid Crystals by Surface Coupling Agents," **Appl. Phys. Lett.**, Vol. 22, p. 386 (1973).

[43] G. Assouline, M. Hareng, and E. Leiba, "Liquid Crystal and Photoconductor Image Converter," **Proc. IEEE,** Vol. 59, p. 1355 (1971); and M. Hareng, G. Assouline, and E. Leiba, "Affichage Bicolore à Cristal Liquide (Two Color Liquid-Crystal Display)," **Electron. Lett.**, Vol. 7, p. 699 (1971).

[44] T. Shimojo, K. Matsuda, and K. Kasano, "Singular Electro-Optical Characteristics of Liquid Crystal Display with Interdigital Electrodes," **S.I.D. International Symp. Digest,** 1973 (p. 36).

[45] R. A. Kashnow, "Thickness Measurements of Nematic Liquid Layers," **Rev. Sci. Inst.**, Vol. 43, p. 1837 (1972).

[46] J. A. Castellano and M. T. McCaffrey, "Liquid Crystals IV. Electro-Optic Effects in p-alkoxybenzylidene-p'-aminoalkyphenones and Related Compounds," in **Liquid Crystals and Ordered Fluids,** ed. J. F. Johnson and R. S. Porter, Plenum Press, New York, p. 293 (1970).

[47] U. Bonne and D. P. Cummings, "Properties and Limitations of Liquid Crystals for Aircraft Displays," Contract #N00014-71-C-0262, ONR Task No. NR 215-173, Honeywell, Inc., Oct. 1972, Chap. VII.

[48] G. H. Heilmeier, J. A. Castellano, and L. A. Zanoni, "Guest-Hose Interactions in Nematic Liquid Crystals," **Mol. Cryst. and Liq. Cryst.**, Vol. 8, p. 293 (1969).

[49] J. Dryer, "Liquid Crystal Optical Devices," Reported at Second International Liq. Cryst. Conf., Kent, Ohio, 1968.

[50] H. DeVries, "Rotary Power and Other Properties of Certain Liquid Crystals," **Acta. Cryst.**, Vol. 4, p. 219 (1951).

[51] C. B. Burckhardt, M. Schadt, and W. Helfrich, "Holographic Recording with an Electro-Optic Liquid Crystal Cell," **Appl. Optics,** Vol. 10, p. 2196 (1971).

[52] D. W. Berreman, "Optics in Smoothly Varying Anisotropic Planar Structures: Application to Liquid-Crystal Twist Cells," **J. Opt. Soc. Am.,** Vol. 63, p. 1374 (1973).

[53] G. H. Heilmeier, "Some Cooperative Effects in Butyl p-Anisylidene-p-Amino Cinnamate," in **Ordered Fluids and Liquid Crystals,** Advances in Chemistry Series #63, p. 68, American Chemical Society, Washington, D.C. (1967); A. Takase, S. Sakagami, and M. Nakamizo, "Light Diffraction in a Nematic Liquid Crystal with Positive Dielectric Anisotropy," **Japan J. Appl. Phys.,** Vol. 12, p. 1255 (1973); W. H. DeJeu and C. J. Gerritsma, "Electrohydrodynamic Instabilities in Some Nematic Azoxy Compounds with Dielectric Anisotropies of Different Sign," **J. Chem. Phys.,** Vol. 56, p. 4752 (1972); and Ref. 4.

[54] R. Williams, "Domains in Liquid Crystals," **J. Chem. Phys.,** Vol. 39, p. 384 (1963).

[55] P. A. Penz, "Voltage-Induced Vorticity and Optical Focusing in Liquid Crystals," **Phys. Rev. Lett.,** Vol. 24, p. 1405 (1970).

[56] P. A. Penz and G. W. Ford, "Electromagnetic Hydrodynamics of Liquid Crystals," **Phys. Rev.,** Vol. 6A, p. 414 (1972).

[57] H. Greubel and U. Wolff, "Electrically Controllable Domains in Nematic Liquid Crystals," **Appl. Phys. Lett.,** Vol. 19, p. 213 (1971); and L. K. Vistin, "New Electrostructural Phenomenon in Liquid Crystals of Nematic Type," **Sov. Phys. Crys.,** Vol. 15, p. 514 (1970).

[58] A. Sussman, unpublished results.

[59] Orsay Liquid Crystal Group, "Hydrodynamic Instabilities in Nematic Liquids Under ac Electric Fields," **Phys. Rev. Lett.,** Vol. 25, p. 1642 (1970).

[60] R. A. Kashnow and J. E. Bigelow, "Diffraction from a Liquid Crystal Phase Grating," **Appl. Optics,** Vol. 12, p. 2302 (1973).

[61] Y. Galerne, G. Durand, M. Veyssie, and V. Pontikis, "Electrohydodynamic Instability in a Nematic Liquid Crystal: Effect of an Additional Stabilizing ac Electric Field on the Spatial Period of 'Chevrons'," **Phys. Lett.,** Vol. 38A, p. 449 (1972).

[62] A. Sussman, "Secondary Hydrodynamic Structure in Dynamic Scattering," **Appl. Phys. Lett.,** Vol. 21, p. 269 (1972).

[63] J. Nehring and M. S. Petty, "The Formation of Threads in the Dynamic Scattering Mode of Nematic Liquid Crystals," **Phys. Lett.,** Vol. 40A, p. 307 (1972).

[64] L. Goodman, "Light Scattering in Electric-Field Driven Nematic Liquid Crystals," Soc. for Information Display 1971 International Symp. Dig. Tech. Papers, (Lewis Winner, New York), p. 124. See also References [31] and [47].

[65] L. T. Creagh, "Nematic Liquid Crystal Materials for Displays," **Proc. IEEE,** Vol. 61, 814 (1973); and Eastman Liquid Crystal Products, Bulletin JJ-14 (1973).

[66] G. Assouline and E. Leiba, "Cristaux Liquides," **Rev. Tech. CSF,** Vol. 1, p. 483 (1969).

[67] J. D. Margerum, J. Nimov, and S.-Y. Wong, "Reversible Ultraviolet Imaging with Liquid Crystals," **Appl. Phys. Lett.,** Vol. 17, p. 51 (1970).

[68] D. H. White and M. Feldman, "Liquid Crystal Light Valves," **Electron Letters,** Vol. 6, p. 837 (1970).

[69] J. D. Margerum, T. D. Beard, W. P. Bleha, Jr., and S.-Y. Wong, "Transparent Phase Images in Photoactivated Liquid Crystals," **Appl. Phys. Lett.,** Vol. 19, p. 216 (1971).

[70] A. D. Jacobson, "Photo-Activated Liquid Crystal Valve," Soc. for Information Display, 1972 International Symp., Dig. Tech. Papers (Lewis Winner, New York), p. 70.

[71] A. Rose, "The Role of Space-Charge-Limited Currents in Photoconductivity-controlled Devices," **IEEE Trans. on Electron Dev.,** Vol. ED19, p. 430 (1972).

[72] T. O. Beard, W. P. Bleha, and S.-Y. Wong, "AC Liquid Crystal Light Valve," **Appl. Phys. Lett.,** Vol. 22, p. 90 (1973).

[73] A. Sussman, "Dynamic Scattering Life in the Nematic Compound p-Methoxybenzylidene-p-amino phenyl acetate as Influenced by the Current Density," **Appl. Phys. Lett.,** Vol. 21, p. 126 (1972).

Dispersion-Limited Modulation Bandwidths of Optical Fibers

James P. Wittke

RCA Laboratories, Princeton, N.J. 08540

Abstract—The information-carrying capacity of an optical fiber is often limited by dispersive effects in the fiber. For relatively short transmission paths (under 500 meters) modal dispersion, caused by the difference between group velocities of the different propagating modes, is dominant. Measurements of the modulation transfer functions of three types of optical fiber, two step-index filters and a graded-index fiber, have been made using both frequency- and time-domain techniques. A simple ray model predicts many of the properties of the lowest-loss step-index fiber, while the assumption of strong attenuation in the higher-order modes is necessary to explain the data on the high-aperture step-index fiber. The graded-index fiber shows anomalously large pulse broadening.

1. Introduction

The literature contains many reports of observations of dispersion in optical fibers.[1-15] Most of these consist of measurements of the pulse broadening resulting from propagation down a given length of fiber, although a few[5, 15] measure instead the amplitude part of the modulation (or frequency) transfer function[16] (MTF) of the fiber. While

pulse broadening information permits an estimate to be made of the bandwidth capability of such fibers, a communications systems designer needs more detailed information on both the amplitude and phase aspects of the MTF if he is to optimize the signal waveforms and the overall system equalization for maximum information transfer capability. This paper gives such complete MTF's for three types of solid glass fibers now of research interest: a low numerical aperture, low-loss, step-index fiber; a relatively high aperture, step-index fiber (of considerably greater loss); and a graded-index fiber. The data given apply directly only to the three specific fibers measured, and great care should be used in extrapolating the results to other fibers, especially ones of different lengths. Nevertheless, a comparison of the results obtained on these three classes of fiber can provide useful information to those interested in applying the developing optical fiber technology to practical communications problems.

The data have been obtained by both time- and frequency-domain measurements. Where possible, an attempt has been made to relate the experimental results to available theory. A simple model of a step-index fiber is seen to predict many of the features of the observations.

2. Experimental Methods and Results

Fibers

Three types of fibers were studied. One consists of a single, low-loss, step-index fiber 350 meters long.* It has a core diameter of approximately 90 μm and a numerical aperature of 0.14. The attenuation, as measured by the manufacturer, is 6 dB/km in the low-loss region near 830 nm. The overall fiber diameter is about 120 μm; the fiber is clad with a thin protective plastic coating. The V-parameter[17] for this fiber is 47.7, giving a total of about 1140 propagating modes. Good flat faces were obtained by cleavage, using recommended techniques.[18] This fiber is considered representative of the best current fiber technology, as applied to low-aperture, step-index fibers.

The second type of fiber studied consists of high-aperture, step-index fibers 30.5 meters long.+ These were bundled to form a cable, 1.1 mm in diameter, consisting of about 180 fibers. Each has a core diameter of 60 μm and a numerical aperture of 0.67. The V-parameter is 152.2, giving 11600 propagating modes. The attenuation, as quoted by the manufacturer, is 720 dB/km. The fibers have a 5-μm cladding

* Supplied by Corning Glass Works.

+ Manufactured by Galileo Electro-Optics Corp.

and are close packed, as shown in Fig. 1. Since the (slot-shaped) effective-source size used had a length of 130 μm, the measurements on this type of fiber always consisted of an average of the properties of two (or perhaps three) individual fibers. As seen in the figure, the fibers were not very uniform in their transmission properties. Particular fibers were not selected for the measurements; the source was moved relative to the (carefully polished) fiber-bundle end until a (local) transmission maximum was found. This procedure may account for some of the nonreproducibility of the data noted below.

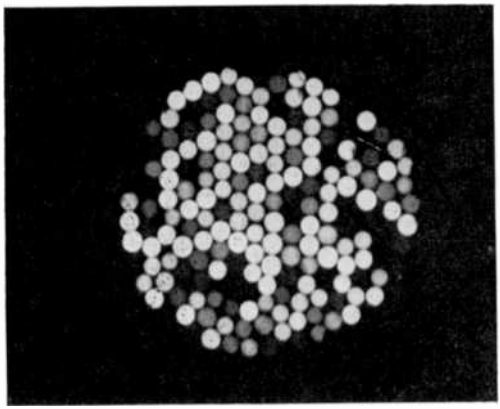

Fig. 1—Magnified image of the end of a 30.5-meter high-aperture fiber bundle illuminated at the other end by a diffuse, incoherent light source. The differences in apparent fiber brightness are due to differing losses in the individual fibers.

The last type of fiber used was a graded-index fiber 100 meters long.* This has an effective input diameter of 30 μm and effective numerical aperture of about 0.15. The number of focused modes is about 220.[19] The nominal attenuation is 50 dB/km at 850 nm. The glass fiber is covered with a protective plastic coating 1.5 mm in diameter.

Pulse Measurements

The first method used to determine the MTF's of the fibers was to propagate a short optical pulse (of known input shape) down the various fibers and measure the output pulse shape. Insofar as the

* Manufactured by Nippon Electric Company under the trade-name SELFOC SLC-100.

fiber link and the source and detection elements can be considered linear elements, the output pulse shape can be obtained by convoluting the transform of the MTF with the input pulse. (That the fiber itself can be treated in this way has been shown by Personick.[20]) Under the conditions of the measurements, the assumption of system linearity is an excellent one. Therefore, the MTF can be obtained by a deconvolution of output and input pulse shapes. This procedure eliminates the effects of pulse distortion introduced either by the light source or the detection electronics. (Care must be taken to ensure that the latter are operated in a strictly linear fashion.)

An RCA development $Ga_xAl_{1-x}As$ double heterojunction light-emitting diode (LED) was used as the source. While, in principle, a 'slow' LED that has little response at high drive frequencies can be used, in practice, accurate data can only be obtained with a source with appreciable response at frequencies of hundreds of megahertz. Preliminary data concerning the type of diode used in these measurements was presented at the International Electron Device Meeting, Washington, D.C., December, 1973.[21] The LED can produce pulses 3.3 nsec wide (at half-power), after detection, when driven by 1.0-nsec current pulses.* An incoherent source was used because its angular beam pattern completely fills the acceptance cone of even the high-aperture fiber, thus ensuring approximately uniform excitation of all propagating modes. This uniformity was not obtained when an injection laser source was used. Although 2.3-nsec pulses (detection-limited) could be observed with the laser, the laser beam did not fill the numerical aperture of all the fibers.

The LED was coupled into each fiber by bringing it into near contact with the end of the fiber (or bundle) and adjusting its position to secure maximum transmitted light through the fiber. The LED had a junction size of 125 × 250 μm. The light emission from one of the shorter facets was coupled into the fiber. Since the high-aperture fibers were only 70 μm in diameter (including cladding), light was coupled into two or three fibers at one time with this bundle of fibers.

A high-speed, S-20 response, photomultiplier tube was used to detect the pulses, either transmitted through the fiber or direct from the LED. Saturation of the photocathode was avoided. The photomultiplier was connected, via a short length of low-loss 50-ohm coaxial cable, to a high-speed oscilloscope.+ Oscilloscope photographs provided a permanent record of the pulses for subsequent analysis.

* A Spencer-Kennedy Laboratories Model 503A pulser was used.

+ A Tektronix Model 7704A oscilloscope with a Model 7A19 plug-in amplifier was used.

The photographed pulse shapes were Fourier-analyzed on a digital computer. From this, the deconvolution could be readily accomplished. The results are shown in Figs. 2-4. Part (a) of each figure shows the amplitude part of the MTF's, normalized to unity for unmodulated light. The response drops off at high frequencies due to dispersive

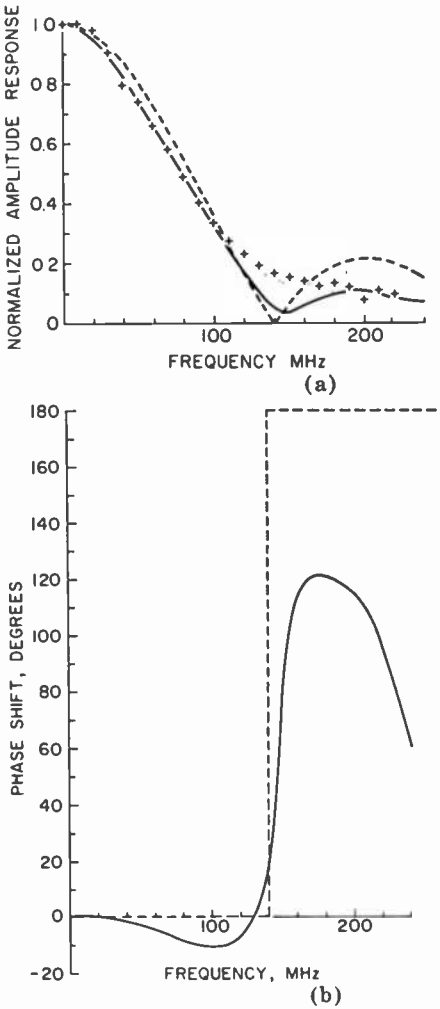

Fig. 2—(a) Relative amplitude response of a 350-meter, low-loss, low-aperture, step-index fiber. The solid curve is the MTF measured using a pulse technique; the data points were taken using sinusoidal modulation; the dashed curve is for a sin $(\omega\tau/2)/(\omega\tau/2)$ MTF. (b) Phase response of a 350-meter, low-loss, low-aperture, step-index fiber. The solid curve was determined from pulse measurements; the dashed curve corresponds to the phase characteristic for a sin $(\omega\tau/2)/(\omega\tau/2)$ MTF.

effects in the fiber. It should be noted that the three figures refer to three different lengths of fiber. To the degree that the MTF varies linearly with fiber length (an assumption to be discussed below), a direct comparison between Figs. 3 and 4 and Fig. 2 requires that the frequencies of Figs. 3 and 4 be divided by 11.5 and 3.5, respectively.

Since the exact travel times of the pulses down the fibers are of no particular interest, the phase parts of the MTF have been adjusted by an additive linear variation (with frequency)[16] to make their slopes zero at low frequencies: (Parts (b) of Figs. 2, 3, and 4).

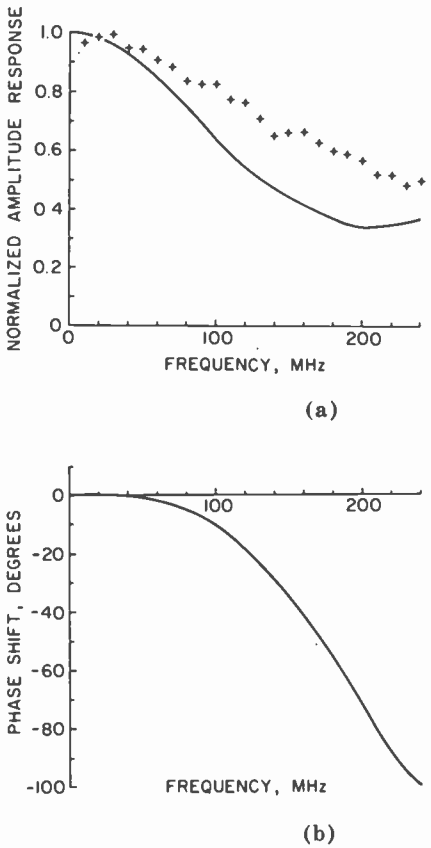

Fig. 3—(a) Relative amplitude response of 30.5-meter, high-aperture, step-index fibers in a compact bundle. The solid curve was determined from pulse measurements; the data points were taken using sinusoidal modulation. (b) Phase response of 30.5-meter, high-aperture, step-index fibers in a compact bundle as determined from pulse measurements.

Sinusoidal Measurements

While pulse measurements are relatively easy to make and give phase as well as amplitude response information, they are susceptible to systematic errors introduced by electrical mismatches, errors in measuring photographed pulse shapes, and spurious effects introduced in the numerical treatment of the data. A check on the pulse results was, therefore, obtained by measurements of the sinusoidal modulation of the transmitted light. For these measurement, the same high-speed LED used in the pulse measurements is biased by a dc current of 200 mA, so that a small sinusoidal current modulation produces a linearly related sinusoidal output light variation.

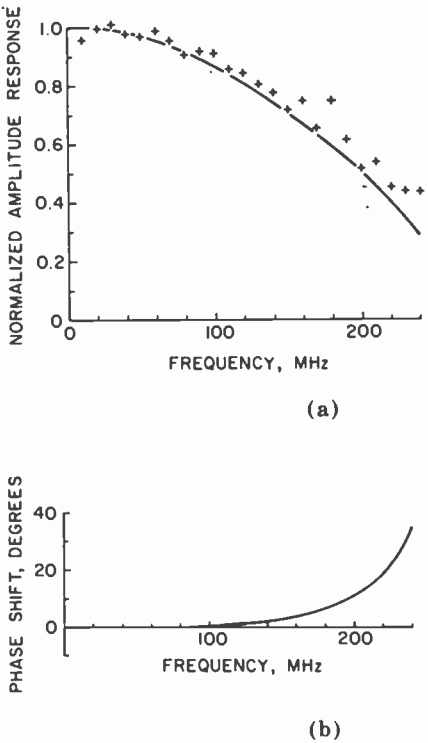

Fig. 4—(a) Relative amplitude response of a 100-meter, graded-index fiber. The solid curve was determined from pulse measurements; the data points were taken using sinusoidal modulation. (b) Phase response of a 100-meter graded-index fiber determined from pulse measurements.

The equipment used in this alternative method is shown in Fig. 5. The rf component of the drive current is supplied by a signal generator; the rf current to the LED is monitored with a broad-band current probe and high-speed oscilloscope. Chokes in the matching network isolate the rf and dc bias currents. The sinusoidally modulated light from the face of the LED is coupled, as before, into the end of the fiber to be measured. A silicon avalanche photodiode is used to detect the light transmitted by the fiber. The coupling between fiber and detector is adjusted to keep a constant detected dc component. The detector output is amplified by a broadband preamplifier whose output is fed through a 10-dB-attenuation 50-ohm matching pad to a spectrum analyzer. The spectrum analyzer functions as a low-noise, narrow-band, tunable receiver for the modulation signal.

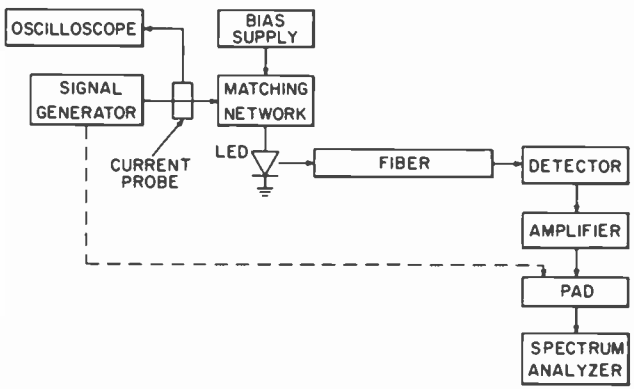

Fig. 5—Block diagram of the equipment used to measure the amplitude part of the MTF of fibers using sinusoidally modulated light.

The test procedure is as follows. With the signal generator level set to produce a 32 mA peak-to-peak current modulation at the LED, the gain of the spectrum analyzer is adjusted to produce a full-scale deflection on the display oscilloscope at a fixed modulation frequency. The (calibrated) signal generator is then disconnected from the LED and applied directly to the pad in front of the spectrum-analyzer receiver. The signal level is now adjusted to again produce a full-scale deflection on the display, and the required signal level is recorded. In this way, possible variations in the sensitivity of the spectrum analyzer with frequency are eliminated as a source of error. This process is repeated at a different modulation frequency until the range of frequencies up to 240 MHz has been (randomly) sampled.

To eliminate errors introduced by the frequency characteristics of the LED and detector, the above measurements were also made on a 6.1-meter length of low-loss, low-aperture fiber. The short length of fiber is useful in providing spatial separation of the high-level LED drive circuitry and the sensitive detection circuits, thereby eliminating electrical pick-up problems. Since such a short fiber is not expected to effect the measured system frequency response, this set of measurements can then be used to calibrate the frequency response of the system and hence to correct the measurements of the MTF's of the three fibers being tested. The amplitude parts of the MTF's obtained with this sinusoidal modulation technique are shown in Figs. 2-4, as individual data points.

In principle, by observing the *phase* of the sinusoidal signal (after propagation through the fiber, detection, amplification, and correction for phase shifts introduced in the light source and detection circuits), the phase part of the MTF could also be measured. In practice, however, this is very difficult. The signal level after propagation through the fiber is very low, and, with the broad-band circuits used, the noise level is relatively high, making accurate phase measurements difficult. Nevertheless, an attempt was made.

Phase measurements were made on only the low-loss, low-aperture step-index fiber, because, despite its greater length, its very low loss permitted a stronger signal than the other fibers. The measurement was made by comparing the phase of a signal taken from the LED drive circuit to that of the signal following detection and amplification (after transmission through the fiber) as the frequency of the modulation was varied from 0 to 80 MHz. Higher frequencies were not used because the signal-to-noise ratio became too poor. The measurements were then repeated with the fiber removed, but all electrical circuits, etc. unchanged. By substracting out the phase shifts due to the circuitry, the phase response of the fiber alone could in principle be determined. In practice, however, the results of this process were not very satisfactory. Since the optical path was 350 meters long and had an effective index of about 1.5, one expects, even in the absence of dispersion, a phase shift of about 360° for each change in frequency of 570 KHz, or a total shift of some 1.5×10^5 degrees in going from dc to 240 MHz. The difficulty is that what one is really interested in is the *deviations from linearity* of the frequency-dependent phase shift. As seen from Fig. 2(b), the maximum deviation to be expected is about 10° (below 80 MHz) or about one part in 15,000. This apparently was beyond the capability of the technique, which only indicated that any differential phase variations were less than about

8°/MHz. These measurements, therefore, while compatible with the phase data obtained from the pulse technique, are quite inconclusive.

Beam Pattern Measurements

To ensure that the fiber apertures were being fully illuminated, far-field angular beam patterns were determined for both the light issuing from the three types of fibers, and for the LED itself. These were obtained by scanning a photomultiplier with a small pinhole in front of it across the beam from the LED or fiber. The results are shown in Fig. 6.

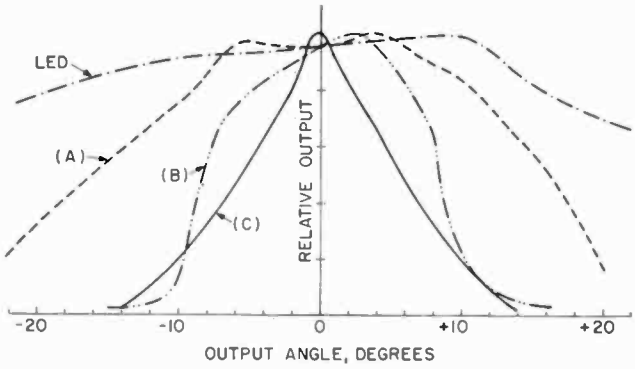

Fig. 6—Far-field beam patterns of the LED used to illuminate the fibers, and for the (transmitted) beam patterns for the three types of fibers. The pattern for the LED is for angles perpendicular to the plane of the junction: the radiation pattern is essentially flat over 180° in the plane of the junction. Curve (A) is for the high-aperture, step-index fiber; curve (B) is for the low-aperture, step-index fiber; and curve (C) is for the graded-index fiber.

3. Discussion

Comparison of Measurement Techniques

The results obtained by the two measurement techniques are in good agreement, except in the case of the high-aperture, step-index fiber bundle, where the pulse measurements indicate a significantly smaller bandwidth than the data obtained with sinusoidal modulation. To try to understand this discrepancy, consider first the processes of material and modal dispersion.[22, 23] Since the LED coupling method and the LED beam patterns were the same for both pulse and sinusoidal measurements, the same mode coupling distribution was obtained in both techniques, and so modal dispersion should not contribute to this

discrepancy. The situation with regard to material dispersion is not so simple. Fig. 7 shows the spectra of the LED under the conditions of the measurements. Under pulsed conditions, the spectrum narrows and shifts to shorter wavelengths. These effects can be explained in terms of conduction band-filling under the strong excitation conditions found in the pulse measurements. The result is that the pulsed measurements should show somewhat *reduced* dispersive effects and, hence, a somewhat broader (in frequency) MTF. However, Fig. 3 shows just the opposite effect—the pulse-determined MTF is narrower than expected from the sinusoidal measurements.

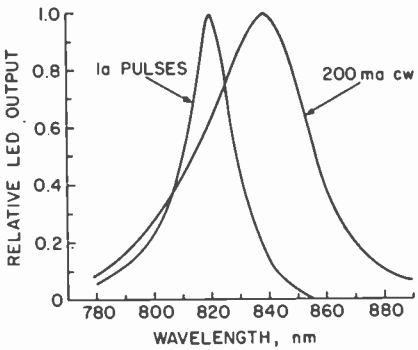

Fig. 7—Emission spectra of the LED used in all measurements, under pulsed and cw excitation conditions. The pulses were at a sufficiently low repetition rate to eliminate heating effects.

The cause of the discrepancy between the pulse and sinusoidal modulation measurements is thus not obvious. However, considering the variation in transmission properties from fiber to fiber in the high-aperture bundle (see Fig. 1), it seems reasonable to seek the cause here, rather than in a serious difficulty in the measurement techniques. The quite good agreements obtained in the cases of the two other types of fiber tend to support this conclusion.

Material Dispersion

Gloge[23] has shown that in weakly guiding fibers, such as the step-index fibers studied here, one can effectively treat material and model dispersion effects separately. Material dispersion has been considered in detail for several glasses by DiDomenico.[24] His data indicate that in predominantly silica fibers, such as the low-aperture one studied here, material dispersion should broaden pulses from our LED source

by about 2.3 nsec/km for the pulsed operation corresponding to Fig. 7. The "equivalent broadening" (as reflected in the MTF) for sinusoidal operation, (i.e., the broader emission spectrum also shown in Fig. 7), is 4.4 nsec/km. For the 350-meter length of our fiber, the corresponding values are 0.8 and 1.5 nsec. This is clearly not the dominant limiting factor in the MTF of the low-aperture fiber, as can be seen from Fig. 8. Here the time response of this fiber has been computed for an impulse (delta function) excitation, using the data of Fig. 3. The impulse is seen to be broadened to about 6.5 nsec by the fiber, a much larger value than that computed from the material dispersion.

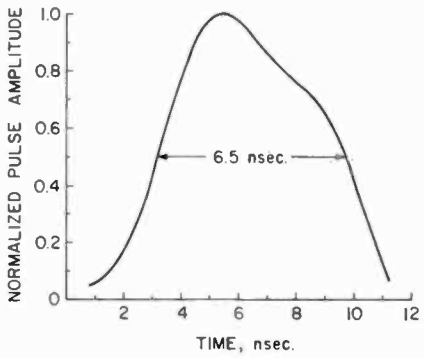

Fig. 8—Computed response of the low-aperture step-index fiber to a delta-function input.

For the high-aperture fiber, its flint glass core has considerably greater dispersion, resulting in a broadening of about 12 nsec/km. However, for the short length measured, this corresponds to only 0.4 nsec broadening, and, hence, material dispersion can be neglected for this fiber too.

The same conclusion applies to the graded index glass; the observed MTF is not primarily determined by the material dispersion of the fiber.

Modal Dispersion

It is apparent that the modal dispersion in these fibers is the dominant factor in determining their MTF's. A simple model[5] for modal broadening assumes that the modal distribution and excitation are such that light propagates (without loss) with a *uniform* spread of transit times between the fastest (on axis) mode and the slowest (meridional)

mode. Then an impulse excitation would produce a rectangular output pulse of width

$$\tau = \frac{L\Delta n}{c},$$

where Δn is the core-cladding index difference. The corresponding MTF is[5]

$$S(\omega) = \frac{\sin\left(\frac{\omega\tau}{2}\right)}{\left(\frac{\omega\tau}{2}\right)}.$$

In Fig. 2, this model has been fitted to the data for the low-aperture fiber. The fit is remarkably good: not only is the zero of the model MTF at $f_c = 1/\tau$ seen in the measurements, but the overall fit of the curve is quite good. A sudden phase shift, of about 180°, at this frequency is also seen. The core-cladding index difference of the measured fiber is about 0.007. This corresponds to a time-spread of $\tau = 8.2$ nsec and a critical frequency $f_c = 122$ MHz. To fit the data, the choice $f_c = 140$ MHz had to be made. Thus, while this simple model roughly fits the data, the measured MTF shows better high frequency characteristics than predicted, by about 15%. This type of behavior, i.e., measured pulse broadenings less than predicted by the simple model, has often been observed in previous work,[1,3,4,10,13] and is in striking agreement with similar measurements by Gloge *et al.*[5] where a critical frequency 12% higher than predicted was observed. On the other hand, other work[6,7,9] indicates essential agreement between experiment and the simple model.

The input and output pulses for the low-aperture, step-index fiber are shown in Fig. 9. A "tail" is observable on both pulses, but is more pronounced in the case of the transmitted pulse. Because some (slight) circuit ringing was observed, it was felt that at least a portion of this tail might be due to some such spurious cause. To see the effect of this, and to get some idea of the sensitivity of the numerical analysis to slight errors in the input wave forms, the data were re-analyzed using the artifically truncated pulse shown by the dashed line in the figure. The results of this procedure were as ex-

pected; the amplitude response part of the MTF was altered slightly, in the direction of making it closer to the model MTF. That is, the "zero-dip" was sharper and deeper, and the following, high-frequency response maximum was somewhat higher. As concerns phase, the weak "negative dip" below the critical frequency was reduced, and the height of the phase jump near the critical frequency was increased somewhat. There was, however, a sharper phase fall-off at high frequencies than in the previous case. The conclusion is that the effects of even as large a change as truncating the pulse tail does not seriously alter the results as reported.

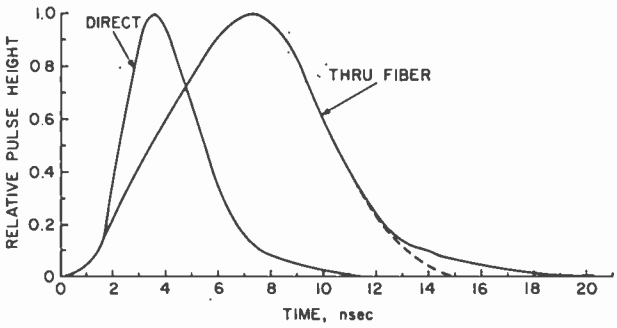

Fig. 9—Detected optical pulse shapes: input pulse shape direct from LED to detector, and output pulse shape after transmission through 350 meters of low-aperture step-index fiber. The dashed portion at the end of the output pulse shows an (arbitrary) pulse truncation used to study the sensitivity of the analysis to measurement errors.

It is also interesting to note that the data measured sinusoidally for this low-aperture fiber can be fit quite well with a Gaussian MTF. This, of course, does not exhibit any critical frequency, as does the sin $(\omega\tau/2)/(\omega\tau/2)$ model. This was also observed by Personick *et al*[15] using a similar sinusoidal technique; their data also start to deviate from a Gaussian at higher frequencies at essentially the same relative frequency as do the data of Fig. 2.

We have no good explanation of the observation on the low-aperture fiber that measured pulse broadening is less than expected on the basis of the model. While the model is clearly a rather gross oversimplification of the actual situation occurring in an actual fiber, nevertheless one might expect the measured pulse broadening to *exceed* the prediction. This is because the model is based on meridional rays only, and skew rays, neglected in the model, would have even longer propagation times.

The usual explanations are: (1) only a subset of all possible modes may be excited;[3] (2) "slower" modes may be attenuated strongly by repeated interaction with irregularities at the core-cladding interface;[4] or (3) mode conversion may narrow the transmitted pulse.[20] Let us consider these possibilities in order. As Fig. 6 shows, the LED beam pattern more than fills the effective acceptance cone of all the fibers. (While the numerical aperture of the high-index fiber corresponds to a half-angle of 42°, only the central 20° or so appear to be useful, as shown in Fig. 6; in any case, the LED pattern is broad enough to fill even the 42° cone.) It therefore does not appear that the observation of unexpectedly small pulse broadening can be explained on the basis of not exciting all possible propagation modes.

The second possibility, that the higher-order 'slower' modes may be more strongly attenuated by repeated interaction with the loss mechanism at the core-cladding interface, seems the most likely one to explain our data on step-index fibers. Gloge *et al*[4] have used this explanation for their data. Moreover, Gambling *et al*[12] have measured increased attenuation in these modes, using a low-loss liquid-core fiber. It seems reasonable to expect such higher loss in the higher-order modes, because in these modes the energy density at the core-cladding interface is much higher[17] than for the low order modes.

Finally, the beam pattern for the high-aperture, step-index fiber (Fig. 6) is much narrower than the model predicts. Since, as mentioned, the full aperture for 'propagating' modes was illuminated by the source, the reduced cone of radiation observed at the output can best be explained by the selective attenuation of the higher-order modes. This explanation is compatible with the data of Fig. 3. Fitting the simple model (without very good agreement at the higher frequencies) gives an 'observed' spread of transit times of about 5.6 nsec from the pulse data, or about 3.3 nsec from the sinusoidal measurement technique. These values are in poor agreement with the expected value of about 14 nsec, calculated from the known indices of the core and cladding. However, if we ask what 'equivalent' beam half-angles would give the 'observed' 5.6 (or 3.3) nsec broadening, we find an angle of 25° (or 19°), in good agreement with the measured transmitted beam pattern given in Fig. 6.

The third possible effect that can narrow the observed pulses over those given by the model is mode-mixing. Personick[20] has shown theoretically, and Chinnock *et al*[14] have shown experimentally, that such an effect certainly occurs. However, for the fiber measured by Chinnock *et al*, fiber lengths of over 500 meters were required before mode mixing effects became evident for excitation at 900 nm. More-

over, if mode-mixing, rather than attenuation of high-order modes, were the dominant effect, it is hard to explain the narrow beam pattern of Fig. 6, curve (A). Thus, in our step-index fibers, evidence of significant pulse-narrowing due to mode-mixing does not seem strong.

The most puzzling results obtained in the present series of measurements concern the graded-index fiber. There are sound theoretical[19, 25, 26] reasons for expecting the modal dispersive effects of (quasi-parabolic) graded-index fibers to be much less than those of step-index fibers. There is also considerably experimental evidence that this is so.[10, 11, 13] Indeed, the expression[26] for modal broadening

$$\tau \approx \frac{L}{2nc} (\Delta n)^2,$$

where Δn is the difference between the (high) index on axis and that of the glass at the periphery of the graded region, gives 0.05 nsec for the modal broadening. An additional broadening due to material dispersion is expected.[11] This amounts to some 0.3-0.7 nsec, depending on which spectral width (Fig. 7) is used. While large compared to the expected modal dispersion, this is still negligible compared to the observed 'equivalent broadening' of about 3.6 nsec derived from the data of Fig. 4.

That there is something drastically wrong with the data seems unlikely, in view of the apparent validity of the results obtained with step-index fibers and of the good agreement between the pulse and sinusoidal measurements on the graded-index fiber. Looking elsewhere, then, it might be thought that the method of excitation used would excite either propagation modes in the protective plastic coating or in the outer regions of the glass fiber where the index is essentially constant. Indeed, owing to the small diameter of the graded-index region and the (comparatively) large size of the LED, a considerable fraction of the emitted light is incident on these 'undesirable' regions.

There are good reasons for rejecting these alternatives, however. The fiber used is quite long, 100 meters, and plastics all appear to have much too high absorption losses in such lengths to permit detectible energy after propagation down the protective coating. Propagation in the glass away from the axial graded-index region also seems unlikely (the interface losses at the boundary of glass and plastic would be expected to be too high). Moreover, as Fig. 6 indicates, the transmitted beam has a pattern upon exiting the fiber that is much narrower than that of the other fibers. It is also of a characteristically

more 'pointed' shape, which is to be expected from a fiber with focusing properties, than the 'squarer' shape expected and observed with the step-index fibers. The observed angular beam width is also that expected from the manufacturer's specifications on the guiding properties of this fiber. It therefore appears that the detected optical energy used to determine the MTF of this fiber traveled in the guided modes associated with the graded-index region of the fiber.

4. Summary and Conclusions

Measurements on the MTF's of three types of optical fibers have been made using an LED light source excited in both pulsed and sinusoidal modes. The agreement between the two methods of measurement is quite good, except in the case of the high-aperture step-index fiber, where the two sets of measurements were probably made on different pairs of fibers in the bundle.

The results for the lowest-loss fiber (the low-aperture, step-index, fiber) are in quite good agreement with expectations based upon the simple meridional-ray model often used. A significant (relative) phase shift is observed at a modulation frequency corresponding to the reciprocal of the expected spread of modal pulse transit times.

The results on the high-aperture fiber can be best understood by a picture of strong attenuation of the higher order modes, so that the numerical aperture effective for propagating the signal is, perhaps, only half that expected on the basis of the index discontinuity between core and cladding.

The data on the graded-index fiber are perplexing. While both measurement techniques gave consistent results, they indicate an order of magnitude greater dispersive effects than expected, with a correspondingly narrow (in frequency) MTF. No acceptable explanation has been found for this discrepancy.

Acknowledgments

Constructive comments on the content and form of this paper by A.H. Firester have significantly improved it. The broadband amplifier used with the silicon avalanche detector was designed and built by J. Schroeder and D.R. Patterson. Support by, and discussions with, numerous of the author's other colleagues during this work was also appreciated. The high-speed LED used in this work was of a type developed with ONR support under Contract N00014-73-C-0335.

References:

[1] D. Williams and K. C. Kao, "Pulse Communication Along Glass Fibers," **Proc. IEEE,** Vol. 56, p. 197 (1968).

[2] W. A. Gambling, D. N. Payne, and H. Sunak, "Pulse Dispersion in Glass Fibres," **Elect. Lett.,** Vol. 7, p. 549 (1971).

[3] V. N. Smiley, H. F. Taylor, A. L. Lewis, and D. J. Albares, "Pulse Distortion in Fiber Optic Bundles," **Appl. Opt.,** Vol. 10, p. 2543 (1971).

[4] D. Gloge, A. R. Tynes, M. A. Duguay, and J. W. Hansen, "Picosecond Pulse Distortion in Optical Fibers," **IEEE J. Quant. Elect.,** Vol. QE-8, p. 217 (1972).

[5] D. Gloge, E. L. Chinnock, and D. H. Ring, "Direct Measurement of the (Baseband) Frequency Response of Multimode Fibers," **Appl. Opt.,** Vol. 11, p. 1534 (1972).

[6] D. Gloge, E. L. Chinnock, and T. P. Lee, "Self-Pulsing GaAs Laser for Fiber-Dispersion Measurements," **IEEE J. Quant. Elect.,** Vol. QE-8, p. 844 (1972).

[7] D. Gloge and E. L. Chinnock, "Fiber-Dispersion Measurements Using a Mode-Locked Krypton Laser," **IEEE J. Quant. Elect.,** Vol. QE-8, p. 852 (1972).

[8] D. Schicketanz, "Pulse Broadening in Multimode Fibres Excited by GaAs Lasers," **Elect. Lett.,** Vol. 9, p. 5 (1973).

[9] W. A. Gambling, J. P. Dakin, D. N. Payne, and H. R. D. Sunak, "Propagation Model for Multimode Optical-Fibre Waveguide," **Elect. Lett.,** Vol. 8, p. 260 (1972).

[10] R. Bouillie and J. R. Andrews, "Measurement of Broadening of Pulses in Glass Fibres," **Elect. Lett.,** Vol. 8, p. 309 (1972).

[11] D. Gloge, E. L. Chinnock, and K. Koizumi, "Study of Pulse Distortion in Selfoc Fibres," **Elect. Lett.,** Vol. 8, p. 526 (1972).

[12] W. A. Gambling, D. N. Payne, and H. Matsumura, "Dispersion in Low-Loss Liquid-Core Optical Fibres," **Elect. Lett.,** Vol. 8, p. 568 (1972).

[13] C. A. Burrus, E. L. Chinnock, D. Gloge, W. S. Holden, T. Li, R. D. Standley, and D. B. Keck, "Pulse Dispersion and Refractive-Index Profiles of Some Low-Noise Multimode Optical Fibers," **Proc. IEEE,** Vol. 61, p. 1498 (1973).

[14] E. L. Chinnock, L. G. Cohen, W. S. Holden, R. D. Standley, and D. B. Keck, "The Length Dependence of Pulse Spreading in the CGW-Bell-10 Optical Fiber," **Proc. IEEE,** Vol. 61, p. 1499 (1973).

[15] S. D. Personick, W. M. Hubbard and W. S. Holden, "Measurements of the Baseband Frequency Response of a 1-km Fiber," **Appl. Opt.,** Vol. 13, p. 266 (1974).

[16] M. Schwartz, **Information Transmission, Modulation, and Noise,** Chap. 2, McGraw-Hill Book Co., New York, N. Y. (1959).

[17] D. Gloge, "Weakly Guiding Fibers," **Appl. Optics,** Vol. 10, p. 2252 (1971).

[18] D. Gloge, P. W. Smith, D. L. Bisbee, and E. L. Chinnock, "Optical Fiber End Preparation for Low Loss Splices," **Bell Syst. Tech. J.,** Vol. 52, p. 1579 (1973).

[19] D. Gloge and E. A. J. Marcatili, "Multimode Theory of Graded-Core Fibers," **Bell Syst. Tech. J.,** Vol. 52, p. 1563 (1973).

[20] S. D. Personick, "Time-Dispersion in Dielectric Waveguides," **Bell Syst. Tech. J.,** Vol. 50, p. 843 (1971).

[21] M. Ettenberg, H. F. Lockwood, J. P. Wittke, and H. Kressel, "High Radiance, High Speed $Al_xGa_{1-x}As$ Heterojunction Diodes for Optical Communications," Paper 16.1, **Internat. Elect. Devices Meeting Tech. Digest,** 1973.

[22] F. P. Kapron and D. B. Keck, "Pulse Transmission Through a Dielectric Optical Waveguide," **Appl. Opt.,** Vol. 10, p. 1519 (1971).

[23] D. Gloge, "Dispersion in Weakly Guiding Fibers," **Appl. Opt.,** Vol. 10. p. 2442 (1971).

[24] M. DiDomenico, "Material Dispersion in Optical Fiber Waveguides," **Appl. Opt.,** Vol. 11, p. 652 (1972).

[25] S. Kawakami and J. Nishizawa, "An Optical Waveguide With the Optimum Distribution of Refractive Index with Reference to Waveform Distortion," **IEEE. Trans. Microwave Theory and Tech.,** Vol. MTT-16, p. 814 (1968).

[26] D. Marcuse, "The Impulse Response of an Optical Fiber with Parabolic Index Profile," **Bell Syst. Tech. J.,** Vol. 52, p. 1169 (1973).

Design, Construction, and Testing of a Magnetic Bubble Memory Chip

L. S. Onyshkevych and R. Shahbender

RCA Laboratories, Princeton, N.J. 08540

S. Tomkiel and F. Putzrath

Government and Commercial Systems, Camden, N.J.

Abstract—A 34-bit cylindrical domain (bubble) memory chip with complete functions for read, write, erase, and store operations was designed, fabricated, and tested. Description of the design and fabrication steps and experimental test data are presented.

Introduction

Bubble[1,2] memories potentially offer inexpensive bulk storage, with no moving parts, for replacement of electromechanical bulk stores, such as magnetic drums, discs, and tapes.[3] Fabrication of bubble memory chips utilizes well-developed IC semiconductor technology—metallization and etching. Bubble devices, however, require fewer fabrication steps than do semiconductors and do not require any high-temperature diffusions.

The basic geometry of a bubble device is shown in Fig. 1. The "bubbles" are cylindrical magnetic domains in a magnetic crystal such as a rare-earth garnet. The domains are stabilized by a bias field applied perpendicularly to the film plane.

For binary storage, the presence of a bubble codes a "1" while the absence of a bubble signifies a "0." The bubbles are stored in serial shift registers. Thin-film structures on the surface of the garnet films serve to define the register paths and also to write, read, and manipulate bubble streams.

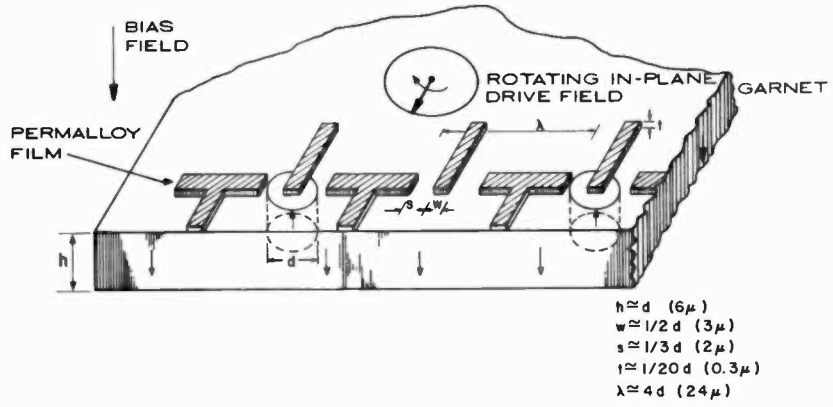

Fig. 1—Basic bubble geometry.

Bubbles are moved readily by gradients in the vertical field. These gradients are generated by thin permalloy films,[3] as shown in Fig. 1. The films are magnetized by an external rotating magnetic field that drives the gradients in synchronism. Field accessing is thus achieved. Conductor connections are needed only for reading, writing, and steering of information streams.

Chip Design

The 34-bit test chip shown in Fig. 2 was investigated to arrive at design rules, to develop fabrication technology, and to select optimum elements for mass memory chips. The chip design included distinct elements for evaluation of

(a) bubble propagation/storage,
(b) bubble generation,
(c) bubble replication/steering,
(d) bubble annihilation,
(e) magnetoresistive sensing.

These elements are connected to form a recirculating register.

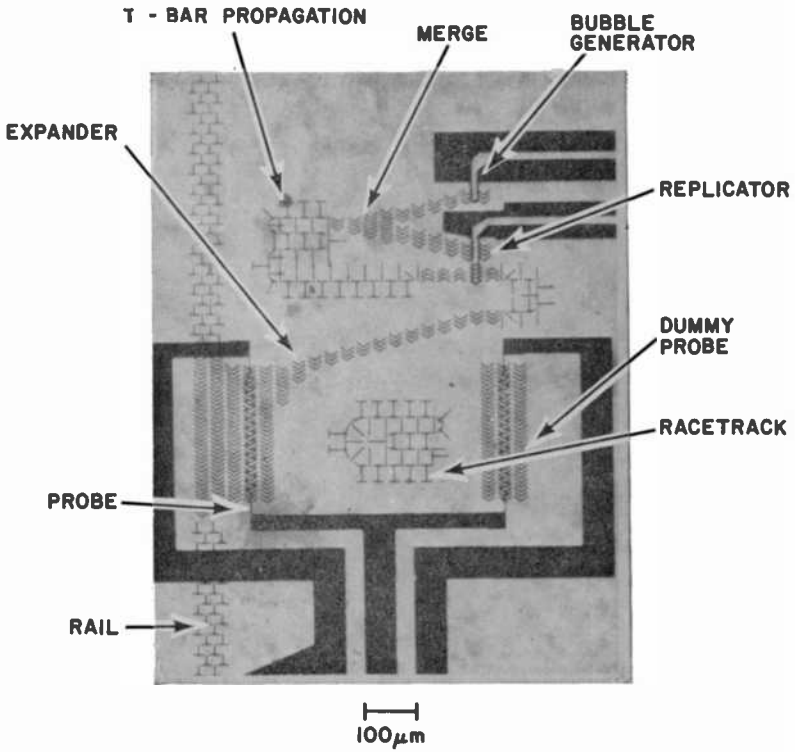

Fig. 2—Fabricated 34-bit register.

The chip was designed for garnet films with a nominal bubble diameter of 6.3 μm.

(a) Bubble Propagation

A coordinatograph is most efficient in generating orthogonal lines. This dictated the choice of T-bar[4] elements in the main body of the propagation pattern (see Fig. 2). In a large-capacity chip this portion would occupy the bulk of the chip area.

The design dimensions of the T–bars are: bar width = 3.8 μm, spacing between elements = 1.9 μm, periods = 30.4 μm and 32 μm. The propagation path is folded 3 times. Many more foldings would occur in a large array. The T and bar elements on neighboring legs of the folded array are merged. On the edges of the array the T's are still formed into I's to present a uniform field environment to a propagating bubble.

Eight different types of hairpin turns are incorporated into the design to permit evaluation of operating margins.

The bubble generator, the replicator, and the bubble sensor include chevron propagation structures.[5] A three-chevron design was adopted whose parameters are: bar width = 3.8 μm, chevron angle = 120°, period length = 30.4 μm, chevron-to-chevron spacing = 2.95 μm, inter-period spacing = 3.8 μm. No chevron hairpins are employed. Straight and slanted chevron lines are utilized. Three different types of transitions between chevrons and T-bars are used.

(b) Bubble Generation

In the nucleating generator, chosen for the test chip, a bubble is nucleated by a current pulse in a conductor loop. The generator conductor loop has a 6.3-μm line width with 6.3-μm spacing. The loop is ~30 μm deep and is connected by wide conductor film leads to avoid spurious nucleation of bubbles outside of the generator pattern. Two stages of chevrons are associated with the generator. To facilitate nucleation, the nucleating pulse should occur during that portion of the rotating drive field cycle when attractive poles appear on the chevron ends within the generator loop.

(c) Bubble Replication or Steering

A recirculating storage register requires a single logic gate to allow either the retention of a bubble stream (recirculation) or its destruction (erasure).

A replicator device serves the required function. In replicator operation, a bubble traveling on a chevron line is stretched (to encompass two chevron lines) by a current pulse in a conductor loop (see Fig. 2). As the drive field rotates, the bubble stretches even more. A current pulse in the conductor loop cuts the stretched bubble into two portions one of which travels to the sensor while the other recirculates in the storage loop. The stretching and the cutting pulses are of opposite polarities, favoring and opposing, respectively, the magnetization direction of the bubble. For our chip the replicator loop has the same width as the generator loop and is 80 μm long.

The recirculated bubbles returning to the storage loop are merged back into the main propagation path in a chevron merger.

(d) Bubble Annihilation

To erase information in a register one must annihilate bubbles. For

our design, the bubbles are first expanded in a chevron expander, then sensed by the sensor and finally discarded—pushed out of the pattern. A guard rail is provided to prevent discarded bubbles from returning to the storage area. Two types of guard rails are used, as shown in Fig. 2: a chevron rail (simply two additional columns of chevrons) and a T rail (4 columns of offset T's). The rail is so designed that the motion of any bubble caught in it is away from the pattern. In operation, the region outside the rail becomes filled with discarded bubbles, which annihilate each other.

(e) Magnetoresistive Sensing

Various ways of sensing bubbles have been proposed.[6] Practical detectors are Hall-effect probes, optical sensors,[7] and magnetoresistive probes.[8] The latter method was selected in the design of the register.

The resistance of a magnetoresistive probe changes by ~1 to 1.2% when magnetized. If a constant current flows through the probe, the change in resistance produces a voltage change across the probe terminals. Permalloy films, integrated with the rest of the pattern, are used as probes. Generally larger signals are obtained from very thin (< 1000 Å) probe films. However, for ease in fabrication, it is advantageous to use probes of the same thickness as the rest of the permalloy pattern (3000 Å). Such a probe gives a smaller signal but design can compensate for the signal loss.

The signal is directly proportional to the length of that part of probe permalloy whose magnetization is switched by the bubble. It is advantageous to use a long probe and to expand the bubble into a long stripe, positioned along the probe. A chevron zig-zag probe design was adopted for our register. The zig-zag probe maximizes the length of permalloy switched by the bubble. A sizable signal is obtained even with 3000 Å thick permalloy. An expansion factor of 31 was adopted. Near the ends of the probe the zig-zag pattern approaches a fishbone design to eliminate the possibility of stripe hang-ups at the probe ends.

Expansion by 31× is accomplished in 4 stages. Stripe-to-bubble compression is avoided entirely, since after sensing the stripes are discarded.

The magnetization in a magnetoresistive probe is switched not only by the bubbles but also by the rotating field and by neighboring permalloy structures. In addition, at higher frequencies, the drive field induces a voltage in the probe loop. To minimize these common-mode signals, differential sensing of two identical probes is utilized, as shown in Fig. 2.

(f) Chip Design Criteria

The prime criterion of our design was to create an arrangement with all the characteristics desirable in a large memory chip. This meant giving consideration to starting and stopping of data flow, recirculation and erasure of data, and immunity to failure modes. These considerations led to topological guidelines for design.

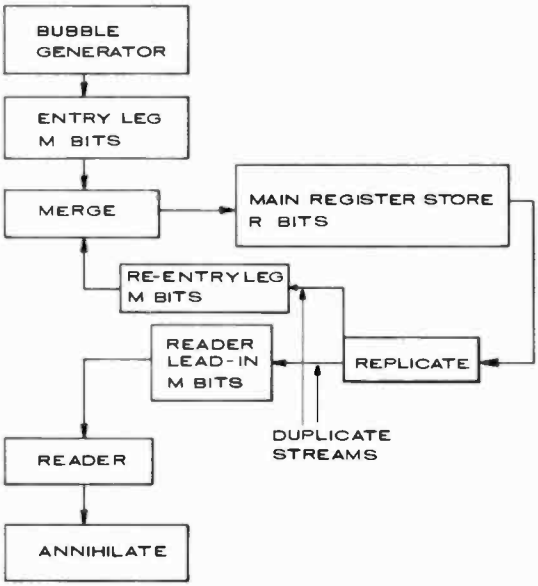

Fig. 3—Bubble memory functional diagram.

The location of the reader should allow read-out shortly after the track is filled. At the end of an initial read-in cycle, the first-loaded bit should be located one bit cell ahead of the sensing cell. In the recirculation mode, the first-loaded bit should be returned to this location at the end of each recirculation cycle. An erase function should make it possible to store new data without a separate erase cycle. The main information storage site should be a long register that has a first-in first-out characteristic. Information should be read nondestructively. There should be a re-entry path for the bubble flow. Information should be able to enter and leave the register loop via the merge and the replicator cell. An entry leg and a reader lead-in leg should be provided.

The manner in which the separate elements are integrated into the chip configuration is illustrated in Fig. 3. The register contains an

entry leg, and a reader lead-in leg with M bit cells in each. In the read-in mode, new data enter the chip via the entry leg. After $M + R$ shift fields (R = number of memory cells in the register), data entry stops and the first-entered bit is at the replicator cell. The advancement of the entered data is continued, but no new data are entered. The replicator provides data for the read and the re-entry legs. A total of $(M + R) + M$ shift fields will locate the first-entered bit at the merge cell and its twin at the read cell. At this point the main loop and the read leg are full and the entry leg is empty. Data are also ready for readout. Each subsequent series of $M + R$ shift pulses will play back the stored data. New data can be entered at any time. By inactivating the replicator during read-in, the old data will leave the register. Data in the re-entry leg do not merge with the incoming data since the data entry track has an M-bit blank buffer. This topography avoids the necessity for a separate erase cycle and permits continuous data read-in.

A failure of the replicator will cause the bubbles to flow to the reading station, leaving the memory still capable of sequential read-in/read-out cycles.

On-chip elements should be oriented to avoid loss of bubbles during start/stop cycles of the rotating magnetic field. The preferred bubble location at the power turn-off/turn-on cycle in a chevron pattern is at the end of one arm of the chevron V rather than in the middle. The generator, reader, merge, and replicator elements involve chevrons; thus they should be oriented so that the chevrons are facing in one direction or 180° from it. In the replicator, field timing should be such that the stretch-and-cut cycle is completed before the drive field is stopped.

The 34-bit chip design satisfies nearly all of the above criteria, except for the replicate-to-read-cell distance, which was made longer because of the overriding concern for keeping the active chip area small. A small "racetrack" structure located between the probes was incorporated to evaluate hairpin turns.

Registration marks limit layer-to-layer errors to 0.8 μm. In the worst case, a 1.6-μm alignment error over 3 layers is still acceptable.

Device Fabrication

(a) Garnet and Substrate

The magnetic garnet films were grown by Liquid Phase Epitaxy (LPE) on Gadolinium Gallium Garnet (GGG) substrates. The GGG wafers are approximately 20 mils thick and $\frac{7}{8}$ or $1\frac{1}{4}$ inches in diameter. The

garnet films are typically 6 to 7 μm thick. The film thickness is uniform to within one fringe of sodium light. Approximately 9 chips of uniform film thickness and with dimensions of 5×5 mm can be diced out of a typical wafer using a diamond wheel or laser-beam scribing.

Typical parameters for the garnet films are given in Table 1. The films exhibit a low defect density, typically less than 1 defect per chip from the central portion of the wafer.

(b) Layers on the Garnet Film

The structures fabricated on top of the garnet film must be spaced at predetermined distances from the bubble material. The permalloy films should be 1 μm from the garnet to prevent bubble hang-ups. Nucleator and replicator loops should be at a smaller distance to minimize current pulse requirements, but not directly over the garnet film, since stresses at the edge of the conductor film can interfere with bubble propogation.[9]

Table 1—Typical Garnet Parameters

Nominal Composition: $(Y,Eu)_3(Fe,Ga)_5O_{12}$
Thickness: 6-7 μm
Saturation Flux Density ($4\pi M_s$): 120-150 gauss
Mid-range Bubble Diameter: 6-7 μm
Mid-range Bias Field: 50-65 Oe
Coercivity: ~0.3 Oe
Collapse Field: 60-70 Oe
Mobility: ~400 cm/sec/Oe

These considerations led to the structure shown in Fig. 4. The garnet film is first coated with a 3000 Å SiO_2 layer. The conductor is deposited next, 3000 to 10000 Å thick. The conductor layer is etched and a second SiO_2 layer is deposited, 7000 Å thick. Windows are opened in the SiO_2 for contacts. Permalloy, 3000 Å thick, is deposited and etched next. If necessary, to prevent oxidation of the permalloy, a protective layer (SiO_2 or an organic coating) is deposited over the chip (omitted in Fig. 4).

Thus 4 deposition and 3 masking-etching operations are necessary to produce this pattern, with another deposition and etching operation optional.

(c) Mask Fabrication

The RCA design automation program PLOTS was used in generation of the master artwork. This approach results in the creation of a

standard library of common bubble element designs that can be used in the future. Debugging of the program was done with a combination of available artwork display systems: coarse error detection through use of CRT displays and more accurate checks using graphical plotters.

The final program was used to create master artwork glass plates on a coordinatograph. The artwork was optically reduced to the desired bubble size. Chrome masks were used.

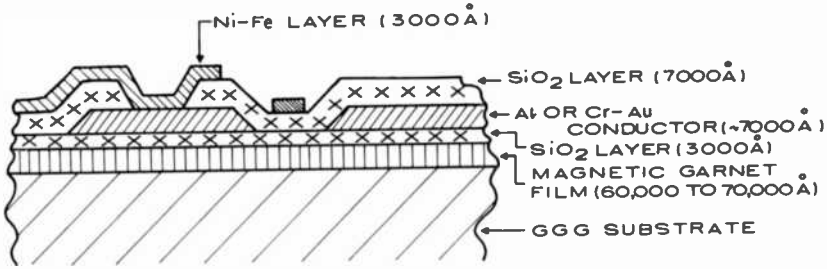

Fig. 4—Layers on garnet chip.

(d) Device Fabrication

Two SiO_2 deposition techniques are used: rf sputtering and silane chemical vapor deposition. Studies of pinholes in the SiO_2 show the sputtered layers to be superior to undensified silane-deposited layers. Negative photoresist is used to open contact windows in the SiO_2. A special technique is utilized to produce gently sloping edges in the SiO_2 windows for reliable contact between the permalloy and the probe leads.

Aluminum or chrome–gold conductors are fabricated by vacuum deposition. Techniques for gently sloping conductor edges for both Al and Cr-Au were developed to permit permalloy elements to climb over these edges without breaks.

Cr-Au is preferred to Al, since permalloy etchants attack Al readily, but do not attack Au. Pinholes in the SiO_2 layer permit the permalloy is either evaporated from an rf-heated alumina crucible or

Zero magnetostriction (80:20 Ni-Fe) permalloy is used. The permalloy is either evaporated from an rf-heated alumina crucible or sputtered. The films exhibit coercivities of less than 3 Oe and some anisotropy. The magnetic properties of the evaporated films are easier to control than those of sputtered films.

Chips are mounted on carrier boards designed for insertion into

testing jigs. On-chip conductors are ultrasonically bonded to the carrier board.

Device Testing

(a) Test Equipment

The fabricated chips underwent extensive testing. Complete margin and other data were taken at low propagation speeds (up to 100 Hz). Devices were also operated successfully at higher speeds (up to ~8 kHz).

The test equipment consists of a polarizing microscope, a single pair of coils for supplying the bias field, two orthogonal coil pairs driven in quadrature to provide the rotating field, and associated electronic circuitry.

All functions for the drive circuitry are digitally controlled by a variable-rate clock. On-chip functions are driven from a common 12-phase decoder integrally phase-locked to the rotating drive field. Nucleate and replicate pulses can be easily varied in phase and duration with respect to the rotating field cycle. Sensing is accomplished by a pair of ac-coupled 26-dB preamplifiers that provide current sources for the probes, or by a dc-coupled single-ended preamplifier.

(b) Bubble Propagation

Bubbles were propagated completely from generator to probe and around the small racetrack in all of the devices tested. None of the circuits had garnet defects to impede bubble motion. Low-frequency operating margins of propagation were determined for 17 distinct elements on the chip: 2 types of T-bars, 2 types of chevron propagation line, 8 types of hairpins, the merger, the expander, and 3 types of transitions between chevrons and T-bars. Figs. 5 and 6 show margins for representative elements. Fig. 7 gives the combined margin for all of the features on the chip. It was concluded that:

1. The bias field margins for individual features are all reasonably wide. Typically, at 35 Oe drive field they are ±10%. The narrowest margin is exhibited by the slanted chevron line, but even that is ±6% at 35 Oe drive.

2. The combined margin for all the features on the chip is considerably narrower: ±4% at 35 Oe drive, due to the fact that some devices operate better at higher bias field, some at lower. The failure mechanisms are different for different devices. For example, in a T-bar line at high bias field, bubbles tend to collapse. In a slanted chevron line at a higher bias the stretched-out bubbles (stripes) tend to escape out of the line.

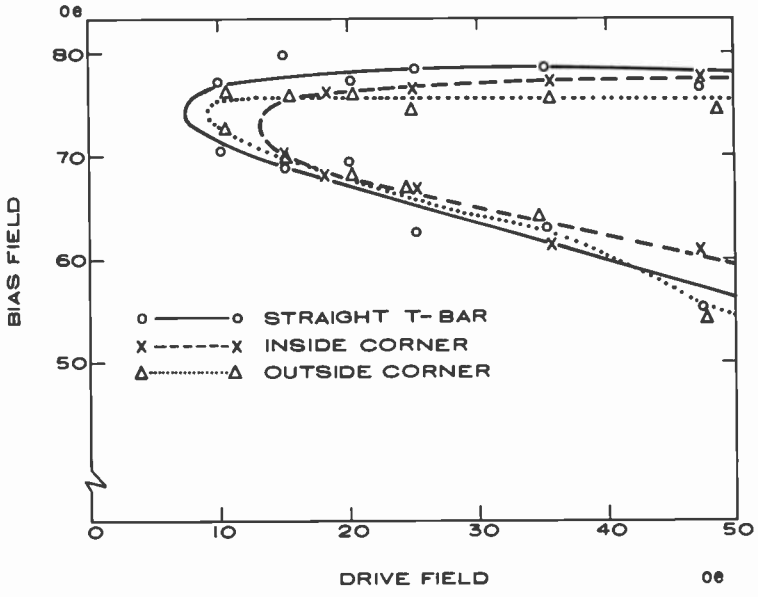

Fig. 5—Typical margins of various T-bar structures.

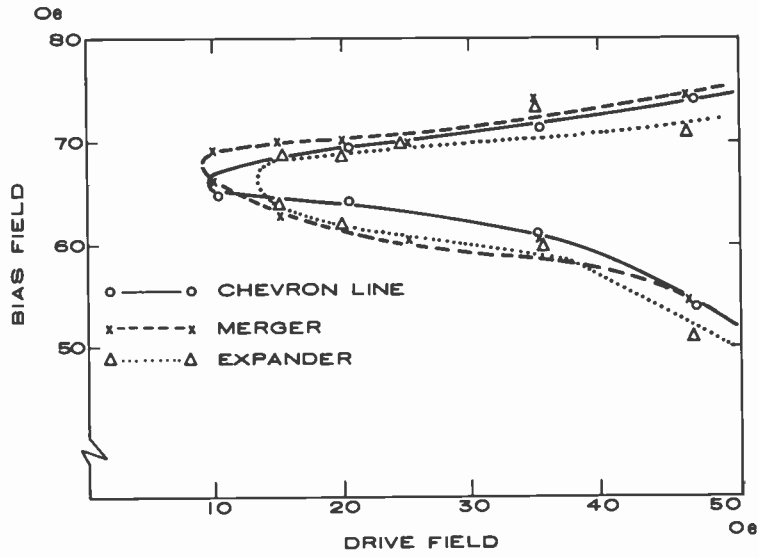

Fig. 6—Typical margins of various chevron structures.

3. The pattern contains extra features: different types of corners, transitions, etc. If one selects a minimal necessary set of features for maximum margin overlap, the combined margin widens to ±6% at 35 Oe drive (see the outer margin in Fig. 7). The slanted chevron line should be avoided.

4. The margins of the active elements (generator, replicator, probe) are the same as those of the associated chevron lines. Conductor loops, either Au or Al, did not affect the bubble motion.

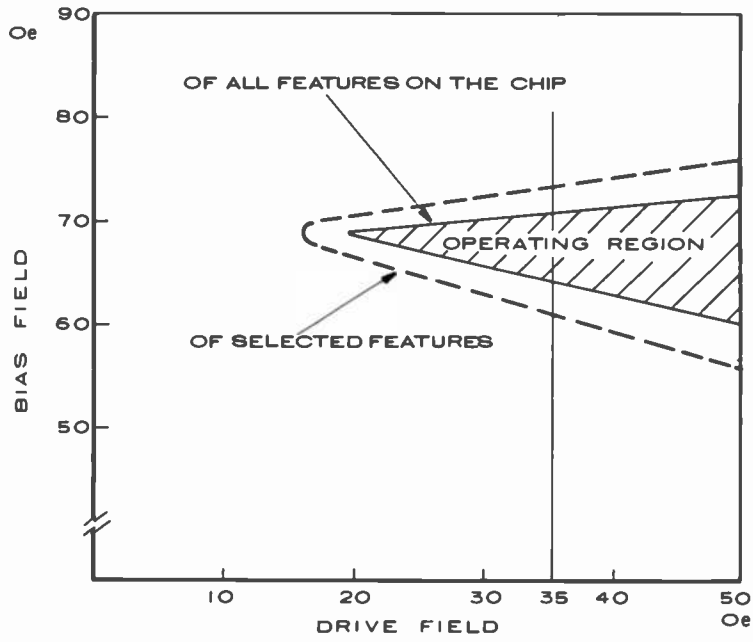

Fig. 7—Combined margins of operation of (1) all elements on the chip (inside margin) and (2) a minimum set of elements necessary for a complete memory register (outside margin).

(c) Bubble Generator

The generator nucleates reliably with current pulses of at least 225 mA at 100 nsec duration. Bubbles can be reliably nucleated during more than 180° of the rotating field cycle. Nucleation is largely independent of bias conditions. Nucleation was observed to occur even at high bias values, when the nucleated bubbles collapsed before leaving the generator.

(d) Bubble Replicator

Fig. 8 illustrates the replicator action. The minimum pulse necessary for stretching the bubble into a stripe stradling the 2 chevron lines is 70 mA, 600 nsec. Higher amplitude pulses can be shorter, since they produce faster wall motion. The cutting pulse should be at least 100 mA and 100 nsec. The timing of the replicate pulses is more critical than the timing of the generator pulses, but a latitude of ~90° of the drive cycle is allowable.

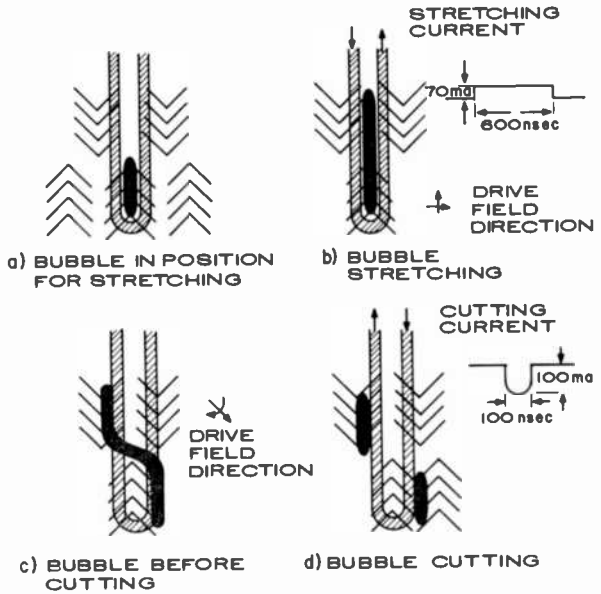

Fig. 8—Operation of the replicator.

(e) The Magnetoresistive Probe

The probe expander operates with reasonable margins (see Fig. 6). No problems were encountered with discarded bubbles outside the guard rail. The guard rail operates faultlessly over the whole range of bias and drive fields.

The large pads of the probe contacts present some difficulties. At low bias fields, expanded bubbles tend to hang up on the big permalloy pads. Occasionally a stray bubble gets captured under one of the pads. At certain field values this pad–bubble combination acts as a spontaneous bubble generator.[3] Both of these difficulties, however, occur

outside the combined margin area of Fig. 7. The difficulties can be avoided by making the pads smaller and circular in shape, and by placing them further away from the probes.

The probe resistance, including leads and contacts, ranged from 200 to 250 ohms. Matching between the 2 probe resistances on a chip is usually within 10%. The matching is important, since it determines the common-mode rejection ratio.

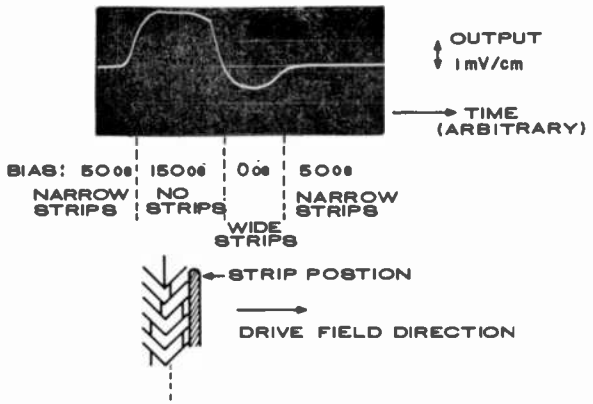

Fig. 9—Bubble-collapse experiment (at 10 mA probe current).

Two basic tests were performed to study the probes. In the first experiment (see Fig. 9), a stripe is positioned next to the probe, using the drive field, in the presence of mid-range bias field. With the drive field on, the bias field is increased gradually until the stripe collapses. The output of the probe is monitored, using a dc amplifier and a slow scan on the oscilloscope as in Fig. 9. The bias field is then reduced so that the chip is filled up again with stripes, one of which gets positioned next to the probe by the constant drive field. In this experiment the signal is totally due to the stripe since the vertical bias field does not produce any output and the drive field is constant.

The results of this experiment are shown as a function of probe current in Fig. 10. The output is $\sim$ 200 μV/mA of probe current for the 31-chevron probe, or $\sim$ 6 μV/chevron/mA. Up to 10 mA of probe current (giving a signal of 2 mV) can be used. At higher currents there is some interference with bubble motion and some probe heating, leading to decreased output as shown by the drooping of the curve in Fig. 10. The probe does not burn out, even at 20 mA.

At 10 mA, the probe current density is $\sim 8 \times 10^5$ A/cm^2. This

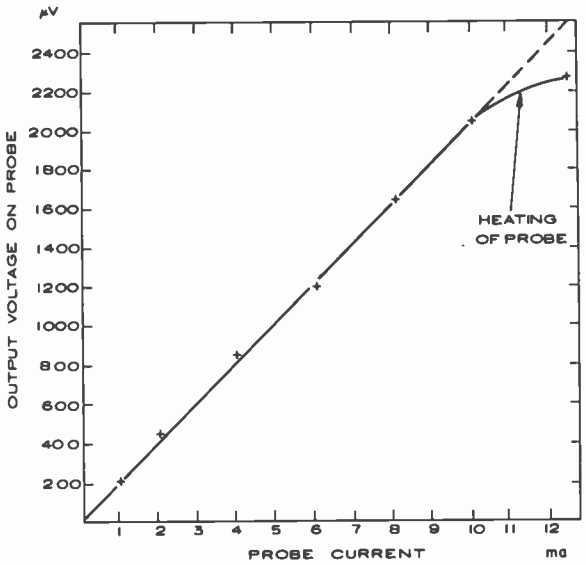

Fig. 10—Output voltage versus probe current.

density would in time lead to problems of migration and oxidation.[10] It is recommended that the maximum probe current not exceed 5 mA. Thus, for a 2-mV signal, the probe should contain at least 70 chevrons.

The observed signal voltage constitutes only about 0.1% of the voltage drop across the probe. Since the $\Delta R/R$ of the permalloy film material is 1% to 1.2%, it is evident that only about 10% switching of the probe magnetization contributes to the sense signal.

In normal operation, the voltage developed across the probe terminals contains common-mode noise components. Fig. 11 shows typical single-ended outputs, with and without a bubble. The common-mode noise at 28 Oe drive is about twice the signal due to the bubble. The

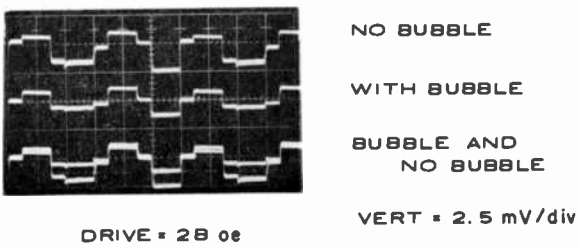

Fig. 11—Single-ended output at probe terminals. Probe current is 5mA; horizontal calibration is 2 msec/div.

bubble signal at this drive field is ~ 200 μV/mA of probe current, comparable to signals obtained in the static experiment. At higher drives the common-mode noise increases, while the bubble signal decreases because the probe magnetization is partially clamped by the drive field. At 35 Oe drive the signal is only about ~ 160 μV/mA of probe current.

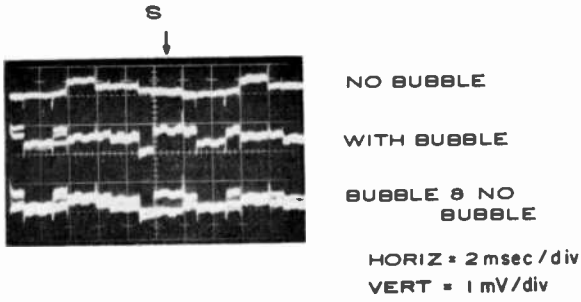

Fig. 12—Differential output of probe and dummy at probe terminals. Probe current is 5 mA; drive field is 35 Oe. *S* indicates suggested timing of strobing pulse.

Fig. 12 shows the differential output of a probe pair at 35 Oe drive. The common-mode noise is partially suppressed by differential sensing and is comparable to the signal, considerably below the 1:4 signal-to-noise ratio obtained at this drive level with single-ended output. No attempt was made in Fig. 12 to minimize the common-mode noise by adjusting the two probe currents. Such adjustments may improve the signal to common-mode noise ratio to about 10:1 in a well-matched probe pair. From Fig. 12 it is evident that strobing of the signals will be necessary. The optimum timing of the strobing pulse is indicated.

(f) Discussion

Testing of the 34-bit chip proved that reliable operation of a bubble memory device is possible. The tested chips displayed reasonable margins, required low generate and replicate pulse amplitudes, and gave acceptable sense signals. The data presented are mostly from low-frequency operation. However, we were able to operate some of the devices at 8 kHz.

The choice of drive field amplitude must be a compromise. At high drive fields, the operating margins are wide, but the probe signal

level decreases. It is suggested that large expansion-ratio probes (> 100 chevrons) be used for wide margin operation.

The experience gained makes it possible to design a memory chip with a large number of bits. Table 2 summarizes our experience with fabrication of the test chips. These are not true yield figures, since fabrication steps were being developed and improved as we went along. The table includes all the chips processed, even the results of unsucessfull experiments.

Table 2—Results of 34-bit Chip Fabrication

Wafers: $(Eu,Y)_3(Fe,Ga)_5O_{12}$
- ⅞ and 1⅛ inch diameter
- Total number diced for this application: 9
  - (7 perfect, 2 for training purposes)

Chips: 5 × 5 mm
- Total number of acceptable chips: 80
- Number of chips used in fabrication: 56

Memory Registers:
- Number of chips that went through all of the fabrication steps: 45
- Number of chips accepted and mounted on carrier boards: 22
  - Of these:
  - — 6 chips had both probes continuous
  - — 5 chips had 1 probe continuous
  - — 11 chips had no probes continuous, but were otherwise perfect
- Number of chips Tested: 18
  - Of these:
  - — 6 chips had everything working
  - — 12 chips had everything but the probes working

Conclusions

A simple bubble memory test chip has been designed and successfully operated. It is capable of performing all the elementary functions of storage, data entry, readout, replication, and erasure. We were able to fabricate with reasonable yield the required garnet materials and the required patterns.

Large garnet film chips are now available both at RCA and from outside vendors so that the capacity of a register is no longer limited by chip size. State-of-the-art storage density is 10^6 bits/sq. inch. With advanced techniques it can reach or exceed 10^8 bits/sq. inch. The present chip capacity is $\sim 5 \times 10^4$ bits, where artwork reduction optics and uniform large area etching are the limiting factors. Serial bit rates of $\sim 10^5$ bps have been achieved reliably with ion-implanted garnet films and 10^7 bps has been proposed as the eventual rate. Non-destructive, non-volatile information storage is possible. Temperature

variations do affect physical characteristics of bubble materials but the safe operating range is compatible with military standards.

The ultimate viability of the bubble memory concept is still to be established and will in part be determined by progress achieved with competing approaches.

Acknowledgments

The authors wish to acknowledge the help received from A. Akselrad, I. Gordon, C. Horak, R. Noack, and T. Ward at RCA Laboratories and J. Griffin at RCA, Camden. The authors also wish to acknowledge the contributions of J. Banfield, F. Cestone, and R. Epiphano at RCA Somerville.

References:

[1] A. Bobeck, R. Fisher, A. Perneski, J. Remeica, and L. VanUitert, "Application of Orthoferrites to Domain Wall Devices," **IEEE Trans. on Mag.**, Vol. MAG-5, No. 3, p. 544, Sept. 1969.

[2] B. Bobeck and H. Scovil, "Magnetic Bubbles," **Scientific American**, p. 78, June 1971.

[3] A. Akselrad, L. Onyshkevych, R. Shahbender, and C. Wentworth, "Magnetic Bubble Technology," RCA Reprint RE 18-4-4 (1973).

[4] A. J. Perneski, "Propagation of Cylindrical Magnetic Domains in Orthoferrities," **IEEE Trans. on Mag.**, Vol. MAG-5, No. 3, p. 554, Sept. 1969.

[5] A. Bobeck, R. Fisher, and J. Smith, "An Overview of Magnetic Bubble Domains—Material-Device Interface," **AIP Conf. Proc.**, No. 5, **Magnetism and Magnetic Materials**, p. 45 (1971).

[6] W. Strauss, "Detection of Cylindrical Magnetic Domains," **J. Appl. Phys.**, Vol. 42, No. 4, p. 1251, Mar. 15, 1971.

[7] R. Shahbender and J. Druguet, "Lensless Optical Detection of Bubble Domains," **RCA Rev.**, Vol. 34, No. 3, p. 385, Sept. 1973.

[8] G. Almasi, K. Keefe, Y. Lin, and D. Thompson, "Magnetoresistive Detector for Bubble Domains," **J. Appl. Phys.**, Vol. 42, No. 4, p. 1268, Mar. 15, 1971.

[9] J. Dishman, R. Pierce. and B. Roman, "Effects of Metallization Stress in Bubble Devices," presented at 1973 INTERMAG, April 24-27, Wash., D.C.

[10] G. Moore, Jr., P. Turner, and K. Tai, "Current Density Limitations in Permalloy Magnetic Detectors," **AIP Conf. Proc.**, No. 10, **Magnetism and Magnetic Materials**, p. 217 (1972).

Properties of Avalanche Photodiodes

P. P. Webb, R. J. McIntyre, and J. Conradi
RCA Limited, Ste. Anne de Bellevue, Quebec

Abstract—The basic properties of avalanche photodiodes are reviewed and the conditions under which they can be used to best advantage are discussed. Expressions are presented for calculating the avalanche gain, signal-to-noise ratio, detector excess noise factor, effective noise factor under conditions of mixed injection, diode linearity and saturation, noise equivalent power, quantum efficiency, impulse time response, and frequency response. Several commercially available avalanche photodiode structures are compared, and their virtues and disadvantages are discussed. The properties of a reach-through avalanche photodiode developed in this laboratory are discussed in detail, and experimental results are presented for single-element avalanche diodes with sensitive areas up to 20 mm^2, and quadrant avalanche diodes with 5 mm^2 sensitive areas. Finally, an equivalent circuit for the reach-through avalanche diode is derived.

1. Introduction

Within the past decade, solid-state photodiodes have come into prominence as small, rugged, fast, and convenient detectors in the visible and near infrared. Because they can be made with quantum efficien-

cies close to 100%, they come within a few percent of achieving the performance of ideal detectors in any background-limited application, i.e., applications in which the major source of noise is in fluctuations in the light incident on the detector. Since the majority of every-day commercial applications (e.g., card-readers, light activated relays, and lightmeters, optical pick-offs) and many military applications are of the background-limited variety, simple p-n or p-i-n junction photodiodes can be the ideal solution in that they provide the best signal-to-noise ratio possible. A drawback is that, unlike photomultipliers or photoconductive detectors, such as CdS or PbS, they provide no internal gain and in most cases require use of an amplifier to provide a large enough signal current.

Not all applications, however, are background limited (see Fig. 1). The laser, with its narrow spectral bandwidth, allows the use of narrow-band optical filters that exclude much of the normal background radiation, and high-speed optical modulation techniques allow signal bandwidths of 1 GHz or more to be carried by the laser. The limiting source of noise, then, can be either the dark current in the detector, the noise in the preamplifier, or the quantum noise in the signal carrier. If the detector dark current is the limiting factor, improvement can be obtained only by reducing the dark current, either by cooling the detector or switching to a different detector type (such as a photodiode made from a material having a wider bandgap or a photomultiplier). If amplifier noise is the limiting noise source, it is desirable to have an internal gain mechanism in the detector that multiplies, as noiselessly as possible, both the detector signal and the detector noise until the latter is greater than the amplifier noise.

By way of illustration, we consider the case of a narrow-band (less than one octave) detection system designed to detect a signal modulated at a center frequency ω. For this situation, the signal-to-noise ratio of a photodiode or an avalanche photodiode detection circuit can be written[1]

$$\frac{S}{N}=\left(\frac{i_s}{i_n}\right)^2=\frac{(P_o m R_o M)^2/2}{2q[I_{ds}+(P_o R_o F_s+I_{db}F_d)M^2]B+i_{na}^2} \qquad [1]$$

where P_o is the average value of the intensity of light incident on the detector,

m is the modulation depth (such that $P_o m$ is the amplitude of the fundamental component of the modulated signal),

R_o is the unity-gain responsivity,

M is the gain ($M = 1$ in the case of a nonmultiplying photodiode),

q is the electronic charge,

I_{ds} is that component of the dark current (usually the surface component) that is not multiplied,

I_{db} is that component of the dark current (usually the bulk-generated dark current) that undergoes multiplication,

B is the noise bandwidth,

i_{na}^2 is the equivalent mean square noise current of the amplifier and biasing circuit,

F_d is the detector effective excess noise factor appropriate to the multiplication of the dark current I_{db}, and

F_s is the detector effective excess noise factor appropriate to the multiplication of the photocurrent (we assume that the radiation due to background and signal are at the same wavelength).

In some avalanche diode structures the effective excess noise factors above may be different, and F_s may be wavelength dependent, as they depend on the ratio of the electron and hole currents injected into the multiplying region (see Secs. 2 and 3 for further discussion).

As we shall find later, the detector noise factor F is unity for a nonmultiplying photodiode and is a monotonically increasing function of gain for multiplying photodiodes. Since the factor M^2 appears in both the numerator and denominator of Eq. [1], an increase in gain will increase the signal-to-noise ratio only if the term in which M^2F appears is not already the dominant term in the denominator.

Fig. 1 shows the relative amplitudes of the various contributions to the noise current, normalized to unity bandwidth, in a typical nonmultiplying detector circuit as a function of the bandwidth of that circuit. The shaded area labeled "amplified-noise" denotes the region in which the noise current, referred to the input, of "typical" low-noise preamplifiers might fall. It is not meant to be absolute, and with improved circuit design and devices, the lower edge of this region can be expected to move down, particularly for wide bandwidths. The points have no significance other than that they are experimental values for specific preamplifiers built in this laboratory. The preamplifier noise includes the noise of the load resistor. To achieve low noise, this resistor must be large. The noise contribution from the load resistor itself is also shown in Fig. 1.

The dashed lines in Fig. 1 show the noise contribution of the incident power P_o for two fictitious situations in which it is assumed that the only noise is that from the signal (i.e. the detectors are as-

sumed to be quantum-noise limited). In these cases, Eq. [1] would reduce to

$$\frac{S}{N} = \frac{P_o m^2 R_o}{4qB} \qquad [1(a)]$$

(for $M = F = 1$) so that the noise current spectral density would be given by

$$\left(\frac{i_n^2}{B}\right)^{1/2} = (2qP_oR_o)^{1/2} = \left(\frac{8q^2B}{m^2}\frac{S}{N}\right)^{1/2}. \qquad [2]$$

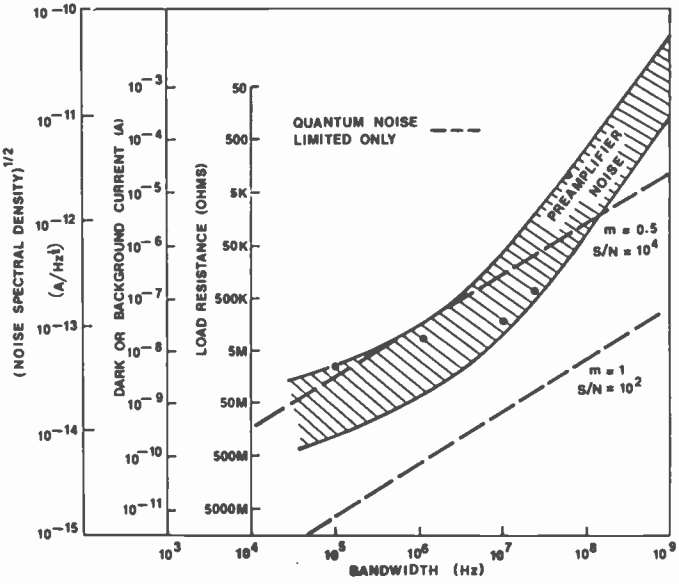

Fig. 1—Noise sources encountered in optical detection systems.

The upper dashed curve ($m = 0.5$, $S/N = 10^4$) might represent typical operating conditions for a high quality video link in an amplitude modulated laser-diode fiber-optic system. It is obvious that for this application the noise from the signal itself can be as large as, or greater than, the noise of the following preamplifier, so that nothing is to be gained by using a multiplying photodiode. For applications requiring a smaller value of S/N, such as a fiber-optic system carrying digital information, the quantum noise is not as high, and the use of a multiplying detector would present an advantage.

It can be seen from Eq. [1] and Fig. 1 that a multiplying detector can improve the system performance only when the dark and background currents are sufficiently low that the noise from all other sources is less than that of the preamplifier, and that the required gain is only that which will raise this noise above that of the preamplifier. This required gain can be quite low (of the order of 10 to 20) except in very wideband systems, where it is higher only if the modulation system is such that the noise-in-signal is low. An example of such a system is a pulse-code-modulation (PCM) communications system in which the signal pulses are much shorter than the interval between them. The noise analysis of this type of system is discussed more completely later in this paper.

One advantage of avalanche photodiodes that is not often appreciated is that the current I_{db} is usually more than two orders of magnitude less than I_{ds}, typical values being 10^{-10} A/mm^2 and $\sim 3 \times 10^{-8}$ A/mm of circumference, respectively. Since only I_{db} is multiplied, an avalanche diode with a gain of 10 can have less than twice the noise current, but 10 times the signal current, of a p-i-n diode of the same area, provided $P_o R_o$ is less than I_{db}.

It is clear from this discussion that very high internal gains, such as those available in photomultipliers, may be convenient in that they eliminate the need for a low noise preamplifier, but they are by no means essential to obtaining the best possible performance. In addition, avalanche photodiodes may be better suited for certain applications by virtue of their ruggedness, size, speed, and greater quantum efficiency in the near infrared; this in spite of being limited to gains of 200 or less (depending on size) and being rather noisy amplifiers, particularly at high gains. Two important applications in which these conditions occur are laser ranging and optical communications at 0.8-0.9 μm ($Ga_xAl_{1-x}As$ laser or light-emitting diodes) or at 1.06 μm (neodymium-doped YAG or glass lasers).

In the remainder of this paper, we first review those basic avalanche mechanisms that are pertinent to the intelligent use of avalanche photodiodes. Section 3 then compares the three avalanche photodiode structures that are commercially available today, and Section 4 describes in some detail the properties of the reach-through avalanche photodiode structure developed in these laboratories.

2. Basic Properties of Avalanche Multiplication

To use avalanche photodiodes to best advantage, it is important that the user have a working knowledge of their operating mechanisms.

The basic physical mechanism upon which avalanche gain depends is that of impact ionization. If the electric field is sufficiently high, an electron or a hole can collide with a bound (valence) electron with sufficient energy to ionize it, thereby creating an extra electron and hole. These additional carriers, in turn, can gain enough energy from the field to cause further impact ionization, until an avalanche of carriers has been created. Below the diode breakdown voltage the total number created is finite; above, it can approach infinity.

2.1 Ionization Rate

The probability that an electron or hole will have an ionizing collision is a strong function of the electric field, and can increase by several orders of magnitude as the electric field increases by, say, 50%. Normally, the ionization probabilities are assumed to be functions of electric field only. In a practical avalanche photodiode, where the mean free path for scattering collisions is much shorter than both the mean free path for ionizing collisions and the distance over which the electric field and ionization rates change appreciably, the approximation that the ionization probabilities are a function of electric field only is not a bad one. Since the electric field in the depletion layer is a function of position and the ionization coefficients are strong functions of the electric field, the ionization coefficients will be very strong functions of position in the depletion layer, and are large enough to merit consideration only where the electric field is highest. The *probabilities* that a given electron or hole will have an ionizing collision within a distance dx are αdx and βdx, respectively, where α and β are the *ionization coefficients*. (These coefficients are also referred to in the literature as α_e and α_h, or α_n and α_p; we use α and β here for simplicity.)

2.2 Gain or Multiplication

The ideal avalanche photodiode would be one in which only one type of carrier is capable of having ionizing collisions. If, for example, these were electrons, one would try to absorb all the light on the p-side of the junction. In traversing the high-field region, the electron current J_n would then vary with position according to the equation

$$-\frac{dJ_n}{dx} = \alpha J_n, \qquad [3]$$

which is easily integrated to give

$$J_n(x) = J_n(x_2) \exp\left[\int_{x}^{x_2} \alpha dx\right]. \qquad [4]$$

Thus if x_1 and x_2 represent the extremities of the high-field region (see Fig. 2), the electron multiplication M_e, which is the ratio of the

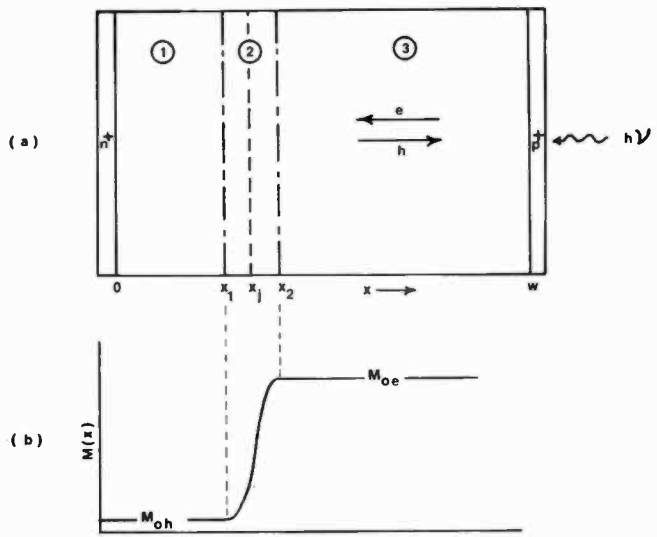

Fig. 2—Schematic of multiplying region.

multiplied electron current $J_n(x_1)$ to the injected electron current $J_n(x_2)$, would be given by

$$M_e = e^{\delta}, \quad \beta \ll \alpha, \qquad [5]$$

where

$$\delta = \int_{x_1}^{x_2} \alpha dx. \qquad [6]$$

Note that although M_e increases exponentially with δ, it is always finite so long as $\beta = 0$. Thus, such a diode would never go into avalanche 'breakdown'.

Unfortunately, the ideal situation of single-carrier multiplication is seldom if ever the case in practical semiconductor materials. In most materials, both electrons and holes can have impact ionizations, in which case Eq. [3] must be modified to give[2]

$$\frac{dJ_n}{dx} = -\alpha J_n - \beta J_p - g(x) = -\frac{dJ_p}{dx}. \qquad [7]$$

Here, we have included not only the hole ionization current, but generalized to include the case where optical generation $g(x)$ also occurs in the high-field region.

The solution to this equation can be shown to be given by

$$\overline{M} = \frac{\int_0^w g(x)M(x)dx}{\int_0^w g(x)dx}, \qquad [8]$$

where $\overline{M}$ is the average multiplication for all carriers generated in the diode, and $M(x)$ is the multiplication that a hole–electron pair generated at x will undergo. This is given by[2,3]

$$M(x) = \frac{G(x)}{1 - \int_{x_1}^{x_2} \alpha G(x)dx}, \qquad [9]$$

where

$$G(x) = \exp\left[-\int_x^{x_2} (\alpha - \beta)dx'\right]. \qquad [10]$$

$M(x)$ is sketched in Fig. 2. It is to be noted that $M(x)$ is constant everywhere except in the high-field region, having the value M_h on the n-side of the junction and M_e on the p-side, with the transition region being very narrow. It is usually sufficient to approximate Eq. [8] by

$$\overline{M} = \frac{I_{po}M_h + I_{no}M_e}{I_{po} + I_{no}}, \qquad [11]$$

where $I_{po} = \int_o^{x_j} g(x)dx$ and $I_{no} = \int_{x_j}^{w} g(x)dx$ are the 'primary' or 'injected' hole and electron currents. M_h and M_e are related by $M_h = G(x_1)M_e$.

Eq. [9] is, in general, difficult to solve except in the case of a p-i-n avalanche diode in which α and β are constant everywhere, and as far as we are aware, no such device has ever been made. Eq. [9] can be put in a more useful form, however, by writing

$$M(x) = \frac{G(x)(1-k_1)}{G(x_1) - k_1}, \quad G(x_1) = \exp\left[-(1-k_o)\delta\right] \qquad [12]$$

where

$$k_o = \int_{x_1}^{x_2} \beta dx \Big/ \int_{x_1}^{x_2} \alpha dx$$

and

$$k_1 = \int_{x_1}^{x_2} \beta G(x)dx \Big/ \int_{x_1}^{x_2} \alpha G(x)dx$$

$$= \int_{x_1}^{x_2} \beta M(x)dx \Big/ \int_{x_1}^{x_2} \alpha M(x)dx \qquad [13]$$

Thus k_o is an average and k_1 is a weighted average of the ratio of the hole and electron ionization rates. As it turns out, k_o and k_1 do not normally vary very much with gain, and can, to a first approximation, be considered constant and equal. This is very convenient, in that it allows one to study the properties of the avalanche diode in terms of the ratio of the ionization coefficients. The electron multiplication is

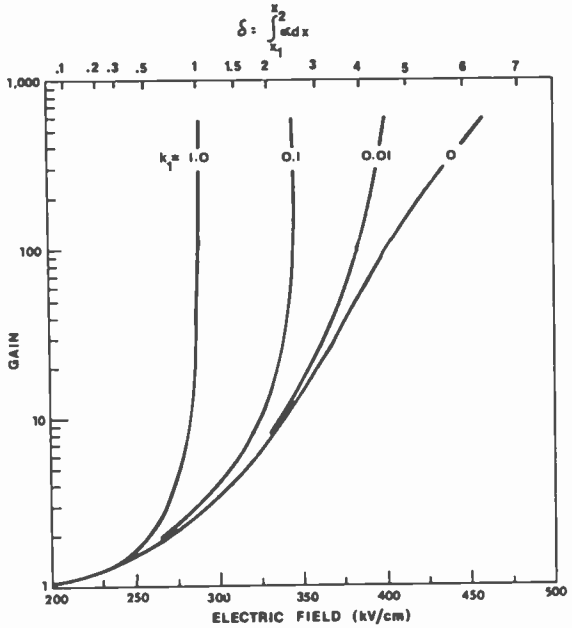

Fig. 3—Electron multiplication as a function of electric field and δ, with ionization ratio k_1 as a parameter, in a 1 μm wide p-i-n diode.

shown as a function of δ and k_1 in Fig. 3. (Also shown are the fields required to give corresponding values of δ in a silicon p-i-n diode 1 μm wide.) It is seen that for any value of k_1 other than zero, the multiplication goes to infinity at some finite electric field or voltage, and that the slope of the M versus E curve is a strong function of k_1. This slope is important in that it determines how uniform the doping level must be in the depletion layer so that a given multiplication uniformity can be obtained. At a gain of 100, for example, a 0.5% variation in doping level (and therefore in electric field) would result in a 20% variation in gain if $k = 0.01$ and a completely nonusable 320% variation in gain if $k = 1$! This curve, more than anything else, demonstrates the severe practical problems in trying to make

avalanche photodiodes out of materials in which the ionization ratio (k_1) is not small. As we shall see later, there are also other reasons.

2.3 Excess Noise Factor

The expressions for $M(x)$ given in Eqs. [9] and [12] give the *average* multiplication that a hole–electron pair generated at x will undergo. However, not every pair generated at x undergoes the same multiplication. In fact, there is quite a wide probability distribution of possible gains any particular pair might experience, so that when the average gain is M, the *mean square* gain is somewhat greater than M^2. Since the noise depends on the mean square gain, the avalanche device can be relatively noisy. If the noise spectral density in the primary current is $2qI_o$, it is convenient to write the noise spectral density in the multiplied current as $2qI_oM^2F$, where $F = <M^2>/<M>^2$. (Here the symbols $< >$ imply an ensemble average.) Thus, F is the ratio of the actual noise to that which would exist if the multiplication process were noiseless (i.e., all generated pairs being multiplied by exactly M). F is usually referred to as the *excess noise factor*.

Expressions for the excess noise factor have been derived for both injected electrons and holes.[24] They are, respectively,

$$F_e = \frac{k_2 - k_1^2}{1 - k_2} M_e + 2\left[1 - \frac{k_1(1-k_1)}{1-k_2}\right] - \frac{(1-k_1)^2}{M_e(1-k_2)}, \qquad [14]$$

$$F_h = \frac{k_2 - k_1^2}{k_1^2(1-k_2)} M_h - 2\left[\frac{k_2(1-k_1)}{k_1^2(1-k_2)} - 1\right] + \frac{(1-k_1)^2 k_2}{k_1^2(1-k_2)M_h}. \qquad [15]$$

Here, k_2 is another weighted ionization rate ratio given by

$$k_2 = \int_{x_1}^{x_2} \beta M^2 dx \Big/ \int_{x_1}^{x_2} \alpha M^2 dx \qquad [16]$$

For most practical applications F_e and F_h can be simplified by writing

$$F_e = k_{eff} M_e + (2 - 1/M_e)(1 - k_{eff}) \qquad [14a]$$

$$F_h = k'_{eff} M_h - (2 - 1/M_h)(k'_{eff} - 1), \qquad [14b]$$

where

$$k_{eff} = \frac{k_2 - k_1^2}{1 - k_2} \approx k_2$$

$$k'_{eff} = \frac{k_{eff}}{k_1^2} \approx \frac{k_2}{k_1^2} \qquad [17]$$

F_e is plotted as a function of M_e and k_{eff} in Fig. 4(a). As can be seen, a small value of k_{eff} is desirable to keep the excess noise

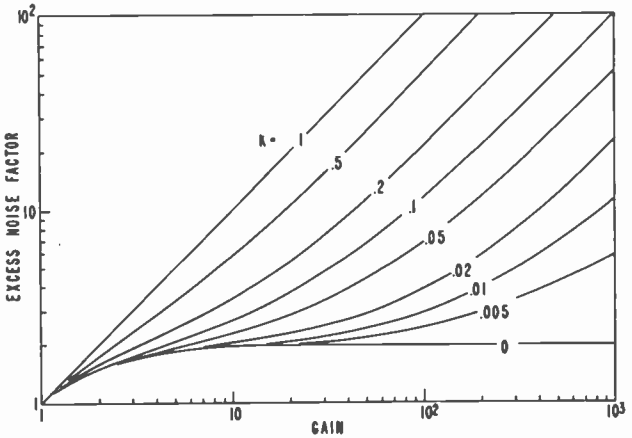

(a)

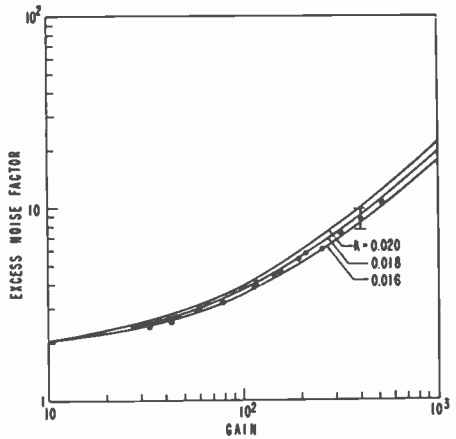

(b)

Fig. 4—(a) Excess noise factor as a function of electron gain M_e and k_{eff}; (b) experimental results for a silicon reach-through diode.

factor at an acceptable minimum. Some experimental results for F_e versus M_e for a reach-through avalanche diode made in these laboratories are plotted in Fig. 4(b).[5] As can be seen, agreement with the computed curve for $k_{eff} = 0.02$, the k-value computed from the ionization rate data of Lee et al[3] and the electric field distribution of the diode, is very good.

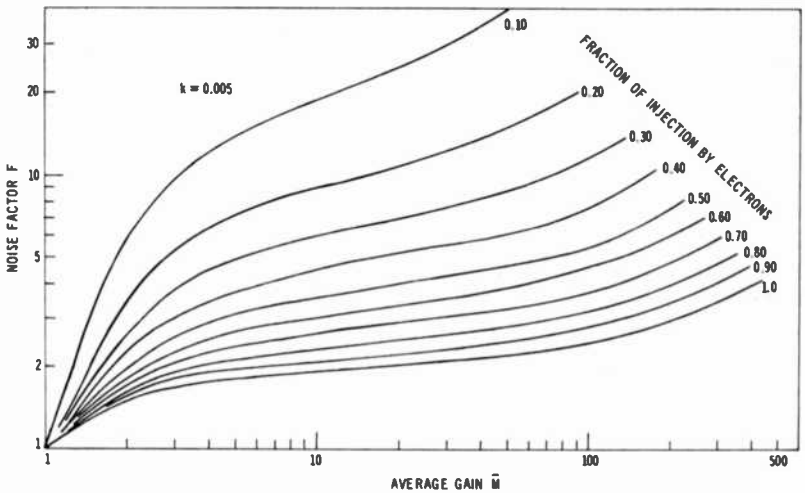

Fig. 4(c)—Excess noise factor for mixed injection ($k_{eff} = 0.005$).

At this point we make a comment regarding a commonly used approximation for the dependence of the avalanche noise on gain. It has become fairly common to say that the noise spectral density in the multiplied current is given by $2qI_oM^{2+\alpha}$ or $2qI_oM^d$ rather than by $2qI_oM^2F$, where α and d for silicon are stated to be anywhere from 0.3 to 0.5 and 2.3 to 2.5, respectively.[6] If this approximation were true, then $F = M^\alpha$ and a log-log plot of F versus M would be a straight line. A quick glance at Fig. 4(a) shows that this is a poor approximation for all k except $k = 1$. Since the excess noise factor provides a direct quantitative measure of the excess noise introduced by the avalanche process, the above approximation obscures the simple physical picture of things as well. Furthermore, since F_e is determined primarily by k_2, the excess noise factor is not only material dependent but also structure dependent, so that a unique value for the gain dependence of the avalanche noise generated in a particular material cannot be assigned. This is a consequence of the electric field dependence of the ionization rates for electrons and holes, the ratio of

which (β/α) is very small in silicon for small fields but becomes larger at higher fields.[3] Thus, in general, the lower the peak electric field at breakdown and, hence, the higher the breakdown voltage, the lower the values of k_{eff} and F_e. Also for silicon junctions, k_2 is smaller in an n+p junction than it is in a p+n junction having the same depletion layer width and peak field. The reason for this is that the weighting factor M^2 which appears in the expression for k_2 (see Eq. [13]) is much larger on the p-side of the high-field region than on the n-side. Thus the low-field values of the ratio β/α are given more weight in the integrals of Eq. [13] for an n+p junction than for a p+n junction.

When light is absorbed on both sides of the junction, so that both electron and hole currents are injected into the multiplying region, the *effective* noise factor is given by

$$F_{eff} = \frac{fM_e^2F_e + (1-f)M_h^2F_h}{[fM_e + (1-f)M_h]^2}, \qquad [18]$$

where $f = I_{no}/(I_{po} + I_{no})$ is the ratio of the electron to the total injected current. F_{eff} is plotted in Fig. 4(c) as a function of the injection ratio f for a diode having a k_{eff} of 0.005, indicating that a low k_{eff} is not sufficient for low noise unless most of the light is also absorbed on the correct side of the junction.

Physically, the reason for the increase in the effective excess noise factor is rather simple. If we have mixed injection, then to achieve an average gain $\overline{M}$ (see Eq. [8]), the diode must be operated at a voltage that can produce an electron gain considerably higher than the average gain, thereby increasing the excess noise factor.

2.4 Gain Probability Distribution

For pulse-coded modulation systems, a knowledge of the noise factor and the dark current is not sufficient to allow the prediction of error rates. If the amplitude distribution of gains were Gaussian, one would expect that a light pulse that contained on average n_p photons and that generated, again on average, $n_e = \eta n_p$ hole–electron pairs in the detector (where η is the quantum efficiency) would result in a pulse of m electrons, for which the probability distribution is Gaussian:

$$P(x) = \frac{1}{(2\pi)^{1/2}} \exp\left\{-\frac{x^2}{2}\right\} \qquad [19]$$

where $x = (m - n_eM)/\sigma$, $\sigma^2 = n_eM^2F_e$.

The actual distribution has been shown to differ substantially from this.[4,7-9] It is rather complicated, but can be approximated with fairly good accuracy by

$$P(x) = \frac{1}{(2\pi)^{1/2}} \frac{1}{(1 + x/\lambda)^{3/2}} \exp\left\{-\frac{x^2}{2(1 + x/\lambda)}\right\},$$

$$-\frac{(F_e - 1)}{F_e}\frac{(M-1)}{M} < \frac{x}{\lambda} < \infty, \qquad [20]$$

where $\lambda = (n_e F)^{1/2}/(F_e - 1)$. We have assumed that all the light is absorbed on the p-side of the junction, so that only primary electrons enter the avalanche region, and that the number of primary electrons has a Poisson distribution. Obviously, the actual distribution approaches the Gaussian shape only for λ large (i.e., for $n_e/F_e \gg 1$.) If such is not the case, the Gaussian approximation cannot be used for estimating probable bit error rates. This is particularly important in estimating the probable error rates due to pulses initiated by a few electron–hole pairs, be they thermally generated or due to less than 100% modulation depth of the digitally modulated signal. For a given modulation depth and amplifier noise, there will be an optimum gain that minimizes the bit error rate.

As an illustration of the importance of using the proper amplitude distribution of gains, we show in Fig. 5 calculated amplitude distributions of "on" and "off" pulses such as might be produced in a system with a modulation depth of 99%. We assume that there are on average 250 and 2.5 primary electrons in the on and off pulses, respectively, that are distributed in a Poisson fashion, and that we are using a diode with $k_{\text{eff}} = 0.02$ and a gain of 100. Three amplitude distributions are shown for each type of pulse. The dashed curves are calculated assuming Gaussian distributions with $\sigma^2 = \bar{n}M^2$ (i.e., an ideal detector) and $\sigma^2 = \bar{n}M^2F$ (i.e., detector noise is included but Gaussian distribution is assumed); the solid curves are computed using the correct distribution. Obviously, considerable error results from using a Gaussian distribution, even when we include broadening due to the inclusion of the excess noise factor; this is particularly so for the "off" pulse. This would result in considerable error in the optimum amplifier discriminator setting for minimum overall error rates in a digital system.

As a second example, Table 1 gives the minimum number of photoelectrons n_{min}, and optimum gain required to give a bit-error-rate of 10^{-10} for both the "on" and "off" pulses when the modulation depth

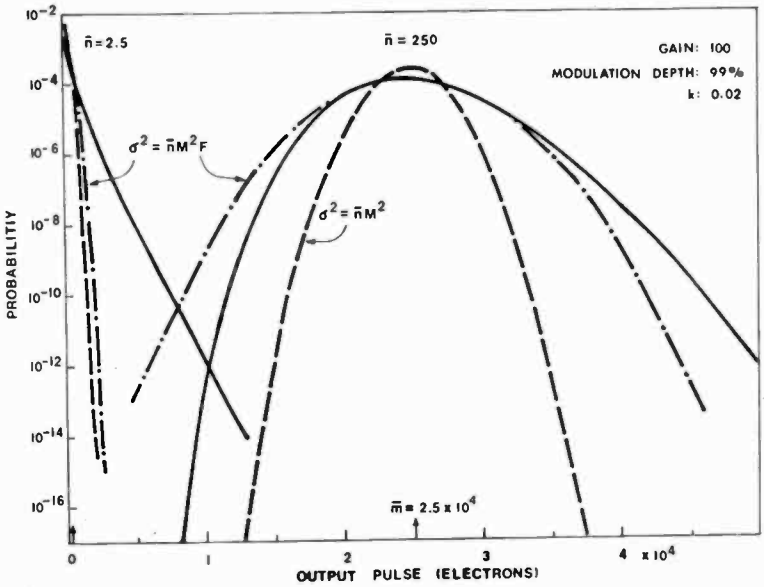

Fig. 5—Calculated gain distributions of "on" and "off" pulses assuming a modulation depth of 99%, diode gain = 100, $k_{eff} = 0.02$ and an average of 250 primary photoelectrons in the "on" pulse. The dashed curves correspond to Gaussian distributions with $\sigma^2 = \bar{n}M^2$ and $\sigma^2 = nM^2F$. The solid curves are calculated using the proper gain distribution.

Table 1—Comparison of the minimum number of primary photoelectrons n_{min} required from an 'on' pulse of a PCM optical communications system to give a bit error rate of 10^{-10} when the modulation depth is 99%: (a) threshold set to pass pulses of 2×10^4 electrons or more and (b) threshold set at 4×10^3 electrons.

	Ideal Detector ($F = 1$)		Aval. Photodiode		
	Poisson Dist.	Eq. 20	$k = 0$	$k = .02$	$k = 1$
(a) $m = 2 \times 10^4$					
n_{min}	46	49	115	328	1820
M_{opt}	large	—	550	150	25
F_e	1	1	2	5.0	25
n_{min}/F_e	46	49	57	65	73
(b) $m = 4 \times 10^3$					
n_{min}	46	49	115	198	793
M_{opt}	large	—	110	54	11.0
F_e	1	1	2	3.0	11.0
n_{min}/F_e	46	49	57	66	72

is 99%. These numbers have been calculated by integrating Eq. [20] and assuming that the amplifier discriminator is set to pass pulses containing more than m electrons, where m is determined by the noise in the preamplifier and is taken to be equal to 2×10^4 and to 4×10^3 (a and b in Table 1). Also shown is the number of photoelectrons required by an ideal noiseless detector, as calculated both from the actual Poisson distribution and from Eq. [20].

This example is instructive in that it illustrates the considerable advantage to be gained by (a) keeping k_{eff} small and (b) improving the preamplifier. It also illustrates the futility of trying to make high speed avalanche photodiodes out of any material for which k is *not* close to zero. Note that, to a first approximation, n/F_e is more or less constant, although it increases somewhat with increasing k. Since n is proportional to η, F_e is approximately proportional to kM, and M_{min} is more or less proportional to $k^{-1/2}$, the ratio $\eta/k^{1/2}$ is a useful figure of merit in comparing two types of avalanche detectors.

2.5 Linearity and Frequency Response

Avalanche photodiodes are linear over many orders of magnitude of incident light level, from the lowest detectable signal level (10^{-14} to 10^{-8} watts, depending on the bandwidth and quantum efficiency) up to incident power levels at which some gain saturation occurs. Gain saturation can occur due to a number of effects. The most obvious, and usually the most important at low frequencies in circuits designed for low noise, is the gain reduction that results from the voltage drop across the load resistance. This reduces the voltage across the diode and consequently the gain. Other effects that can reduce the gain are (1) space-charge effects, in which mobile charge in the drift region increases the electric field in the drift region and decreases the electric field in the avalanche region, thereby reducing the gain, and (2) heating effects, in which the increase in temperature resulting from the power being dissipated reduces the gain. These effects are discussed in detail in the Appendix.

The frequency response can be limited by either transit-time effects or by the time for multiplication. The transit-time limitation is the main one for most avalanche diodes, and usually takes the form $\sin \pi f \tau_t / (\pi f \tau_t)$ where τ_t is the transit time of the multiplied carriers across the depletion layer (see Appendix for more exact expressions). The time for multiplication, in most avalanche diodes, is sufficiently short so as not to be a limitation until the gain–bandwidth product exceeds a few hundred GHz. Under these conditions, the frequency dependent gain can be written

$$M(\omega) = \frac{M(o)}{1 + j\omega\tau_m M(o)} \qquad [21]$$

where $M(o)$ is the low-frequency gain. Typically, τ_m is about 1 picosecond or less.

The effects of gain saturation and frequency response are analyzed more completely in the Appendix, and an equivalent circuit of the diode is derived that takes into account all of these effects, at least to a first approximation.

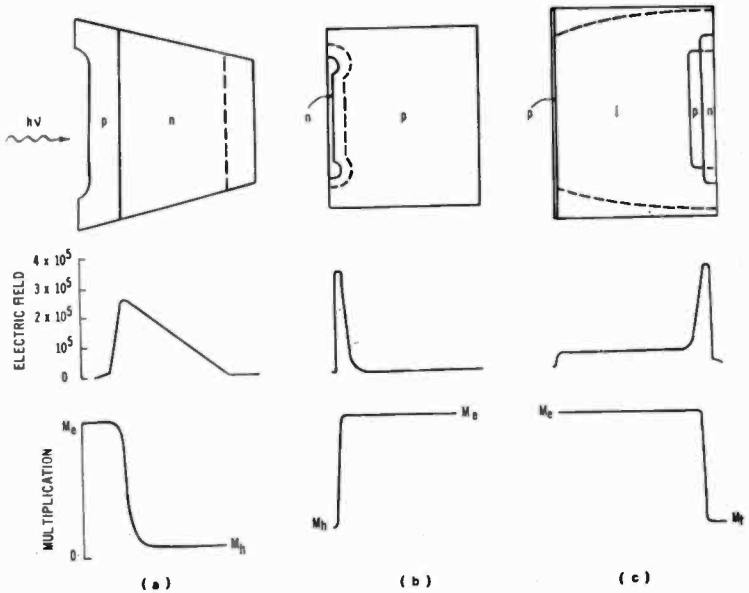

Fig. 6—Structures of three commercially available silicon avalanche photodiodes: (a) beveled edge diode, (b) guard ring structure, and (c) reach-through structure.

3. Comparison of Avalanche Photodiode Structures

Fig. 6 shows three different silicon avalanche photodiode structures that are now commercially available. Structure (a), the "beveled-edge" diode, is a p+n junction in which the n-type resistivity is chosen so as to make the breakdown voltage very high, typically 1800-2600 volts, thereby yielding a device with a wide depletion layer. Breakdown at the junction periphery is prevented by physically beveling the edges of the diode. The junction is usually quite deep, perhaps about 50 to

75 μm; in some instances, this "dead layer" is reduced by etching a "well" in the p-layer as shown. Since in silicon, holes do not multiply as readily as electrons,[3] this device has the advantage of having a low multiplied dark current (most of the carriers that contribute to the bulk dark current are holes). Thus, the multiplication M is a function of where the carriers are generated, as shown in Fig. 6. On the other hand, the only portion of the signal that gets multiplied effectively is that absorbed in the p-layer. Unfortunately, there is very little electric field in this region, and so it takes from 10 to 30 ns for this charge to be collected. Consequently, one has a Hobson's choice with this device between slow response and high gain at short wavelengths ($\lambda < 0.9$ μm) and fast response and low effective gain at long wavelengths ($\lambda > 0.9$ μm).

A second common structure, often called the "guard-ring" structure, is shown in Fig. 6(b). This can be made either n+ on p or p+ on n, with a possible variation being the use of a Schottky barrier plus guard ring instead of a diffused junction. The device shown has a junction depth of 1 to 2 μm and a depletion layer depth of about 10 to 15 μm. Since it is desirable to generate carriers on the p-side of the junction, this structure works well for wavelengths for which the absorption coefficient is between 5×10^3/cm and 10^3/cm, which in silicon is the wavelength range 0.6 to 0.8 μm. For longer wavelengths, much of the light penetrates through to the undepleted region and some of the resulting photogenerated carriers are collected by diffusion and multiplied. They are collected slowly however, and so do not contribute to the high-frequency response of the diode. These carriers do, however, constitute an additional noise source, and the performance of this structure may be quantum-noise limited in many high-frequency applications involving penetrating radiation, which for this structure can be as short as 0.80 μm. Typical high-frequency quantum efficiencies with this device are about 30% at 0.9 μm and 1 to 2% at 1.06 μm.

The third structure shown[10] is the "reach-through" diode.[5,7,11,12] It combines, to the best extent possible, high speed, high gain, and, as we shall see, relatively low noise. It does this by separating the depletion region into two separate regions—a wide drift region in which the photons are absorbed and a narrow multiplying region in which the photogenerated carriers are multiplied.

Fig. 6c illustrates the diode configuration. The two diffusions, p-type (boron) and n-type (phosphorus), that create the avalanche region are carried out in sequence and are so adjusted that when a reverse bias voltage is applied, the depletion layer of the diode just "reaches-through" to the low concentration π region when the peak

electric field at the junction is 5-10% less than that required to cause avalanche breakdown. Additional applied voltage then causes the depletion layer to increase rapidly out to the p+ contact, while the field throughout the device increases relatively slowly.

The π region of the device, which is the substrate crystal, is typically about 5000 ohm-cm resistivity. Thus widths up to 200 μm can be depleted with the application of less than 100 volts bias over and above that required to achieve reach-through. In all cases, the device is operated only in the fully depleted mode, so that all carriers are collected by drift alone. This has important consequences regarding speed of response, as will be seen in subsequent discussion.

Since electrons are more strongly ionizing than holes in silicon, optimum conditions are obtained when the incident radiation is absorbed in the π region. The fully depleted structure allows the device to be used with radiation entering the p+ contact. Electrons absorbed in the π region are swept to the high field region, where multiplication occurs. The resulting holes produced there traverse the π region to the p+ contact, and constitute the main portion of the multiplied signal.

The electric field profile for this diode is shown in Fig. 6c. Avalanche multiplication occurs in the high field region around the p-n junction (typically about 2 μm in width). The field in the π region, although relatively low, is sufficiently high to assure carrier velocities approaching saturation, giving rise to electron and hole transit times in the range 0.5-5 nanoseconds, depending on slice thickness and applied bias.

Fig. 7 illustrates the three general gain–voltage characteristics that can occur during the final n-type diffusion: (1) n-type impurity not adequately diffused so that avalanche occurs before reach-through is achieved; (2) the desired condition where reach-through occurs just as the gain has risen to some intermediate value, typically 10 to 20, beyond which point additional applied voltage gradually increases the field and hence gain; (3) phosphorus diffused too far, so that useful gain would be achieved in the device only at excessively high voltages.

While reach-through avalanche diodes thicker than 200 μm can be and have been made, practical considerations, such as increased difficulty of fabrication and temperature compensation problems, have combined to limit the sensitive thicknesses to the range 50-200 μm. With this range of sensitive thicknesses, the drift region occupies greater than 90% of the total wafer thickness, so that practically every photon of any wavelength absorbed in the device contributes usefully

to the multiplied current. This also avoids any substantial increase in the effective excess noise factor due to mixed injection.

For example, the beveled edge structure shown in Fig. 6(a) probably has a k_{eff} value between 0.005 and 0.01, but an f (the ratio of the electron current to the total injected current) of only about 0.2 or less when used at 1.06 μm, so that the effective noise factor is very high. The reach-through structure, on the other hand, has a k_{eff} of 0.02 as shown in Fig. 4(b)[5] and an f of 0.95 to 0.98 at 1.06 μm, so that F_{eff} and F_e are almost identical.

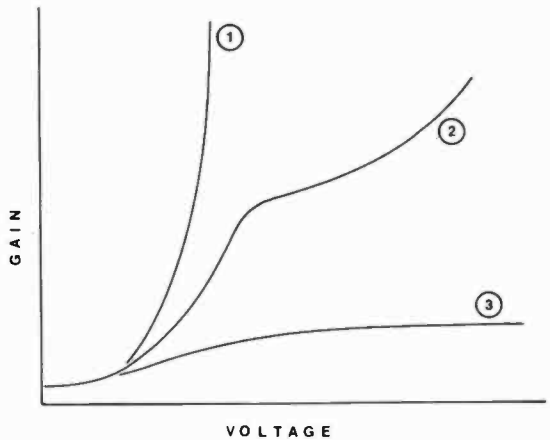

Fig. 7—Gain–voltage characteristics encountered at various stages of processing.

4. Properties of Reach-Through Avalanche Photodiodes

4.1 Quantum Efficiency

An important consideration in selecting any detector is its quantum efficiency, defined as that fraction of the incident photon flux that generates electron–hole pairs that are collected by the detector contacts. In detectors that are not fully depleted this may include electron–hole pairs generated in the undepleted or base layer, which are collected by diffusion. These carriers are responsible for the "tail" or long fall times seen in the pulse response of some photodiodes, and they contribute to a quantum efficiency measured at low frequencies but do not contribute to the height of a pulse in a wideband system. In the case of the reach-through avalanche photodiode, or any other fully depleted photodiode, this tail is absent and the quantum efficiency is constant over the full bandwidth of the detector. In this case, the quantum efficiency is given by

$$\eta = \frac{(1 - r_1)[1 - \exp(-\alpha_o w)][1 + r_2 \exp(-\alpha_o(w + 2d_2))] \exp(-\alpha_o d_1)}{1 - r_1 r_2 \exp[-2\alpha_o(w + d_1 + d_2)]}, \quad [22]$$

where r_1 and r_2 are the reflectivities of the front and back surfaces respectively, d_1 and d_2 are the effective thicknesses of the front and back contact regions, w is the thickness of the active layer, and α_o is the optical absorption coefficient at a specified wavelength and temperature.

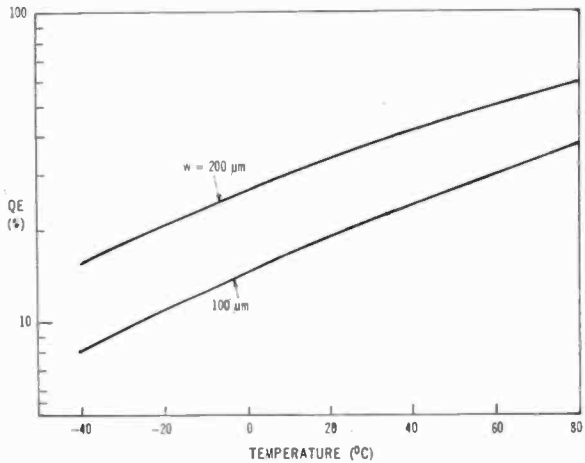

Fig. 8—Quantum efficiency at 1.06 μm as a function of temperature, calculated using the absorption data of MacFarlane et al.[13]

Thus to maximize η, r_1 should be minimized by use of an anti-reflection coating, r_2 should be made as large as possible by using a highly reflective metal for the back contact, $\alpha_o w$ should be much larger than unity if possible, and d_1 and d_2 should be as small as possible. It is particularly important that d_1 be kept small if the detector is to be used in the visible and ultraviolet, where α_o is greater than 10^4 cm^{-1}.

For reasonable yields of avalanche diodes, w is usually ~100 μm. This gives a substantially temperature independent quantum efficiency (Q.E.) of ~90% at 0.9 μm; at 1.06 μm the Q.E. is ~20% at room temperature and has the temperature dependence shown in Fig. 8. At shorter wavelengths Q.E. is limited primarily by d_1, which is a small fraction of a micrometer and is also substantially temperature independent. A typical room temperature Q.E. versus wavelength curve is shown in Fig. 9. The drop in Q.E. from 90% at 0.9 μm to ~60% at 0.45 μm is due almost entirely to the change in reflectivity of the detector, which has been anti-reflection-coated for 0.9 μm with SiO.

4.2 Speed of Response

The response time of the reach-through avalanche photodiode is determined by the transit time of the photogenerated and multiplied carriers across the depletion layer. These carriers must first be collected in a time equal to or less than an electron transit time, $\tau_e = w/v_e$, depending on where the carrier was generated. Here v_e is the average

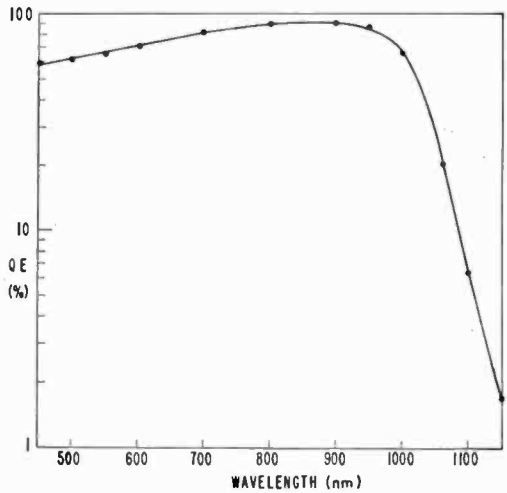

Fig. 9—Quantum efficiency of a typical reach-through avalanche diode (Type C30817) as a function of wavelength.

drift velocity of electrons in the drift region. After collection, electrons undergo multiplication, the time for which is very short, varying from just the transit time of the high field region (2×10^{-11} sec) at low gains to about 4×10^{-13} M sec at high gains, where M is the gain. Thus, for all practical purposes, the multiplication can be considered to occur instantaneously. The resultant holes must then also traverse the depletion layer. The resultant pulse shape, for a delta-function light pulse, depends somewhat on where the light is absorbed, as illustrated in Fig. 10. In all cases, the total pulse duration is less than or equal to the total of the electron and hole transit times, and the pulse width at half maximum is equal to the hole transit time. Expressions for the frequency response of the diode are derived in the Appendix.

The estimated pulse widths at the 10% points are shown in Fig. 11 as a function of voltage and width of the drift region for $\lambda = 0.9$ μm and 1.06 μm, using the drift velocity data of Quaranta et al.[14,15] It is

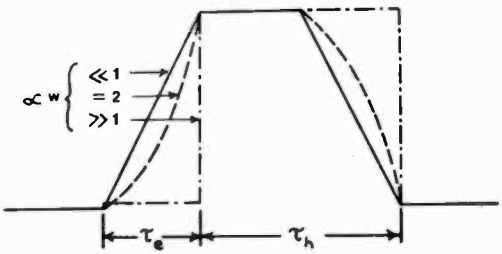

Fig. 10—Impulse response of reach-through avalanche diodes in which $\tau_A \approx 2\tau_e$. $\alpha w \ll 1$ corresponds approximately to 1.06 μm, $\alpha w = 2$ to 0.9 μm, and $\alpha w \gg 1$ to visible light.

obvious that by making the diode thinner, the response time can be decreased to less than 1 ns. However, there is a price paid in quantum efficiency for this speed; the estimated quantum efficiencies at 0.9 μm and at 1.06 μm are shown in Table 2. Note that some of the lost quantum efficiency can be regained by heating the diode. This also increases the dark current, but probably not enough to affect performance, since high-speed operation is usually accompanied by a high effective background level (i.e., the noise-in-signal is greater than the dark-current noise).

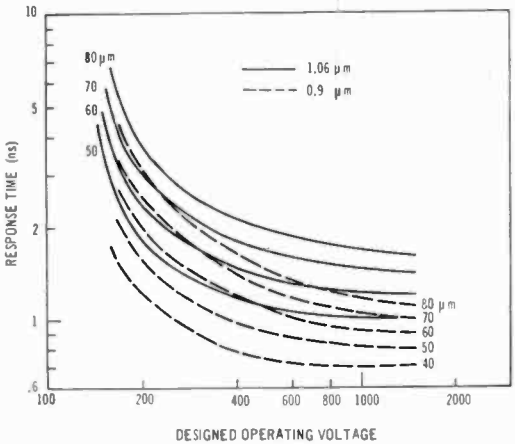

Fig. 11—Pulse widths (10% points) as a function of voltage and width of the drift region for $\lambda \sim 0.9$ and 1.06 μm, calculated using the drift velocity data of Quaranta et al.[14,15]

4.3 Noise Equivalent Power

Of particular interest to the user of such a device, is its Noise Equivalent Power given by

$$\mathrm{NEP} = \frac{i_n}{RB^{1/2}} \qquad [23]$$

where i_n^2/B is the system noise current power spectral density given by

$$i_n^2 = 2q[I_{ds} + I_{dt}M^2F]B + i_{na}^2 \qquad [24]$$

and R is the diode responsivity given by

$$R = \frac{q\eta\lambda M}{hc} = R_oM, \qquad [25]$$

where R_o is the unity gain responsivity.

Table 2—Calculated achievable quantum efficiencies with silicon avalanche photodiodes. Assumed values of r_1 and r_2 are 0.10 and 0.90, respectively.

DEPLETION LAYER WIDTH (μm)	QUANTUM EFFICIENCY			
	0.9 μm	1.06 μm		
	300°K	300°K	325°K	350°K
40	0.766	0.094	0.118	0.167
50	0.812	0.116	0.146	0.206
60	0.841	0.137	0.172	0.240
70	0.861	0.158	0.199	0.273
80	0.873	0.177	0.223	0.305

Here I_{ds} is the detector surface dark current, which is not multiplied and which is normally the dominant current in the avalanche diode (it does not provide the dominant noise current, however, except at very low gains); I_{dt} is the total bulk current, composed of the detector dark current I_{db} plus the background induced current P_oR_o, both of which are multiplied, and i_{na} is an equivalent amplifier noise current.

As noted earlier the main contributing factor to the noise, except

at low gains or wide bandwidths is the noise generated by the avalanche process. If dark conditions are assumed, then at higher gains the amplifier and surface current contributions become negligible and the dominant contributions is $2qI_{db}M^2F$. From measurements on a relatively large sample of devices, the room temperature surface current ranges from ~75 nA for a 1-mm-diameter diode to ~0.3 μA for a 4-mm-diameter diode, varying approximately in a linear fashion with diode circumference. I_{db} is typically 3×10^{-11} to 1×10^{-10} A/mm^2 for a device with a 100-μm-thick depletion region.

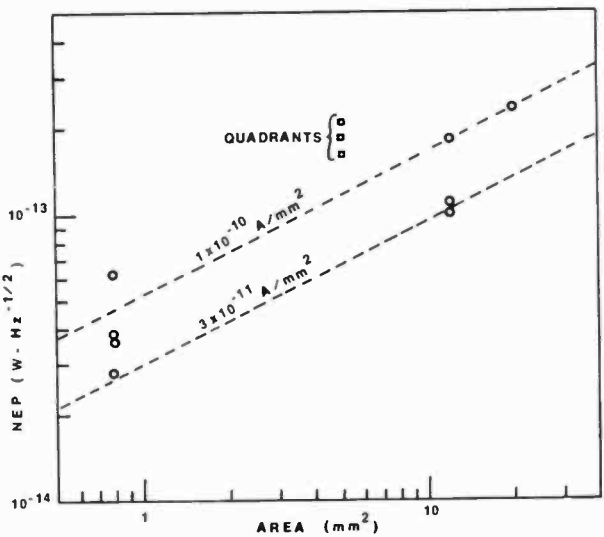

Fig. 12—NEP (1.06 μm) as a function of area for a gain of 30.

Fig. 12 shows lines of NEP at 1.06 μm as a function of area for these two quasi-limits of I_{db} for a gain of 30. NEP's for a number of typical devices have been plotted on the graph. Most small-area devices have some amplifier contribution to the noise at a gain of 30; on the other hand, the effective area is somewhat less than the nominal 0.78 mm^2 due to electrostatic edge effects, which tend to reduce the peak field in the avalanche region over a distance in from the edge on the order of the slice thickness. The two effects tend to be somewhat compensating in terms of position on the graph relative to the calculated lines.

Also of interest to a user is the variation of the NEP with gain, since in certain applications low gains will be adequate, while in others, high gains are necessary. NEP as a function of gain should

follow a $\sqrt{F}$ versus M curve in the absence of other limiting factors. Fig. 13 shows the NEP for three typical devices of varying areas and for a quadrant device, more about which will be said below. The

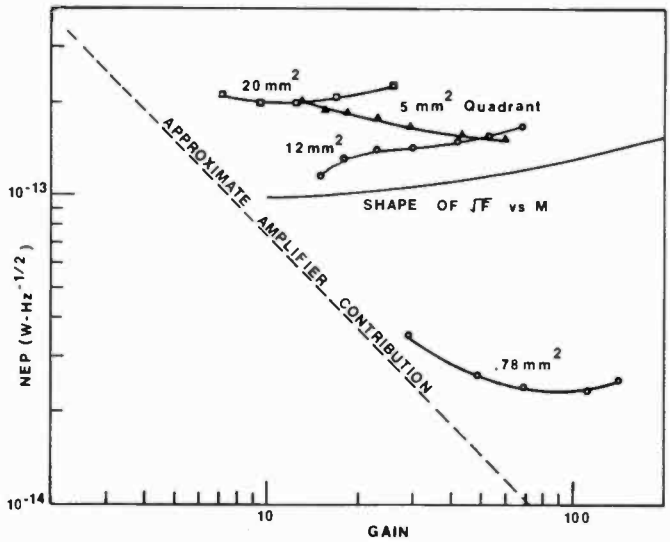

Fig. 13—NEP (1.06 μm) as a function of gain for various device sizes. Also shown is the amplifier contribution and the shape of the $\sqrt{F}$ versus M relationship.

approximate amplifier contribution is also plotted, thus indicating that at low gains the amplifier was a limiting factor for the particular measuring system used. A reduction in the effective area with increasing gain for the small unit is also responsible for some of the decrease in NEP with increasing gain below 100. Similarly, for the 20 mm² unit, a relatively high surface current is undoubtedly a contributing factor at the lowest gains. The results for the quadrant device are discussed later.

Fig. 14 summarizes the voltage dependence of the dark current, responsivity at 1.06 μm, and the NEP (1.06 μm) of a typical 1-mm-diameter detector. At 0.9 μm the responsivity would be approximately a factor of four higher and the NEP a factor four lower.

4.4 Temperature Effects

In addition to the effect of temperature on the quantum efficiency at 1.06 μm, the avalanche gain is also temperature dependent due to the temperature dependence of the electron and hole ionization rates.[3,5,16]

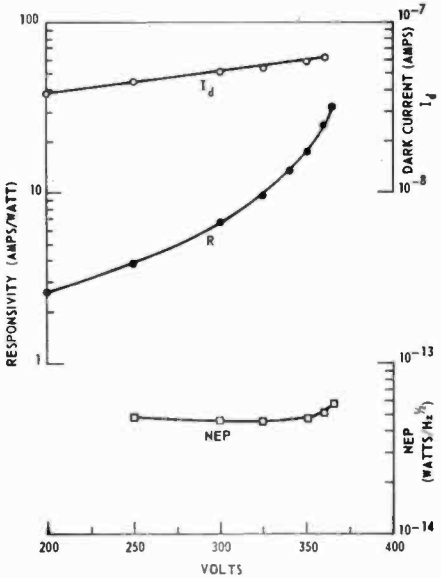

Fig. 14—Typical measured characteristics for Type C30817 1-mm-diameter reach-through avalanche diode at 1.06 μm. At 0.9 μm, the responsitivity is typically a factor of 4 higher and the NEP a factor of 4 lower.

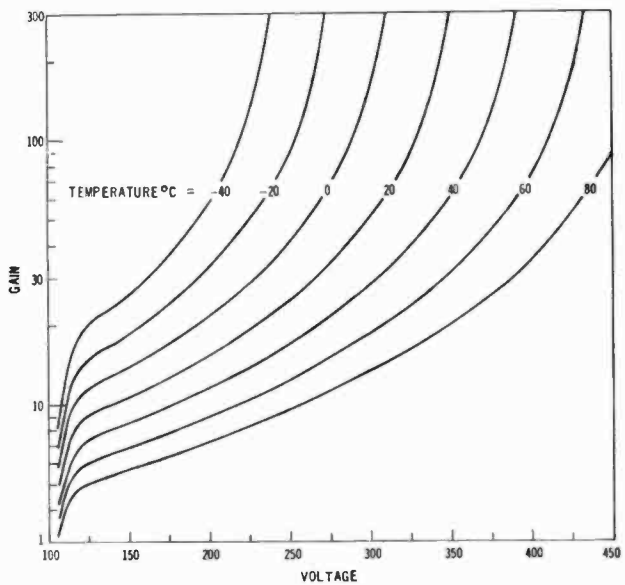

Fig. 15—Typical gain–voltage–temperature curves for the reach-through avalanche diode. Depletion width ~ 100 μm.

This effect can be incorporated into the calculation of the avalanche gain, with excellent agreement between measured and computed gains.[5] The temperature dependence of the avalanche gain of a typical detector having a depletion width of 100 μm is shown in Fig. 15. The spread in this family of gain–voltage curves is a linear function of the depletion width and can be understood in simple physical terms if we consider that the electric field E in the multiplying region of the device is composed of two independent but additive components E_d and E_a. Here E_d is the electric field that exists in the multiplying region at a bias V_d corresponding to the reach-through voltage (i.e., the voltage at which the depletion layer extends through the diffused p region); E_d depends only on the distribution of the diffused impurities and not on the width w of the drift region or on the operating voltage of the device other than through V_d. On the other hand, $E_a = (qN_aw/\epsilon) + (\Delta V/w)$ is independent of E_d, and hence of the diffusion conditions, and depends on N_a the acceptor concentration of the base material, w the width of the drift region, and the incremental voltage ΔV applied over and above that required to fully deplete the diode.

Now if the operating temperature decreases and the applied bias is kept constant, the ionization rates for electrons and holes will increase and so will the avalanche gain. Thus to maintain constant gain as the temperature is lowered, the electric field in the multiplying region of the junction must be lowered, and this can be effected only through the term $\Delta V/w$. Thus, for devices with the same E_d but different depletion widths, the change in bias required to maintain constant gain is proportional to w. This allows us to construct a set of "universal" gain–voltage curves such as those shown in Fig. 16, where to maintain constant gain the bias needs to be changed by about 1.8 V/°C/100 μm of depletion width, independent of gain. These curves are "universal" in the sense that they can be applied to this reach-through diode independently of slice thickness and breakdown voltage. They are not applicable to other avalanche photodiode structures where different electric field distributions exist in the multiplying part of the junction.

A family of responsivity–voltage–temperature curves will have the same shape as the gain–voltage curves at wavelengths where the quantum efficiency is temperature independent ($\lambda < 0.95$ μm for temperatures above -40°C and depletion widths ≥ 100 μm). At 1.06 μm the quantum efficiency is quite strongly temperature dependent and this dependence must be included. However, because the Q.E. versus temperature curves of Fig. 8 have slopes that depend on thickness, it is not possible to construct a single family of "universal" responsivity (1.06 μm)–voltage–temperature curves. Moreover, the voltage change

per °C required to maintain constant responsivity at 1.06 μm is not independent of responsivity. The change depends both on responsivity and depletion width. A set of responsivity curves is shown in Fig. 17 for a detector with a 100 μm depletion width.

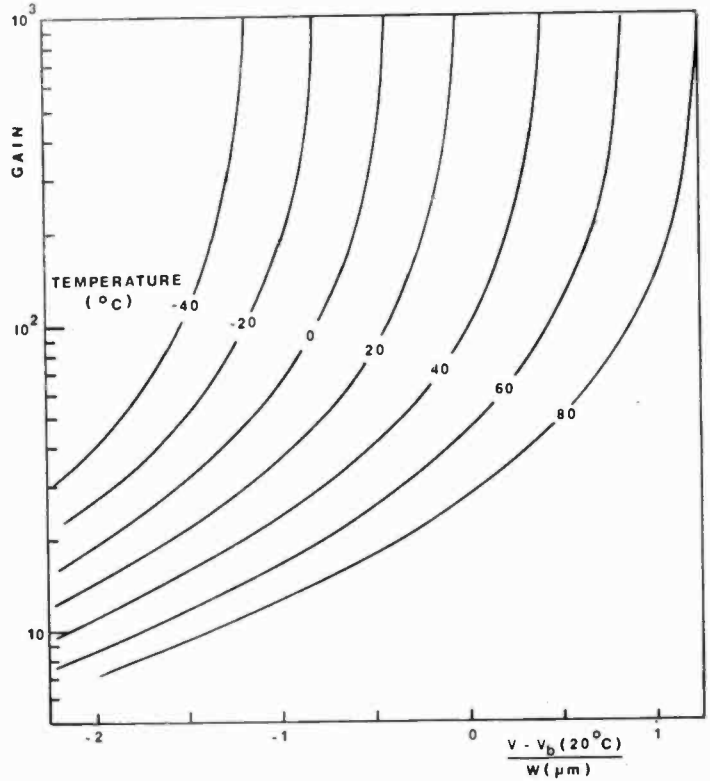

Fig. 16—"Universal" gain–voltage curves for the reach-through avalanche diode.

It is also instructive to examine noise equivalent power in an avalanche diode as a function of temperature, since many applications will involve operation over a substantial temperature range. Fig. 18 shows one such series of measurements, taken at 1.06 μm and at a constant responsivity of 5.2 A/W, for a 12 mm^2 unit over the temperature range −30° to +72°C. The calculated curve in Fig. 18 assumes a generated current in the multiplying region varying as exp $[-E_g/(2kT)]$, as is expected for a fully depleted region. The curve then corresponds to an injected current (into the multiplying region) of

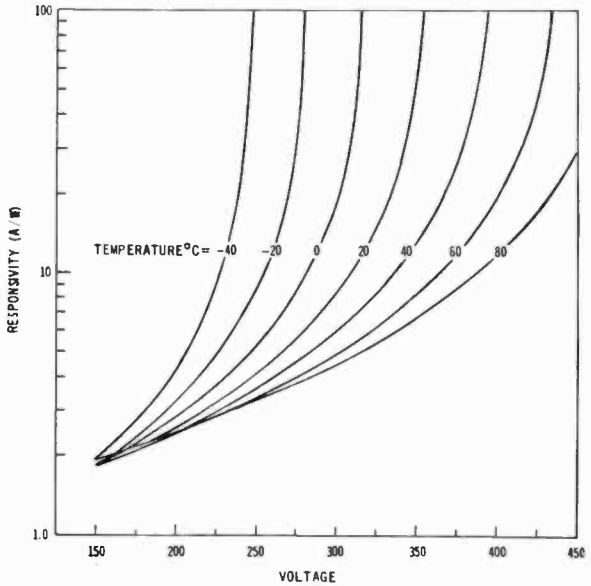

Fig. 17—Typical responsivity at $\lambda = 1.06$ μm as a function of voltage and temperature for the reach-through avalanche diode.

approximately 1.2×10^{-10} A/mm^2 at 20°C for a unit whose sensitive thickness is 160 μm. The deviation at the low-temperature end is partly due to amplifier limitation, but probably also due to nonuniform gain

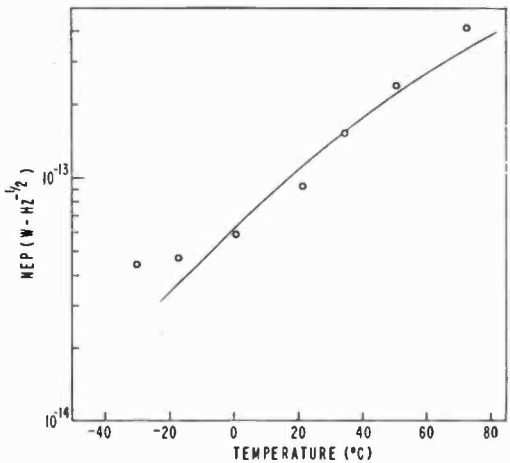

Fig. 18—Calculated and measured NEP (1.06 μm) as a function of temperature at a constant responsivity of 5.2 A/W for a 12 mm^2 diode.

effects, since the gain is considerably higher at low temperatures for a constant responsivity.

4.5 Gain Uniformity

Two methods have been used to examine gain uniformity as a function of position in the avalanche diodes. The first method uses a mechanical scanning system to move a small light spot in a systematic manner across the surface of the device, thus providing a detailed

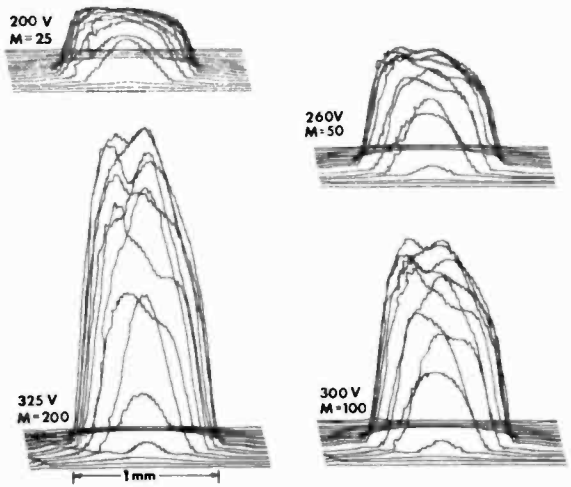

Fig. 19—Gain scans of a 1-mm-diameter diode at peak gains of 25, 50, 100, and 200.

point-by-point measure of the response when connected to an x-y recorder. Fig. 19 shows a series of scans for a 1-mm-diameter diode for several values of peak gain, while Fig. 20 shows a more detailed plot of the gain along a diameter for a different diode. It is quite clear from these figures that at low gains, the gain uniformity is reasonably good. At higher gains, however, the nonuniform field across the device, caused at least in part by electrostatic edge effects, results in higher gain at the center than at the edges. For a gain of 200, an effective width for this device at the half gain points would be approximately 0.70 mm, thus yielding a useful area approximately one half of the total at this gain.

A similar scan for a 20 mm^2 diode is shown in Fig. 21. For this

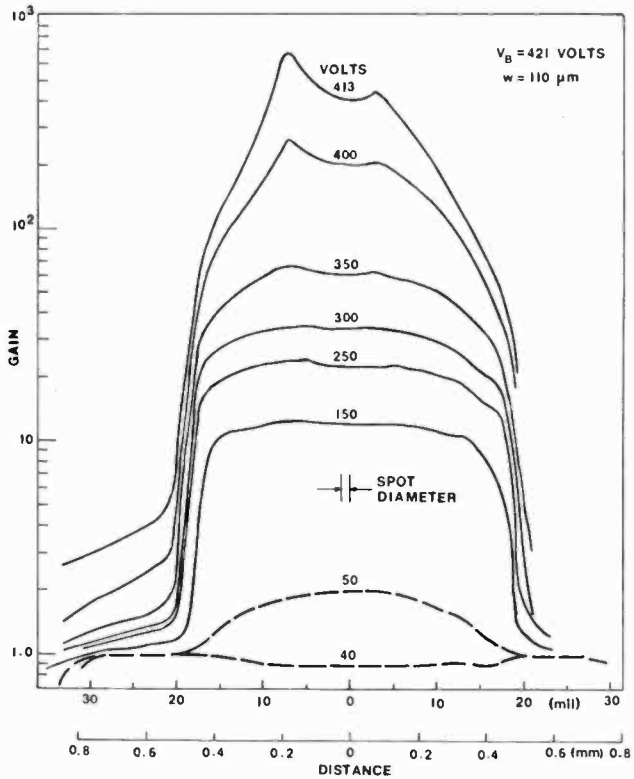

Fig. 20—Gain as a function of position for a 1-mm-diameter diode.

particular device, biased at the voltage indicated, the average gain was determined to be approximately 18. There is a remarkable degree of uniformity in this device, considering the magnitude of the sensitive area.

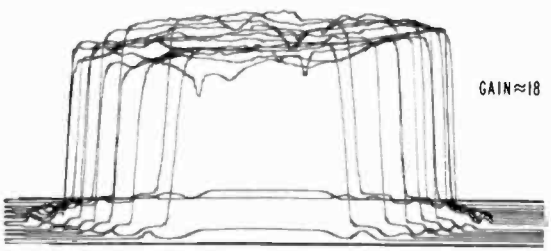

Fig. 21—Gain scan for a 20-mm² diode at a gain of 18.

It should also be mentioned that in the reach-through structure, the uniformity of the diffused boron and phosphorus sources determines the gain uniformity of the detector, since only a small fraction of the p-type impurity is contributed by the substrate crystal. By the use of ion implanted sources and refined diffusion techniques, doping uniformities of ~0.5% can be routinely obtained for devices of 1 mm diameter. This degree of uniformity in the impurity concentration would be extremely difficult to obtain in a bulk crystal, from which other avalanche diode structures are made.

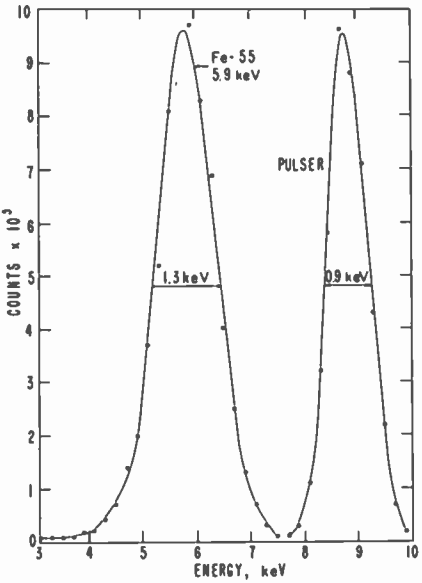

Fig. 22—X-ray spectrum of ^{55}Fe (5.9 keV) taken with a 20 mm² diode.

The second method of assessing gain uniformity is to use the diode to resolve low energy, mono-energetic x-rays, and to compare the width and shape of the peak to that of a pulser run at the same time.[17] The pulser yields a peak whose width is determined by the combination of amplifier and diode noise. Excess width and irregular shape of the x-ray peak will then be mostly due to gain nonuniformity. The 5.9 keV x-ray of ^{55}Fe has been used for this purpose, and one spectrum for a 20 mm² diode is shown in Fig. 22. The full width at half maximum (FWHM) resolution of the x-ray peak is seen to be approximately 1.3 keV, compared to a pulser width of 0.9 keV. If the noise contribution is subtracted quadratically, the remaining FWHM

due to gain nonuniformity would be about 0.93 keV, or about 16%, corresponding to an rms gain variation of only about 6.5%.

The method of x-ray detection in evaluating gain uniformity has considerable merit for two main reasons: (1) the test can be carried out quickly with the use of a multichannel analyzer and (2) an integrated value of gain nonuniformity about an average is obtained.

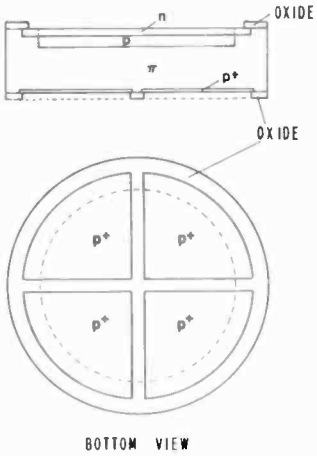

Fig. 23—Quadrant avalanche photodiode structure.

5. Quadrant Avalanche Photodiodes

The structure of the quadrant avalanche diode is indicated in Fig. 23. As can be seen, the only difference between this device and a single element diode is that the p+ contact is diffused through a quadrant-patterned oxide instead of over the entire 'back' surface. This leaves narrow undiffused cross-hairs to separate the quadrants, and the electrical isolation occurs only when the device is fully depleted. Since the p and n diffusions on the junction side are diffused uniformly, and not in a quadrant configuration, the gain over the entire device is uniform and does not drop to unity or zero at the cross-hairs. This is shown to be the case in Fig. 24(a) where a scan has been made with all quadrants connected together. The device behaves as a normal, single-element avalanche diode. To demonstrate the operation of the device in a quadrant mode, a scan was taken with signal coming only from two diagonally opposite quadrants, the others being grounded. This is shown in Fig. 24(b). A more detailed indication of the cross-over between adjacent quadrants is provided in Fig. 24(c), where a

single line scan is plotted across the boundary. The cross-over distance is approximately 0.004 inch, which is also the width of the undiffused cross-hairs.

Extending the depletion layer out to the undiffused silicon surface in the cross-hair region appears to create some problems with respect

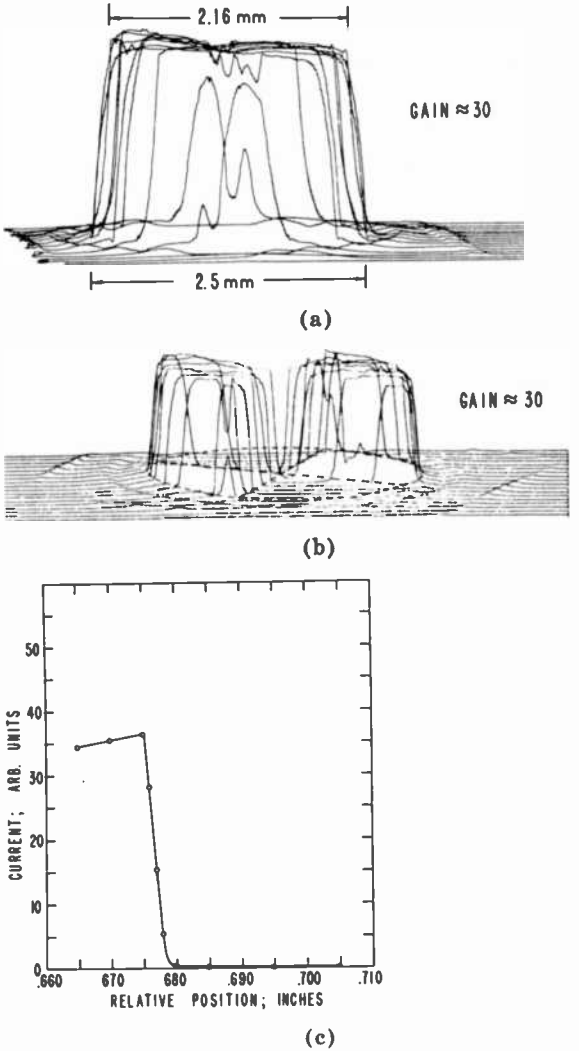

Fig. 24—Gain scan for a quadrant avalanche diode: (a) all quadrants connected together, (b) signal from two diagonally connected quadrants, and (c) details of a single scan across the boundary between two quadrants.

to noise. Clearly, any carrier generation or electron injection at this surface will result in a net increase in the multiplied dark current, since it is all within the multiplying region. This appears to be happening, as indicated by the NEP's for quadrant detectors (all quadrants connected together) which were previously shown in Figures 12 and 13. (The total detector area was 5 mm^2.) It is seen that the noise of the quadrants is somewhat higher than expected on the basis of results for single element devices. A typical value for the dark current generated within the multiplying region is about 3×10^{-10} A/mm^2 compared to 1×10^{-10} A/mm^2 or less for single element devices. However, in spite of the somewhat higher noise, the NEP's are still considered to be within a very useful range.

Conclusions

Basic avalanche mechanisms have been reviewed and discussed in relation to the detection of fast laser pulses particularly at 0.9 and 1.06 μm. It has been shown that avalanche detectors made of materials with nearly equal electron and hole ionization rates would have considerably less uniform gain and would be noisier, much more difficult to make, and much less suitable for the detection of laser pulses than diodes made from materials having a small ratio of ionization coefficients. Moreover, the reach-through structure is a superior structure for the detection of fast low-level laser pulses, particularly at 0.9 and 1.06 μm.

Present day fabrication technologies allow the manufacture of single and multiple element uniformly multiplying reach-through avalanche photodiodes with usable gains of several hundred, areas up to 20 mm^2, and response times of less than one nanosecond.

Acknowledgments

We wish to thank Mrs. J. Sypniewska for her skillful technical assistance in the manufacture of these diodes, T. Doyle for the quantum efficiency data of Figure 9 and A. R. Jones for the x-ray spectrum of Fig. 22.

This work was supported in part by the Defence Research Board of Canada, DRB Grant No. 5567-04, DIR Project E-178.

Appendix—Derivation of an Equivalent Circuit for Avalanche Photodiodes

A. Low-Frequency Circuit

At high light levels, the diode gain becomes a function of current density so that the response becomes nonlinear. Mathematically, if M

is the gain, or multiplication, and I_p is the primary generated photocurrent, the multiplied current is $I = MI_p$. Differentiating, we have

$$\frac{dI}{dI_p} = M + I_p \frac{dM}{dI}\frac{dI}{dI_p}$$

or

$$\frac{dI}{dI_p} = \frac{M}{1 - I_p \dfrac{dM}{dI}}. \qquad [26]$$

The instantaneous value of M, at least at low frequencies, for a given diode depends directly only on the instantaneous value of the electric field in the multiplying region and on temperature. Thus we can write

$$\frac{dM}{dI} = \frac{\partial M}{\partial E_m}\frac{dE_m}{dI} + \frac{\partial M}{\partial T}\frac{dT_m}{dI}, \qquad [27]$$

where E_m and T_m are the maximum values of the electric field and the temperature, respectively, in the multiplying region.

E_m depends on I through the effect of the diode contact resistance R_c, the external load impedance Z_L, and the effect of the mobile charge. For the reach-through structure, the latter reduced E_m by an amount $\Delta E_m = Iw/(2\epsilon v_h A_i)$, where v_h is the average hole drift velocity in the drift region, and A_i is the illuminated diode area. Since the same field reduction could have been achieved by a voltage reduction $w\Delta E_m$, it is convenient to represent this space-charge effect by an effective space-charge resistance $R_{sc} = w^2/(2\epsilon v_h A_i)$. Thus, we can write

$$\frac{\partial M}{\partial E_m}\frac{dE_m}{dI} = -\frac{\partial M}{\partial V}\left(\frac{R_c + Z_L}{1 + j\omega C_d(R_c + Z_L)} + R_{sc}\right). \qquad [28]$$

R_{sc} is in fact purely resistive for frequencies up to those at which the depletion-layer transit-time becomes a limiting factor, and for most practical purposes can be considered purely resistive at all frequencies. Note that in the equivalent circuit (see Fig. 25) R_{sc} affects the gain, but not the RC time constant of the diode and is, therefore, a current-limiting but not a frequency-limiting element.

The effect of temperature on gain is primarily to change the ionization coefficients and, therefore, the breakdown voltage V_B. To a first

approximation for a particular avalanche diode, one can write

$$M(V,T) = \frac{K}{V_B(T) - V}. \qquad [29]$$

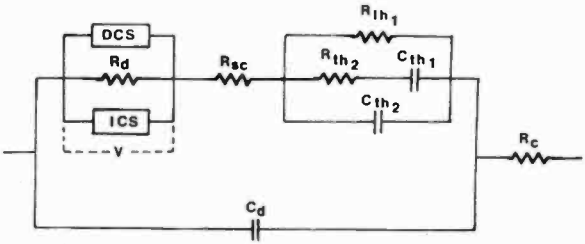

C_d = Diode Capacitance
R_c = Diode Contact Resistance
R_{sc} = Effective Space Charge
$R_d = (dI_{ds}/dV)^{-1}$

R_{th1}, R_{th2}, C_{th1}, C_{th2} are the effective thermal resistances and capacitances, respectively

Fig. 25—Equivalent circuit of avalanche photodiode. ICS is the independent current source $= I_{dso}$, and DCS is the dependent current source $= (P_oR_o + I_{db})M(V)\gamma_e\gamma_h$, where V is the voltage across R_d. As an example, for Type C30817, $R_d \approx 10^{10}$ ohms, $R_{sc} \approx 2 \times 10^3$ ohms, $R_{th1} \approx 1.1 \times 10^4$ ohms, $R_{th2} \approx 12$ ohms, $R_c \approx 10$ ohms, $C_d \approx 2$ pF, $C_{th1} \approx 0.5$ μF, $C_{th2} \approx 0.5$ μF, $I_{dso} \approx 5 \times 10^{-8}$ A, $I_{db} \approx 10^{-10}$ A, and $M(V) \approx 4000/(V_B - V)$, where V_B is the breakdown voltage.

Therefore

$$\frac{\partial M}{\partial T} = \frac{\partial M}{\partial V_B}\frac{\partial V_B}{\partial T} = -\frac{\partial M}{\partial V}\frac{\partial V_B}{\partial T}$$

or

$$\frac{\partial M}{\partial I} = -V\frac{\partial M}{\partial V}\frac{\partial V_B}{\partial T}\frac{\partial T}{\partial P} = -\frac{\partial M}{\partial V}Z_{th} \qquad [30]$$

where $P = VI$ is the power dissipated in the diode, $\partial T/\partial P$ is the diode thermal impedance, and

$$Z_{th} = V\frac{\partial V_B}{\partial T}\frac{\partial T}{\partial P}. \qquad [31]$$

At *very* low frequencies $\partial T/\partial P$ is a pure thermal resistance de-

termined primarily by the insulating substrate on which the diode is mounted, and is given by $\partial T/\partial P = t_s/(K_s A_c)$, where t_s is the substrate thickness, K_s is the substrate thermal conductivity, and A_c is the area of the detector chip, so that at very low frequencies, Z_{th} is purely resistive, with the resistive part given by

$$R_{th} = V \frac{\partial V_B}{\partial T} \frac{t_s}{K_s A_c}. \qquad [32]$$

However, the thermal time constant of the substrate, $c_s t_s^2/K_s$, where c_s is the thermal heat capacity of the substrate, is usually quite long—of the order of milliseconds or more—so that Z_{th} can be considered to be purely resistive only at frequencies of a few Hz or less.

A complete thermal analysis of the diode depends critically on how the diode is mounted and will not be given here. Such an analysis would show, however, the following possible frequency ranges:

[1] $\omega \ll K_s/(c_s t_s^2)$. In this case, discussed above, $dT/dP \approx t_s/(K_s A_c)$.

[2] $K_s/(c_s t_s^2) < \omega < K_s/(c_c t_s t_c)$, where c_c is the thermal heat capacity of the silicon chip and t_c is its thickness. In this frequency range, the chip is more or less all at the same temperature and the substrate acts as a heat reservoir, $dT/dP \approx [t_s/(j\omega c_c t_c K_s A_c^2)]^{1/2}$.

[3] $K_s/(c_c t_s t_c) < \omega < K_c/(c_c t_c^2)$, where K_c is the thermal conductivity of the diode chip (silicon). In this range, the diode is more or less isolated from the substrate, but can still be considered to have a fairly uniform temperature throughout the chip. Thus $dT/dP \approx 1/(j\omega c_c t_c A_c)$.

[4] $K_c/(c_c t_c^2) < \omega < K_c/(c_c t_h^2)$, where t_h is the thickness of the high field region. In this range the temperature change throughout the chip cannot be considered constant, and the change in temperature will be greater in the avalanche region than in the rest of the diode because of the higher power dissipation level in the avalanche region. This frequency range depends critically on the diode structure for a mathematical description.

[5] $K_c/(c_c t_h^2) < \omega$. For all ω's greater than $K_c/(c_c t_h^2)$, the local temperature change depends solely on the local heating rate. In this case, in the avalanche region $\partial T/\partial P = E_m/(j\omega V c_t A_t)$.

For most purposes, these various frequency ranges can be accounted for adequately by the equivalent circuit shown in Fig. 25, where

$$R_{th1} = \frac{\partial V_B}{\partial T}\frac{t_s V}{K_s A_c}$$

$$C_{th1} + C_{th2} = \frac{c_c t_c A_c}{V(\partial V_B/\partial T)} \qquad [33]$$

$$C_{th2} = \frac{c_c A_i}{E_m(\partial V_B/\partial t)}$$

$$R_{th2} = \frac{c_c t_h^2}{K_c C_{th2}}$$

Typical values of these components for the RCA C30817 are: $R_{th1} = 11$ kilohms, $C_{th1} + C_{th2} = 0.5\ \mu$F, $C_{th2} = .015\ \mu$F, $R_{th2} \approx 12$ ohms. Except at very low frequencies, these impedances are small compared to R_{sc}. Thus at all frequencies of normal interest in avalanche photodiodes (> 1 MHz), the thermal effect can be ignored except for the effect of the dc component of the current.

With some slight approximation, it is possible to get a mathematical representation of how the current saturates. Referring to Eqs. [26], [27], [28], and [30] we have

$$\frac{dI}{dI_p} = \frac{M}{1 + I_p \dfrac{dM}{dV}\left(R_{sc} + Z_{th} + \dfrac{R_c + Z_L}{1 + j\omega C_d(R_c + Z_L)}\right)}, \qquad [34]$$

or, since from Eq. [29] $dM/dV \approx M^2/K$,

$$\frac{dI}{dI_p} \approx \frac{II_s}{I_p I_s + I^2} \qquad [35]$$

where

$$I_s = K\left[R_{sc} + Z_{th} + \frac{R_c + Z_L}{1 + j\omega C_d(R_c + Z_L)}\right]^{-1}.$$

Eq. [35] can be integrated to give

$$I = \frac{I_s}{2M_o}\left[\left(1 + \frac{4M_o^2 I_p}{I_s}\right) - 1\right]^{1/2}, \qquad [36]$$

where M_o is the low-current gain. Eq. [36] has two limiting values

$$\left.\begin{aligned} I &= I_p M_o, \qquad |4M_o^2 I_p/I_s| \ll 1 \\ &= (I_s I_p)^{1/2} |4M_o^2 I_p/I_s| \gg 1 \end{aligned}\right\} \qquad [37]$$

Eq. [36] departs from linearity by 10% when $4M_o^2 I_p/I_s = 0.123$. Thus the maximum primary current in the linear range (as defined by $< 10\%$ departure from linearity) is given by

$$I_{p\max} \approx 0.123\, I_s/M_o^2. \qquad [38]$$

Example: In most circuits designed for low noise and good high-frequency response, the effective value of Z_L, because of feedback, is quite low. Thus I_s is normally limited by R_{sc}. For reach-through diodes with $w = 10^{-2}$ cm, $R_{sc} \approx 2 \times 10^3$ ohms and $K \approx 4 \times 10^5 w \approx 4000$. Thus $I_s \approx 2$A and $I_{p\max} \approx 0.25/M_o^2$. At a gain of 100, the diode is linear up to power levels of about $2.5/R$ milliwatts, where R is the responsivity.

B. Transit-Time Effects

The analysis above does not take into account transit-time effects in the diode. The actual current flowing through the external circuit or charging the plates of the diode capacitance is

$$I = \frac{1}{w}\int_0^w (I_h + I_e)\, dx \qquad [39]$$

where I_h and I_e are the hole and electron particle currents.

For the reach-through structure, where most of the depletion layer is the drift region, i.e., $x_2 \ll w$, the frequency dependence of I can be calculated as follows. Let the optical generation rate in the depletion layer be $g(x)$ exp $\{j\omega t\}$. Then, assuming a constant electric field in the drift region, we have

$$I_e(x,t) = \exp(j\omega t) \int_x^w g(x) \exp\{-j\omega x'/v_e\}\, dx' \qquad [40]$$

$$I_e(x_2,t) = I_p \gamma_e \qquad [41]$$

where $I_p = \exp\{j\omega t\} \int_{x_2}^{w} g(x)\,dx$ is the total primary current generated, and γ_e, the electron transit factor, is

$$\gamma_e = \frac{\int_0^w g(x) \exp\{-j\omega(x/v_e)\}\,dx}{\int_0^w g(x)\,dx}. \qquad [42]$$

γ_e has two limiting values of interest. For strongly absorbed light, $\gamma_e = \exp(-j\omega\tau_e)$. In this case all generated electrons enter the high-field region in phase, and γ_e is just a phase factor due to the transit-time delay. For weakly absorbed light,

$$\gamma_e = \exp\left\{-j\frac{\omega\tau_e}{2}\right\} \frac{\sin(\omega\tau_e/2)}{\omega\tau_e/2}.$$

In this case the amplitude as well as the phase of the injected electron current has a frequency dependence.

For the hole current,

$$I_h(x,t) = \exp\{j\omega t\}\left[I_h(0) \exp\left\{-j\omega\frac{\tau}{v_h}\right\} + \int_0^x g(x') \exp\left\{-j\omega\frac{(x-x')}{v_h}\right\} dx' \right], \qquad [43]$$

where $I_h(0) = (M(\omega) - 1)I_e(0)$. Or, for M large,

$$I_h(x,t) \approx I_p\gamma_e \exp\{-j\omega(x/v_h)\}M(\omega). \qquad [44]$$

We thus have

$$I(\omega,t) = \frac{1}{w}\int_0^w (I_h + I_e)\,dx$$

$$\approx \frac{1}{w}\int_0^w I_h dx$$

$$= I_p \gamma_e \gamma_h M(\omega),$$

where $\gamma_h = \exp\{-j\omega\tau_h/2\}\dfrac{\sin \omega\tau_h/2}{\omega\tau_h/2}$.

$M(\omega)$ can be shown to be given by[18]

$$M(\omega) = \frac{M(0)\exp\{-j\omega M\tau_m/2\}}{1 + j\omega M(0)\tau_m},$$

where $M(0)\tau_m$ is the effective multiplication time. Typically, $\tau_m < 10^{-12}$ sec, so that $M(\omega) = M(0)$ up to frequencies such that the gain–bandwidth product approaches 200 GHz. With reach-through diodes at normal gains, this is normally above the frequency limit determined by the transit-time factors.

References:

[1] c.f. L. K. Anderson, M. Di Domenico Jr., and M. B. Fisher, "High Speed Photodetectors for Microwave Demodulation of Light," **Advances in Electronics,** Vol. 5 (1970), Academic Press, Les Young Editor; H. Melchior, M. Fisher, and F. Arams, "Photodetectors for Optical Communications Systems," **Proc. IEEE,** Vol. 58, p. 1466, Oct. 1970.

[2] R. J. McIntyre, "Multiplication Noise In Uniform Avalanche Junctions," **IEEE Trans. Electron Devices,** Vol. ED-13, p. 164 (1966).

[3] C. A. Lee, R. A. Logan, R. L. Batdorf, J. J. Kleimack, and W. Weigmann, "Ionization Rates of Holes and Electrons In Silicon," **Phys. Rev.,** Vol. 134, p. A761, May 4, 1964.

[4] R. J. McIntyre, "The Distribution of Gains in Uniformly Multiplying Avalanche Photodiodes: Theory," **IEEE Trans. Electron Devices,** Vol. ED-19, p. 703, June 1972.

[5] J. Conradi, "Temperature Effects in Silicon Avalanche Diodes," **Solid State Electronics,** Vol. 17, p. 99, Jan. 1974.

[6] S. M. Sze, **Physics of Semiconductor Devices,** J. Wiley and Sons, Inc., N. Y., 1969, p. 678.

[7] J. Conradi, "The Distribution of Gains in Uniformly Multiplying Avalanche Photodiodes: Experimental," **IEEE Trans. Electron Devices,** Vol. ED-19, p. 713, June 1972.

[8] S. D. Personick, "New Results on Avalanche Multiplication Statistics with Applications to Optical Detection," **Bell Syst. Tech. J.,** Vol. 50, p. 167, Jan. 1971.

[9] S. D. Personick, "Statistics of a General Class of Avalanche Detectors with Applications to Optical Communications," **Bell Syst. Tech. J.,** Vol. 50, p. 3075, Dec. 1971.

[10] H. W. Ruegg, "An Optimized Avalanche Photodiode," **IEEE Trans. Electron Devices,** Vol. ED-14, p. 239, 1967.

[11] P. P. Webb, and R. J. McIntyre, "A Silicon Avalanche Photodiode for 1.06 μm Radiation," Solid State Sensors Symposium, Minneapolis, Minn., June 1970.

[12] P. P. Webb, and R. J. McIntyre, "An Efficient Low Noise Avalanche Photodiode for Visible to 1.06 μm," **Proc. Electro-Optical Systems Design Conf.,** 1971 East; p. 51.

[13] G. C. MacFarlane, T. P. McClean, J. E. Quarrington, and V. Roberts, "Fine Structure in the Absorption-Edge Spectrum of Si," **Phys. Rev.,** Vol. 111, p. 1245, 1 Sept. 1958.

[14] A. A. Quaranta, M. Martini, G. Ottaviani, G. Radaelli, and G. Zanarini, "Experimental Results on the Drift Velocity of Hot Carriers in Silicon and Associated Anisotropic Effects," **Solid State Electronics,** Vol. 11, p. 685, 1968.

[15] A. A. Quaranta, C. Canali, and G. Ottaviani, "Hot-Hole Anisotropy in Silicon," **Appl. Phys. Lett.,** Vol. 16, p. 432, June 1970.

[16] C. R. Crowell and S. M. Sze, "Temperature Dependence of Avalanche Multiplication in Semiconductors," **Appl. Phys. Lett.,** Vol. 9, p. 224, Sept. 15, 1966.

[17] P. P. Webb and A. R. Jones, "Large Area Reach-through Avalanche Diodes for Radiation Monitoring," **IEEE Trans. Nucl Sci.,** Vol. NS21, p. 151, Feb. 1974.

[18] R. Kuvas and C. A. Lee, "Quasistatic Approximation for Semiconductor Avalanches," **J. Appl. Phys.,** Vol. 41, p. 1743, March 1970.

Review on High-Power-Laser Damage to Materials II*

A. K. Ghosh

RCA Ltd., Ste. Anne de Bellevue, Canada

Abstract—The paper reviews available information relating to high-power-laser damage to solids. Diverse damage thresholds in metal targets are defined, namely for melting, vaporization, composite effects and plasma shielding. The mechanisms responsible for bulk and surface damage in transparent solids are discussed. The final subsection reviews damage in infrared components such as windows, mirrors and nonlinear devices, mainly at the 10.6 μm wavelength.

1. Introduction

In recent years, intense research and development in obtaining higher and higher output power from lasers have resulted in achieving several hundred kilowatts of cw power from CO_2 lasers.[1] Pulsed CO_2 laser output of GW/cm^2 has also been achieved.[2] Such a high-power beam can cause catastrophic damage to solids. This capability has opened up many applications for infrared laser beams. For instance, the high-power effect of laser beams on metals manifests itself in heating,

* Part I, "Review of Gas-Breakdown Phenomena Induced by High-Power Lasers," by I. P. Shkarofsy appeared in the March 1974 issue of *RCA Review*, p. 48.

melting, and vaporization of the materials, and has found applications for material processing such as cutting, welding, and drilling. Furthermore, because of the damaging aspect of high-power laser effects and the level of power that is being achieved, the CO_2 laser is rapidly approaching the point where its use as a thermal weapon is feasible. Consequently, studies of the vulnerability of military targets to laser thermal weapons are of special interest. Another area of major concern in the development and application of high-power lasers is the behavior of optical materials under intense illuminations. The demands imposed on the optical components, when they are incorporated into a laser system at high power levels, represent a new class of problems. Properties such as weak absorption, minute inhomogenuities, and nonlinear susceptibility, which are insignificant at low power levels, often lead to catastrophic material failure at high power levels. Thus, in the development of high-power lasers, laser-induced damage to windows and mirrors is of great concern. The damage problem is also central to the design and operation of nonlinear devices. For example, with optical parametric oscillators, the interesting regimes of operation are commonly limited by damage problems. In this paper we review various aspects of laser-induced damage in solids with emphasis on CO_2 lasers.

2. Damage in Metal Targets

Laser-induced damage in metals is of particular interest with regard to applications of high-power lasers for material processing and as thermal weapons.

In this section our discussions on damage in metals contains only results available from the open literature, where the main emphasis has been on material processing. Furthermore, most of the data relate to ruby, Nd-glass or Nd-YAG lasers; very few results were obtained with CO_2 lasers. In this paper we discuss those studies on laser-metal interactions where either CO_2 lasers are used or where the importance of laser wavelength is immaterial. It appears that, as Glass and Guenther[3] point out, "we are in a very poor position to draw any conclusions regarding damage at metallic surfaces, other than to assume it is thermal in character. Very little information regarding the morphology of the damage and its dependence on pulse duration and spot size has been obtained and made available to date".

It is generally accepted that the damage in metals by laser radiation is of thermel origin, which involves heating, melting, and vaporization of the metals; the extent of damage depends on the laser power density, the pulsed duration, and the average as well as the peak

power. The heating of a metal by laser radiation without a phase change has been discussed and reviewed by Ready[4] in his book on effects of high power laser radiation. It is not generally considered as damage.

Qualitatively, the laser-metal damage processes go as follows. For a power level of the order of 10^5 W/cm^2 or less and long pulse duration, melting dominates. The melting-flushing of molten metal occurs at normal pulse (not Q-switched) power levels ($\sim 10^7$ W/cm^2) with a pulse duration longer than 100 μsec. As the power density increases, or the pulse duration decreases, vaporization dominates. An extreme case is the Q-switched pulse, which provides extremely high power and very short pulse duration—of the order of 10^9 W/cm^2 and 10 nsec. Fig. 1 shows these sequences from melting to vaporization for various laser pulse lengths and flux density.

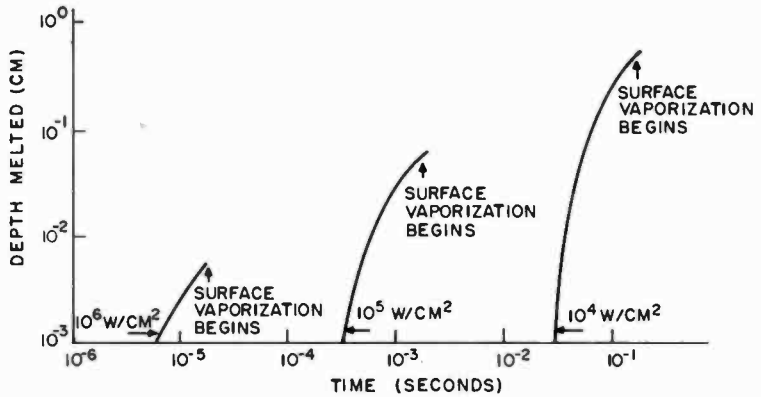

Fig. 1—Melted depth[4] in yellow brass as a function of time for various laser flux densities up to the time that vaporization begins.

Characteristically, however, in most uncontrolled experiments, one finds that laser damage manifests itself with the ejection of both molten metals and vapors and the development of a disintegration zone (a crater).[5-7] Under such a situation, it is very difficult to determine which particular mechanisms influence the material removal. Adams and Hardway[8] hypothesize that most of the material is removed as molten metal. This is confirmed by Anisimov et al[5,6] who find, from a photographic study of the laser-metal interaction, that material is removed in both liquid and vapor form. Chun and Rose[9] also made a

systematic study that agrees with Anisimov et al's conclusion. Shock waves are observed[5] in the vapor plume created at normal pulse power levels, as well as at Q-switched power levels.[10] While shock waves are suggested[11,12] as an important factor in material removal, Chun and Rose's study indicates that they do not play a major role in normal pulsed-laser–metal interaction. Occasionally, as has been reported by Locke et al[13] in their study of deep-penetration welding with a high-power CO_2 laser, a well-concentrated ionization cloud is observed in the laser beam that appears to be fed by the ejected metal vapor. This plasma appears to absorb most of the incident power and, unless blown away, prevents most of the laser radiation from reaching the metal target. The production of plasma is a subject in itself because of its importance in laser fusion studies. This is not discussed in this paper.

2.1 Melting Damage Threshold

Because of numerous complicated processes involved in laser–metal interaction, it is difficult to define a universal damage threshold. Obviously the definition depends on the goal of a given study.

Sneidmiller and Richardson[14] define damage as the transport of material and/or changes in microstructures as a result of melting. This may therefore be referred to as a melting damage threshold. Following their approach, the threshold for melting damage is influenced by factors that affect absorption and temperature rise, namely reflectance, absorption coefficient, heat capacity, thermal conductivity, and melting point. They define a threshold parameter

$$D_o = \frac{1 - R}{(T_m - T_o)\sqrt{K\rho c_p}}, \qquad [1]$$

where T_m is the melting point, T_o is the initial temperature, K is the thermal conductivity, ρ is the density, c_p is the specific heat, and R is the reflectance. This quantity D_o is referred to as the melting damage parameter for opaque materials, since the higher its value, the more susceptible the material is to laser damage. Schneidmiller and Richardson[14] made some laser damage studies using a ruby laser (30 J, 1.5 msec) to check the validity of the damage-parameter definition. Their results are shown in Table 1 for various materials in order of their decreasing damage site volume. This order, with a few notable exceptions, is the same as that of the D_o values. Room-temperature physical properties are used to calculate D_o. Silicon appears higher in the table than one would expect on the basis of D_o. The damage

site, however, appears to have resulted from spallation due to thermal shock rather than melting, thereby yielding an anomalously large damage site volume.

Table 1—Materials in Order of Decreasing Damage Site Volume Compared with Melting Damage Parameter[14]

Material	Beam Energy Density (cal cm^{-2})	Damage Site Volume (mm^3)	Melting Damage Parameter ($D_* \times 10^{-3}$)
Lead	2456	4.5	6.93
Bismuth	474	1.6	16.45
Tin	498	1.2	3.70
Boron	2419	1.1	7.40
Silicon	2456	1.0	1.64
TiC-C Alloy	1216	0.85	—
Titanium	2006	0.30	2.58
Iron (High carbon steel)	1824	0.25	—
Silicon Carbide[d]	2419	0.23	3.52
Aluminum 6061-T6	1884	0.18	—
Iron Alloy (Armco)	2043	0.09	—
Aluminum	2626	0.08	0.480
Pyrolytic Graphite [a,d]	2000	0.08	0.425
Iron	1714	0.05	0.812
Aluminum Oxide	2480	0.02[c]	—
Pyrolytic Graphite[b]	1216	0.01	5.00
Molybdenum	2176	0.002	0.392
Tantalum	2444	—	0.392
Tungsten	2614	—	0.255
Copper	2833	—	0.023
Silver	2079	—	0.022

[a] Beam perpendicular ($\perp$) to the c-axis
[b] Beam parallel ($\parallel$) to the c-axis
[c] Total of all damage site volumes
[d] The lens system used in these two experiments was different from that used in other experiments

Another way of defining the melting damage threshold is with respect to maximum depth melted without vaporization. In order to do that the heat flow equation must be solved in both molten and solid regions with the conservation of energy at the moving boundary, namely

$$K_2 \frac{\partial T_2}{\partial z} - K_1 \frac{\partial T_1}{\partial z} = L_f \rho \frac{dZ(T)}{dt} \qquad [2]$$

where $Z(t)$ is the position of the boundary at time t, L_f the latent heat of fusion per unit mass, and the subscripts 1 and 2 refer to the liquid and solid regions, respectively. At the boundary, the temperature equals the melting point (T_m). At the surface, we have the boundary condition

Table 2—Parameters for Calculation of Depth Melted[4]

Metal	Ratio of heat of fusion to heat content at melting point	G(W/cm) (maximum depth melted × laser flux density)
Cu	0.515	7650
Fe	0.400	1100
Ni	0.491	2070
Ta	0.407	2460
W	0.406	4650

$$-K\,\partial T/\partial z = I(t)\,;\ z = 0, \qquad [3]$$

where $I(t)$ is the absorbed laser flux density. Fig. 2 shows the results of the analog computer solutions of the problem, adapted from Cohen.[15] The laser flux density threshold for melting the metal to a maximum depth Z_{max} without surface vaporization may be expressed

$$I = G/Z_{max}, \qquad [4]$$

where G is a numerical factor characteristic of the metal. The values of G for ruby radiation are given by Ready[4] and are shown in Table 2 as deduced from Fig. 2.

Gonsalves and Duley,[16] following Asmus and Baker,[17] present results of a quantitative investigation on the dependence of the critical incident power (designated as P_m) for the production of melting on a,

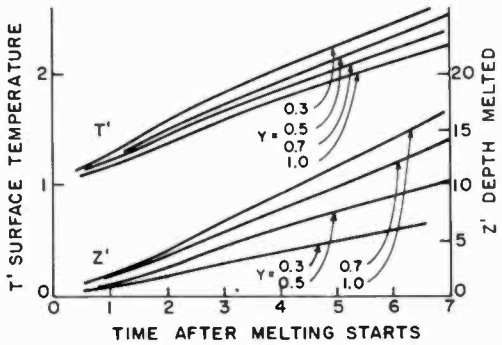

Fig. 2—Generalized analog computer solutions[4] for laser melting. Here, respectively, temperature is normalized to T_m, time to $t_m = \pi T_m^2 (K\rho c_p)_2/(4I^2)$ and depth melted to $3\pi T_m^2 (c_p K)_2/(100 L_f I)$. Also $Y = L_f/(T_m c_{p2})$, where subscript 2 refers to the solid. For calculated values of t_m, Y, and $T_v' = T_v/T_m$, determine $\tau_v = t_v/T_m$ from the top set of curves. The depth melted for $t_m < t < t_r$ is then found from the lower curves.

the radius of the focused spot on the target, and on t_m, the time for melting to occur after the onset of target heating. They direct a cw CO_2 laser with power levels of 10^4-10^6 W/cm^2 at a 302 stainless-steel target. These results are then generalized to provide predictions of P_m for various metals and thicknesses. The results are shown in Figs. 3 and 4.

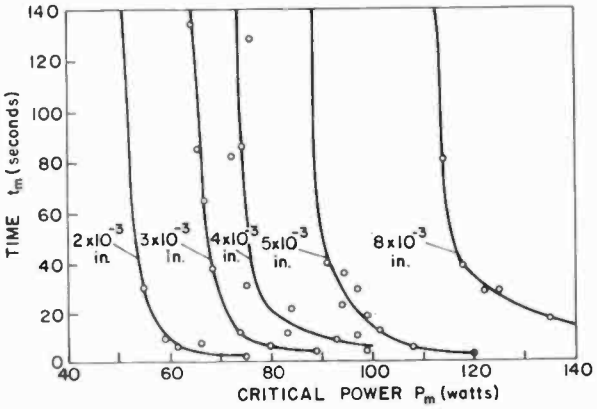

Fig. 3—Critical power P_m for melting[16] versus t_m for several thicknesses of type 302 stainless steel in air. The hole radius for these curves is 0.04 cm.

2.2 Vaporization Threshold

The situation of optimum melting without vaporization occurs only over a very narrow range of laser parameters. In fact, in most experiments, vaporization seems to occur unless one is very careful. At the same time, true vaporization removal is also very uncommon. The experimental results indicate that much of the material is removed in liquid state rather than vaporized state. However, Ready[18] and also Anisimov et al[5,19] develop a quasi-stationary theory for a one-dimensional true vaporization of metals by laser radiation obtained in free-running modes. Ready[18] uses Landau's[20] treatment of a continually vaporizing surface with constant heat input at the surface and continual removal of vaporized material from the surface. He shows that the time (τ_v) to reach the vaporizing temperature (T_v) is given by

$$\tau_v = \frac{\pi}{4}\frac{K\rho c_p}{I^2}(T_v - T_o)^2 \qquad [5]$$

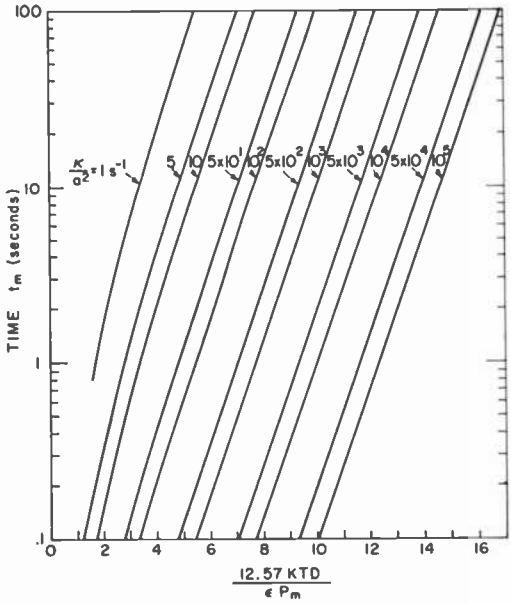

Fig. 4—Theoretical curves[16] for the prediction of P_m or t_m for thin metal sheets, if the thickness $D \leqslant \sqrt{\kappa t_m}$.

Table 3 shows the value of τ_v for various mtals and laser flux densities.

The rate of removal of material will reach a steady-state rate given by

$$\frac{dZ}{dt} \equiv v_{ss} = \frac{I}{\rho[L_v + c_p(T_v - T_o)]} \qquad [6]$$

Table 3—Time to Reach Vaporization Temperature,[4] τ_v

Metal	Laser flux density (W cm^{-2})			
	10^4	10^5	10^6	10^7
Bi	2.460 msec	24.6 μsec	0.246 μs	
Cd	8.970	89.7	0.897	
Pb	11.770	117.7	1.177	
Zn	12.770	127.7	1.277	
Mg		245.1	2.451	
Sn		599.8	5.998	0.060 μs
Ni		1.842 msec	18.415	0.184
Fe		1.855	18.550	0.186
Al		2.666	26.66	0.267
Mo		5.557	55.57	0.556
Cu		8.26	82.60	0.826
W		10.46	104.61	1.046

The depth of vaporization, Z, may be expressed as a function of time in units of τ_v. This implicitly assumes a temporally flat pulse. If, however, the value of τ_v is very short compared to the time scale over which the power in the laser pulse varies, the speed of the moving boundary between vapor and solid will adjust itself to the steady-state speed associated with the flux at any instant of time. The depth of evaporation may be calculated by integrating Eq. [6] for the instantaneous value of evaporation velocity, from τ_v to the end of the pulse.

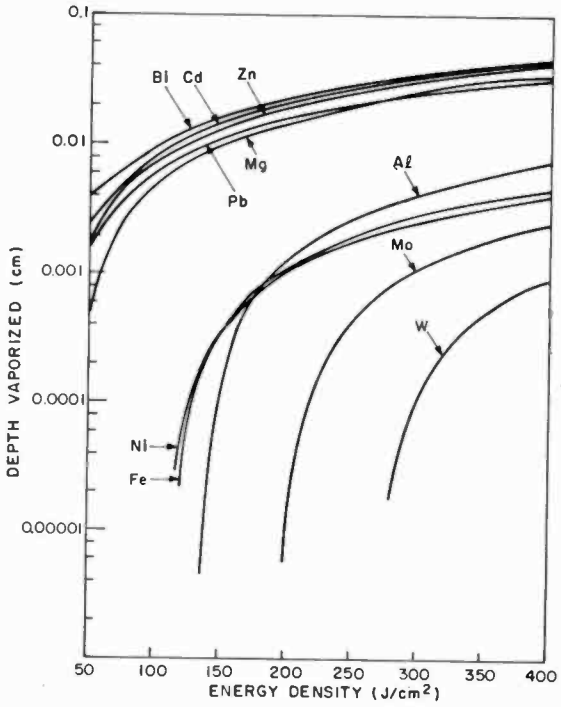

Fig. 5—Calculated depth,[4] hole vaporized by a 0.7 ms duration laser pulse, as a function of absorbed energy per unit area for various metals.

This will give the amount of material removed as a function of total energy in the pulse when a specific pulse shape is assumed. Figs. 5 and 6 show the calculated results for comparison with the experimental results shown in Fig. 7. The discrepancies for high-melting-point metals indicate that the reflectivity of the metals and the expulsion of molten metals are important.

A point of difference between the studies of Ready and Anisimov

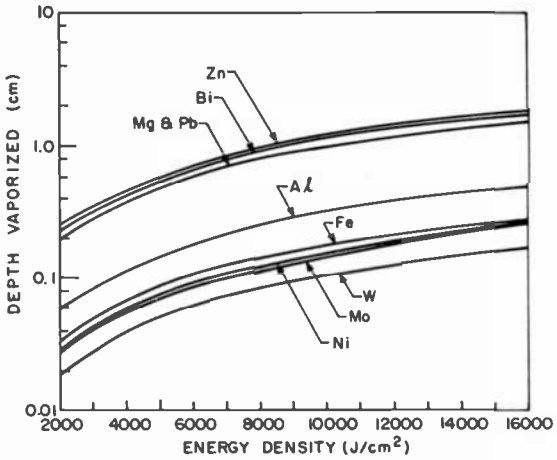

Fig. 6—Same as in Fig. 5, but at higher energies per unit area.

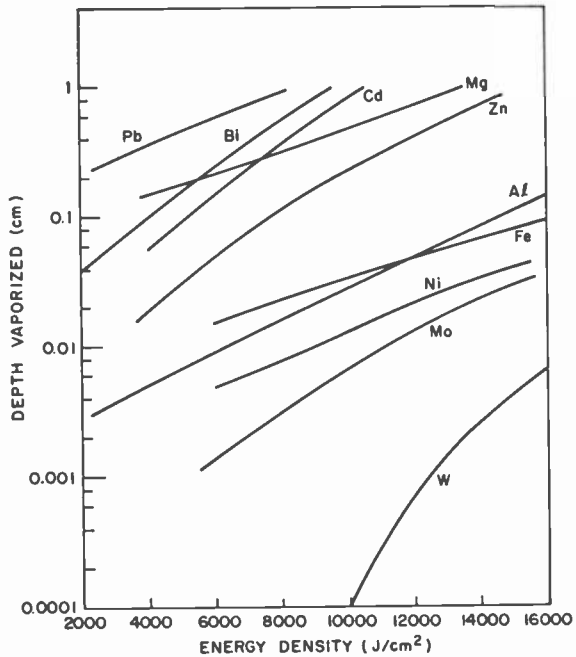

Fig. 7—Experimental depth[4] vaporized for various metals irradiated by a Nd glass laser with a 0.7 ms pulse having 15 J. (Measurements by Braginskii et al, *Sov. Phys. Tech. Phys.*, Vol. 12, p. 753, 1967.)

is that in Anisimov et al's approach the temperature (T_v^*) of the moving boundary between vapor and solid interface is taken to be higher than T_v at high flux densities ($\geqq 10^8$ W/cm^2). The rationale for this is that T_v^* depends on the radiation flux density I and is determined to ensure conservation of energy. This treatment is only applicable for a very high peak power. Moreover, according to Ready,[4] the equation for evaporation kinetics is sufficiently inexact that any deviation from the results derived using T_v is not meaningful, at least in the range of flux density below 10^8 W/cm^2.

Afanasev and Krokhin[21] have used a different approach, namely a gas dynamic approach. However, both the one-dimensional approach and the gas dynamic approach yield the same results at flux densities below 10^9-10^{10} W/cm^2.

2.3 Composite Threshold

As is mentioned above, any treatment considering only a two phase breakdown scheme, i.e., solid–vapor interface, without melting taken into account, does not give the true picture. Ulyakov[22] uses similitude theory to describe the breakdown of solids by a laser beam. It is noted that the surface evaporation dominates in the initial stage of the process until a sufficiently deep crater is formed. Once a cavity is formed in the material, the surface evaporation is replaced by melting and flushing out of the material. Leech[23] recently modeled the thermodynamic behavior of the target material and used it to predict the damage volume of Al, Be, Fe and uranium targets irradiated by a single pulse.

The possibility of explosion-like boiling is considered by Ready[24] and also by Dabby and Paek[25] and others.[26] Dabby and Paek define a parameter

$$B = \frac{KbL_v}{Ic_p} \qquad [7]$$

where K is the thermal conductivity, b is the absorption coefficient, L is the heat of vaporization, I is the laser intensity, and c_p is the specific heat. This parameter has special significance since it may be used to predict the relative strength of an expulsion for certain laser–material interactions. Recently, Gagliano and Paek[27] report some results in qualitative agreement with the theory.

Komotoskii[28] also defines his damage threshold in terms of the intensity level above which the energy absorption mechanism changes

from basically evaporation to explosive destruction and ejection. This threshold is taken to be of the order of 10^8 W/cm^2. The criterion for transition is taken in terms of a characteristic dimension of the evaporation region as a function of relative incident intensity P/P_t, where P_t is the evaporation threshold.

Zhiryakov et al[29] define their damage threshold to be where ejection in the form of liquid droplets begins to occur. Fig. 8 shows the ejected mass as a function of beam intensity for various targets. The study indicates a strong dependence on the purity of the target.

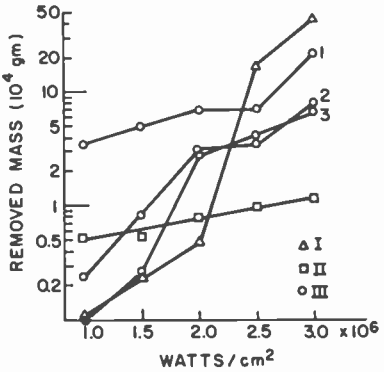

Fig. 8—Relation[29] between removed mass upon damage from various metals as a function of laser beam intensity with a 2-6 μs pulse: I-Zr; II-Cr; III-Cu; 1, crude Cu; 2, anode Cu; 3, cathode Cu.

2.4 Plasma Shielding Threshold

The laser-metal interaction often involves the formation of an ionized layer in front of the target that tends to shield the incident radiation. Andreev et al[30] define a plasma-formation threshold. Threshold energy density is shown to be that level required to ionize a layer of material to a depth of $1/\alpha$, where α is the laser-beam absorption coefficient in the evaporated region. Table 4 gives a summary of test and calculated data for various metals using Nd laser radiation.

Levinson and Smilga[31] also carried out an experimental study of damage threshold in metal films subjected to laser radiation.

Fig. 9 shows results of calculated breakdown threshold versus film thickness using a focused N_2 laser.

Various other studies worth mentioning are as follows:

(1) M. A. Yelyashevich, V. K. Goncharov, L. Ya Min'ko, and G. S.

Table 4—Laser Breakdown Threshold in Metals[30]

Material	Calculated threshold J/cm²	Experimental threshold, J/cm²			Refl., R	$\frac{1}{\alpha} \times 10^{-6}$ cm	
		Detectable plasma glow	Plasma Opacity	Filmed signal		$T = 273°K$	$T = T_{vap}$
Ag	0.20	0.20	0.18	0.24	0.33	1.15	5.05
Al	0.19	0.16	0.23	0.12	0.30	0.9	4.0
C	—	0.82	1.10	1.20	0.02	—	—
Cu	0.38	0.26	0,44	0.40	0.25	1.3	5.6
Mo	0.81	0.74	0.79	0.79	0.20	1.25	7.4
Ni	0.67	0.17	0.27	0.31	0.35	1.5	7.7
Pb	0.06	0.04	0.06	0.04	0.25	1.35	4.1
Pd	0.40	0.29	0.37	0.24	0.27	1.6	6.7
Pt	0.52	0.58	0.76	0.82	0.30	1.35	6.4
Rh	0.62	0.30	0.59	0.66	0.35	1.1	6.0
Ta	1.00	0.30	0.18	0.16	0.31	1.7	8.8

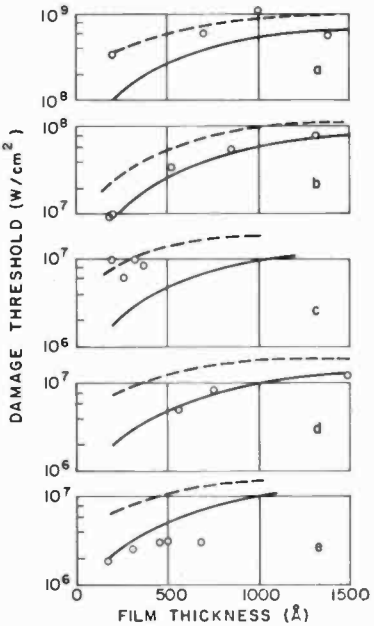

Fig. 9—Damage threshold[31] using a nitrogen laser (0.337 μ) pulse for metallic thin films versus thickness: (a) Ag, (b) Al, (c) Cr, (d) Au, and (e) Cu. Dashed curve includes effect of heat loss in the substrate.

Romanov, "Study of the physical state of destruction products from laser interaction with condensed media," *ZhPS* **15**, No. 2, p. 200, 1971.—A focussed Nd-glass laser was used at energies up to 60 J. Metals studied were W, Li, Al, Cu, Fe, Pb, Zn and brass. The intensity was restricted to 10^8 W/cm^2, so that only thermal destruction occurred.

(2) Yu. K. Krylov and S. A. Volkov, "Optical scatter in products formed by material evaporation by intense electromagnetic radiation." *OiS* **30** No. 3, 517 (1971).—Theoretical and experimental treatments are given to the absorption and reflection from the vapor region generated by laser (Nd glass) radiation directed onto metal targets. For the metals tested (Pb, Al, Cu and Fe), the intensity just before the start of strong attenuation of the probing beam (He-Ne) was in the range $8 \times 10^5 - 3 \times 10^6$ W/cm^2.

(3) N. N. Rykalin and A. A. Uglov, "Internal vaporization from interaction of a laser beam with metals," *TVT*, No. 3, p. 575 (1971).—The effect of internal vaporization and destruction of opaque materials by a laser beam at power densities $>10^6$ W/cm^2 are discussed. The resulting nucleation and growth of bubbles in molten metals are examined from the standpoint of statistical thermodynamic equilibrium of vapour bubbles within the liquid volume.

(4) V. K. Goncharov and L. Ya Min'ko, "Formation of successive shock waves by interaction of a controlled laser emission with absorbing material," *ZhPMTF*, No. 3, p. 98 (1971).—A beam-target experiment is described in which a controlled laser emission is selected to produce shock waves and to study their formation and propagation in absorbing materials (65-59 brass). Spectroscopic studies indicate that shock waves are formed in the material vaporized by the proceeding pulse. Again a Nd-glass laser is used.

It is evident that in the study of laser-metal interaction very little work has been done using CO_2 lasers. Gonsalves and Duley provide a very useful nomogram (Fig. 4) for CO_2 laser-metal interaction for determining the melting threshold. Locke et al study deep-penetration welding using a CO_2 laser; their data of laser cutting and welding will be given in a following paper (part III) on industrial applications of high-power laser beams.* These data are indicative of the degree of damage possible with CO_2 lasers.

In this section an attempt is only made to touch on the key papers involving laser-metal interaction. It appears that the study on laser-metal interaction is far from complete. The data on CO_2 laser-metal

* To appear in future issue of *RCA Review*.

interaction is very meager. Systematic studies on the damaging processes will therefore be very worthwhile using high-power CO_2 lasers.

3. Laser Damage in Transparent Solids

The requirements for new performance criteria on optical materials prompted the American Society for Testing and Materials (ASTM) to establish a subcommittee on lasers and laser materials. Since 1969 there has been an annual symposium on Damage in Laser Materials.[32-35] However, a great majority of the studies reported in these symposia (until 1971) are related to the improvement of host materials for optically pumped lasers, especially ruby and glass. In these systems, the laser material itself is the source of concern. In the 1972 symposium, the emphasis has been on the windows and mirror materials, not only for ruby and glass lasers but also for CO_2 lasers. In this review, we are concerned as far as possible with the basic understanding of the damage mechanisms, with emphasis on CO_2 laser-induced damage. An excellent status report based on the ASTM-NBS symposia has been published by Glass and Guenther.[36]

Some very early works[37,38] on laser damage showed the types of damage that can occur in many materials that are transparent at low power levels. A very striking phenomenon is the production of long narrow damage regions extending in the direction of the beam. It is believed that such damage is associated with the phenomenon of self-focusing (or self-trapping) of the beam. Much work has simply involved examining the damage in detail.[38-41] Most of the works up to 1969 have been reviewed by Ready[4] in his book "Effects of High Power Laser Radiation" (Chap. 6).

Basically two types of damage are encountered in transparent solids: (1) bulk damage and (2) surface damage. In general, there is a difference between the damage threshold at the surface and that in the interior of the sample. Damage induced in the internal volume of the material, i.e., bulk damage, arises from several possible causes. If the material contains minute inhomogeneities due to particulate inclusions, especially metallic inclusions, they can absorb the laser radiation, giving rise to local heating and melting of the surrounding material. This in turn can cause sufficient stress concentrations to rupture the material. A material can also be damaged internally due to self-focusing of the radiation. This occurs because the high electric field associated with the laser beam increases the index of refraction of the material. This causes the beam to converge to an extremely intense focus, after it has propagated a certain distance. If the path

in the material is sufficiently long, the local electric field strength in the light beam is sufficiently intense to cause electron avalanche breakdown, resulting in plasma formation. Electron avalanche breakdown can also occur in the absence of self-focusing, but the threshold is extremely high. Yet another mechanism of breakdown that has been suggested involves production of coherent hypersonic phonons in a stimulated Brillouin-scattering process. Hypersound, due to the direct interaction of laser light with the lattice, then causes mechanical damage.

3.1 Particulate Inclusion

Many laser optical materials exhibit minute inhomogeneities due to particulate inclusions that generally form in the process of fabricating the materials. Theoretical treatments of the problem of stress formation in the vicinity of an absorbing particle have been published.[42-44]

Following Bliss,[44] during a pulse duration τ_p and for an inclusion of radius R such that $R^2/\tau_p \gg D_i > D_h$, where D_i and D_h are the thermal diffusivity of the inclusion and host matrix, respectively, the inclusion surface is heated to a depth of roughly $(D_i\tau_p)^{1/2}$. The laser energy density I required to produce a damaging stress S in the material at the surface of the inclusion due to expansion of the heated outer shell is

$$I = \frac{\tau_p^{1/2} C_i K_h D_i^{1/2} S}{\alpha_i' e_\lambda M} \qquad [8]$$

where C is the heat capacity per unit volume, K_h is the volume compressibility, α' is the volume expansion coefficient, e_λ is the spectral emissivity, and M is a factor to account for a correction due to subwavelength inclusion. Its value is unity for $R \geq \lambda/20$ and $20\ R/\lambda$ for $R < \lambda/20$. Depending on the relative values of D_i and D_h, there is a range of pulse length and inclusion size ($D_i > R^2/\tau_p \gg D_h$) for which the heating is essentially limited to the inclusion during τ_p, and conduction into the host matrix is negligible. Under such a condition, the threshold for damage due to stress from expansion of the inclusion is

$$I \approx \frac{4 C_i K_h S R}{3 \alpha_i' e_\lambda M} \qquad [9]$$

For long pulses or very small inclusions, $D_i > D_h \gg R^2/\tau_p$, a consider-

able volume of the host material is heated during τ_p. Treating the inclusion as a continuous spherical surface generating heat at a constant rate during the pulse, the minimum energy required to cause damage is found to be of the order of

$$I \approx \frac{10 C_h K_h D_h S}{\alpha_h' e_\lambda M} \frac{\tau_p}{R} \qquad [10]$$

Eq. [8] to [10] give the dependence of the damage threshold on inclusion radius and pulse duration for three limiting cases.

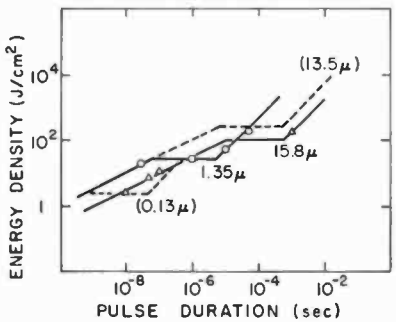

Fig. 10—Threshold for damage[44] due to absorption by Pt inclusion in glass. The pulse duration and inclusion radius dependence of Eqs. (8)-(10) have been fitted to data from P. V. Avizonis and T. Farrington, *Appl. Phys. Lett.*, Vol. 7, p. 205 (1965), indicated by △, for glass known to contain Pt inclusions; and data from C. G. Young and R. F. Woodcock in "Damage in Laser Glass," A. J. Glass et al, editors, ASTM STP 469 (1969), indicated by 0, for glass presumed to contain Pt inclusions. The resulting inclusion sized R giving the best fit are indicated. The dashed curves and R Values in parenthesis illustrate the theoretical dependence on R for the glass in the work of Young and Woodcock.

Fig. 10 shows the threshold for damage due to absorption by platinum inclusion in glass. At the 1972 Damage Symposium, Isumatani et al[45] reported values for damage thresholds by 1.06 μm radiation in glass melted in crucibles of Pt, ceramic, and clay materials. The damage thresholds observed were 15 J/cm² for Pt-melted glass and 120-150 J/cm² for the other two cases. In the absence of particulate inclusions, the exhibited threshold is of the order of 400-500 J/cm².

3.2 Self Focusing

In any transparent dielectric medium, the refractive index exhibits a weak dependence on the local intensity of the transmitted light. This dependence can be written as[46]

$$n = n_o + n_2|E|^2, \qquad [11]$$

where $|E|^2$ is the time-averaged square of the local optical field. Such a dependence leads to the formation of intense self-focusing in the medium. The coefficient n_2 (in units of $|E|^{-2}$ or m^2/V^2) is generally positive. For a given value of n_2, two parameters characterize the tendency of the medium to exhibit self-trapping. One is the critical power for self-focusing, which is that power level in a collimated Gaussian beam that just compensates for the diffraction spreading. The other is the focusing length. Following Akhmanov et al,[47] the critical power is expressed as

$$P_{cr} = \frac{\epsilon_o \lambda^2 c}{8\pi n_2} \qquad [12]$$

where ϵ_o is the permittivity of free space, λ is the wavelength, and c is the velocity of light.

Marburger[48] gives an approximate expression for the self-focusing length as

$$Z_f = \frac{0.369ka^2}{\left(\frac{P}{P_2}\right)^{1/2} - 0.858} \qquad [13]$$

where a is the Gaussian radius of the intensity profile of the beam, $k = 2\pi/\lambda$ and

$$P_2 = \frac{0.0464\pi\lambda^2\epsilon_o c}{n_2}. \qquad [14]$$

This equation is applicable only for $P/P_2 > 1$. Electrostriction[49] is a likely mechanism for self-focusing in transparent dielectric under Q-switched and long pulse duration.

It is seen from Eq. [13] that the self-focusing length is inversely

proportional to the square root of the total laser power. In a pulse, therefore, the focal length will decrease in time as the pulse power rises and then will increase to infinity as the pulse falls. This leads to a moving focus condition. Giuliano[50] demonstrated this effect in an elegant experiment.

It is generally recognized that self-focusing cannot lead to catastrophic damage below the critical power. Fraden and Yablonovitch[51,52] calculate the self-focusing parameter in NaCl and RbI for 10.6 μm (CO_2 laser), 1.06 μm (Nd-YAG) and 0.694 μm (ruby) wavelengths. Results are shown in Table 5.

Table 5—Calculated[51] Steady-State, Self-Focusing Parameters and Experimental Values of Pulse Width (τ_p) and Peak Power

	Wavelength (μm)	τ (10^{-9} sec)	τ_p (10^{-9} sec)	$n_2 \times 10^{22}$ (mks)	P_{cr} (10^3 watts)	P_c (10^3 watts)	P_{probe} (10^3 watts)
NaCl	10.6	11.0	200	2.3	48,000	175,000	120
	1.06	5.3	4.7		480	1,750	37.8
	0.69	3.94	14		204	746	20
RbI	10.6	22.3	200	8.4	13,200	50,000	20
	1.06	10.7	4.7		132	500	6.1
	0.69	8.0	14		56	203	—

For $P_{probe} < P_c$ catastropic self-focusing will not occur.

$P_c = 3.66\ P_{cr}$, where P_{cr} is given by Eq. [12].

P_{probe} is the experimentally measured power for self-focusing.

τ is the electrostrictive response time equal to the ratio of the beam radius to the sound velocity.

3.3 Electron Avalanche Breakdown

As was mentioned, self-focusing by itself is not a damage phenomenon. The reason for material breakdown is the subsequent electron avalanche process due to the intense electric field at the self-focus. Even in absence of self-focusing, an intense laser beam when focused into a transparent dielectric with a short focal length lens will lead to breakdown by the intense optical field at the focus. This is similar to the phenomenon of dc breakdown of dielectrics. Electron avalanche breakdown occurs when free electrons absorbing laser radiation are accelerated sufficiently in the electric field to produce ionizing collisions so that more free electrons are produced. Sources suggested for the initial electrons to start the avalanche include multiphoton absorption[53] and intraband optical absorption.[54] If the rate of electron production from ionization exceeds the electron loss by diffusion, trapping, and recombination, the avalanche starts, eventually leading to a strongly absorbing plasma. Material damage occurs in the vicinity of the plasma.

Bass and Barret[55] discuss a different approach in which they modify to optical frequencies Shockley's[56] avalanche dc breakdown theory. Fraden and co-workers[51] study bulk damage in alkali-halide crystals at 10.6 μm, 1.06 μm, and 0.694 μm in a carefully performed experiment to eliminate the self-focusing effect. Comparison of their results at 10.6 μm and at dc indicates that the process of ac avalanche breakdown, similar in fundamental character to dc avalanche breakdown, is responsible for the damage observed. Their results are summarized in Tables 6 and 7.

Table 6—Absolute Breakdown Strength of NaCl[51]

E_{peak} (dc)	1.50×10^6 V/cm	
E_{rms} (10.6 μm)	1.95×10^6 V/cm	± 10 Percent
E_{rms} (1.06 μm)	2.3×10^6 V/cm	± 20 Percent
E_{rms} (0.69 μm)*	2.2×10^6 V/cm	± 20 Percent

* Gaussian profile assumed.

Table 7—Relative Breakdown Fields[51] (normalized to $E_{NaCl} \approx 2 \times 10^6$ V/cm

	NaI	NaBr	NaCl	NaF
DC	0.460	0.553	1	1.60
10.6 μm	0.405	0.476	1	——
1.06 μm	(0.293)*	0.675	1	1.78
	KI	KBr	KCl	KF
DC	0.380	0.460	0.667	1.27
10.6 μm	0.369	0.482	0.713	1.23
1.06 μm	0.272	0.375	0.568	——
	RbI	RbBr	RbCl	
DC	0.327	0.387	0.553	
10.6 μm	0.323	0.400	0.472	
1.06 μm	0.400	0.550	0.670	

* Crystal was extremely hydroscopic and no final check was made with the microscope to determine if inclusions were responsible for the damage observed.

3.4 Stimulated Brillouin Scattering

A series of experiments[57-59] have been carried out to support the contention that laser-induced damage in transparent solids is due to stimulated Brillouin scattering. Stimulated Brillouin scattering (SBS) results[60] from an internal feedback mechanism that amplifies an acoustic wave (ω_a, k_a) and a secondary electromagnetic wave (ω_s, k_s) at the expense of an input laser beam (ω_1, k_1). The first step in the feedback process occurs when some of the laser light undergoes Bragg diffraction from an acoustic wave in the medium. Through the process

of electrostriction, the diffracted light and the incident laser light then interact to produce an acoustic wave at their difference frequency. When this acoustic wave corresponds to the original acoustic wave, a feedback loop is set up that converts part of the laser energy into acoustic energy. At high enough power levels, damage may occur from the mechanical stress associated with the acoustic wave.[61] The laser energy density for the generation of acoustic power P_{da} that will lead to damage in the material is given by[62]

$$I \propto \left[\ln\left(\frac{BP_{da}}{\tau_p} \right) \right], \qquad [15]$$

where B depends on the material and laser frequency and τ_p is the laser pulse duration. The equation holds for a pulse that is too short to establish a steady-state SBS.[63] For a long pulse, for which steady-state SBS is achieved, $I \propto \tau_p$. At an intermediate pulse length, the laser energy density required for damage is independent of τ_p. The τ_p dependence of the threshold for damage by SBS is shown in Fig. 11.

The mechanism of damage by SBS appears to explain qualitatively some data on damage of transparent materials. However, the general

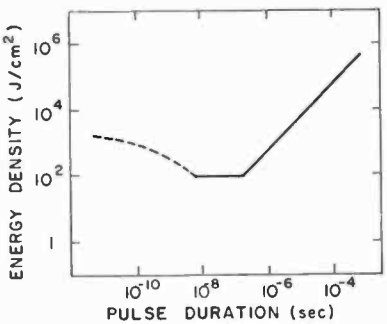

Fig. 11—Predicted pulse duration dependence of the threshold for damage[44] due to stimulated Brillouin scattering. The energy scale is estimated from quartz and glass data in A. I. Ritus and A. A. Manenkov, *JETP Lett.*, Vol. 6, p. 349 (1967) (Ref 58), and from quartz calculations in R. Y. Chiao et al, *Phys. Rev. Lett.*, Vol. 12, p. 592 (1964) (Ref. 61). The time scale is estimated from quartz data in J. Walder and C. L. Tang, *Phys. Rev.*, Vol. 155, p. 318 (1967). The exact form of the dashed part of the curve cannot be determined without knowing B in Eq. [15].

opinion is that although SBS does influence the damage, it may not be the only mechanism.[64] For example, the observations[58] that sometimes SBS occurs without damage while sometimes damage occurs at a threshold below that required for SBS scattering are suggestive. Table 8 shows[4] the threshold values for the SBS process and the actual volume damage threshold.

Table 8—Threshold Values[4] of Q-Switched Ruby Laser

Material	Stimulated Brillouin scattering (W/cm^2)	Volume damage (W/cm^2)
Glass	1.09×10^{10}	0.89×10^{10}
Fused quartz	1.11×10^{10}	1.45×10^{10}
Crystalline quartz (light along z axis)	0.89×10^{10}	3.10×10^{10} (1.95×10^{10}-surface damage)

3.5 Damage at Surfaces

The occurrence of laser-induced surface damage is known to be accompanied by a bright flash of light that comes from a spark or plasma at the surface.[65-68] In fact, the occurrence of a visible spark has been considered to be a criterion for surface damage. Fersman and Khazov[67] suggested that the surface damage is caused by plasma–surface interaction. Damage occurs both at the entrance (front) and exit (back) surfaces, but to a different extent. The difference is explained using a model in which both plasmas on the two sides grow away from the material as they develop in time. In addition, Fersman and Khazov observed a compressional wave that propagated inwardly from the exit surface. Compressional waves have also been observed by others.[53,69] Recently Giuliano[68] performed some experiments using Q-switched ruby laser in an attempt to determine more clearly the connection between the surface damage and the plasma formation. His conclusion was that the surface plasmas are a result rather than the cause of the surface damage. Two kinds of plasmas occur at the entrance surface—one that is sustained by the light beam in the ambient atmosphere, and another that arises from a micro-explosion at or near the surface. The exit surface plasma and spalling is of the explosion type.

The damage at the exit surface occurs at a lower power level than the entrance surface damage threshold. Fig. 12 and 13 show exit and entrance damage threshold in sapphire with a ruby laser. Boling et al[70] propose that this is due to the effect of Fresnel reflection. At normal incidence to a dielectric surface, part of the incident light is reflected and part is transmitted as determined by the Fresnel relations. At the entrance surface, the reflected wave is 180° out of phase with the

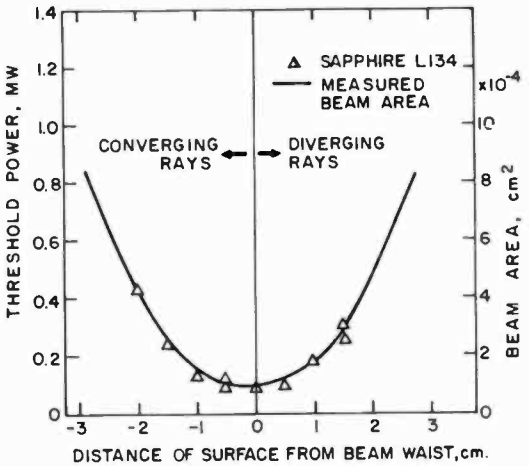

Fig. 12—Exit surface damage threshold power[72] for sapphire sample as a function of surface distance from beam waist for 19-cm lens. Beam area is also plotted.

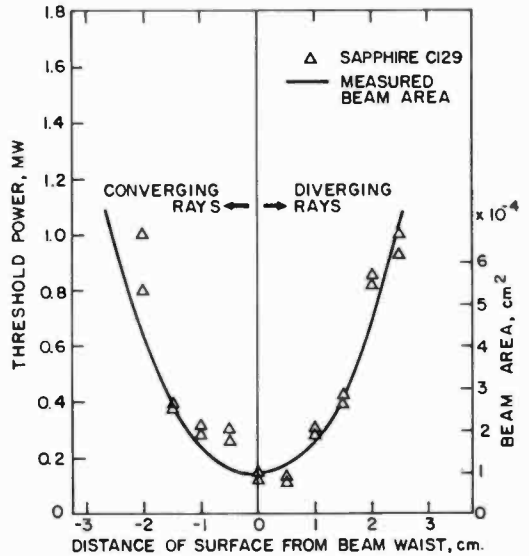

Fig. 13—Beam area[72] and entrance surface damage threshold as a function of surface distance from beam waist for 19-cm lens.

incident light and the transmitted intensity is related to the incident intensity (I_o) by

$$I_{ent} = \frac{4I_o}{(n+1)^2}, \qquad [16]$$

where n is the refractive index of the material. At the exit surface the reflected wave suffers no phase shift and the intensity at the exit surface is given by

$$I_{exit} = \left[\frac{4n}{(n+1)^2}\right]^2 I_o. \qquad [17]$$

Thus

$$I_{exit}/I_{ent} = \left[\frac{2n}{n+1}\right]^2. \qquad [18]$$

For $n = 1.55$ this ratio is 1.48. Experiments[70-72] carried out on ED-2 laser glass ($n = 1.55$) agree with this estimate. Furthermore, with the beam incident and emerging at the Brewster's angle (no reflection), the damage thresholds were found to be the same.

In a recent paper Bloembergen[73] has pointed out that the same Fresnel reflection effect reduces the damage threshold at surfaces due to presence of micropores and cracks. Depending on the geometry of this crack, a reduction of the damage threshold by a factor of 2 to 100 over the bulk value may occur. This implies that application of polishing techniques, such as chemical treatments[74,75] or ion polishing,[76,77] which hopefully remove the surface cracks and inclusions, can raise the surface damage threshold. This has been demonstrated by several workers.[74-77] Fig. 14 shows the increase in damage threshold for a ruby laser incident on sapphire as a result of ion beam polishing.

These new interpretations of surface damage phenomena have prompted ARPA (U.S. Advanced Research Projects Agency) to launch a two-year, million-dollar program to capitalize on the discovery.[78] One of ARPA's priority goals is to protect windows against intense infrared laser beams and against atmospheric deterioration. The requirements are for 0.1% antireflection and protective coatings on alkali halides such as KCl and KBr, with absorption loss held below 0.0001 per surface. Anti-reflection coatings of ZnSe and CdTe also are needed with similar specifications. When the absorption is high due to im-

perfections, phase distortions of the optical beam degrades the beam quality. Thus coatings should be uniform within 1/40 of a wavelength.

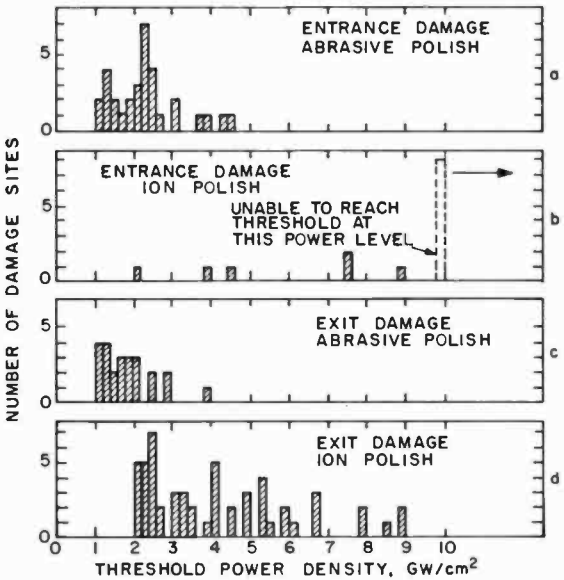

Fig. 14—Number of damage sites[77] as a function of threshold power density at entrance and exit surfaces of sapphire crystals for abrasively polished and ion-beam-polished samples.

4. Damage in Infrared Components

The limitations imposed by the damage susceptibility of infrared components, primarily windows and mirrors, are becoming increasingly evident. It is only recently that this area has received systematic careful attention. However, the problems are very similar to those already discussed. Weak absorption that is insignificant at low power levels can lead to unacceptable degradation of performance and to eventual component failure at high power levels.

4.1 Absorption Mechanisms in Infrared Windows

The origin of the absorption mechanism in transparent infrared materials with small but troublesome residual bulk absorption ($\beta \leqslant 10^{-2}$) has been reviewed by Hellwarth.[79] He considers the problems most pertinent to the fabrication of better laser windows in the

infrared and especially at the CO_2 laser wavelength (10.6 μm). Hellwarth emphasizes two types of absorption mechanisms namely extrinsic and intrinsic.

(a) Extrinsic absorption mechanisms

In crystals and glasses of near-ideal structure, the small residual absorption due to impurities, deviations from stoichiometry, dislocations, etc., can be considered as a simple superposition of the absorption from each such imperfection. That is, the absorption per cm $\beta(\omega)$ at frequency ω is given by

$$\beta(\omega) = \sum_i N_i \sigma_i(\omega) \qquad [19]$$

where the sum is over the various types of imperfections whose number densities are N_i and absorption cross sections σ_i. The processes giving rise to $\sigma_i(\omega)$ may be divided into the following: (1) excitation of polar vibration; (2) absorption by free carriers donated by impurities, and (3) excitation of bound-electron impurity states.

In any given material and at a specific frequency ω, the relevant cross sections of vibration of impurity atoms, ions, molecules, etc., must be determined by experiment. An excellent review on this subject is given in the proceedings of the Conference on High Power Infrared Laser Window Materials[80] (Oct. 1971). Unfortunately, the impurity atoms and molecules that appear to produce troublesome absorption at 10.6 μm and at other infrared laser wavelengths have not been studied adequately in the candidate materials for high-power windows. These impurities are primarily oxygen and hydroxyl radicals covalently bounded in various configurations. The absorption cross sections σ_i at 10.6 μm for metal-oxygen bounds generally lie between 10^{-18} and 10^{-20} cm^2.

Free carriers donated by impurities contribute a term β_e to the optical absorption in cm^{-1} and can be approximately by the Drude formula

$$\beta_e = \frac{30}{\rho n(\omega)(1 + \omega^2\tau^2)} \text{ cm}^{-1} \qquad [20]$$

where ρ is the resistivity in ohm-cm, $n(\omega)$ is the real part of the refractive index, and τ is the free carrier collision time. Since τ is of the order of an infrared period, the factor $(1 + \omega^2\tau^2)$ is of order one. Thus a material, whose resistivity is less than or of the order of 10^3 ohm-cm, has a value of β_e that is too high, and usually is not con-

sidered for use in high-power windows. An important exception is pure germanium, whose resistivity is about 20 ohm-cm but still has a low absorption of 0.017 cm^{-2} at 10.6 μm.

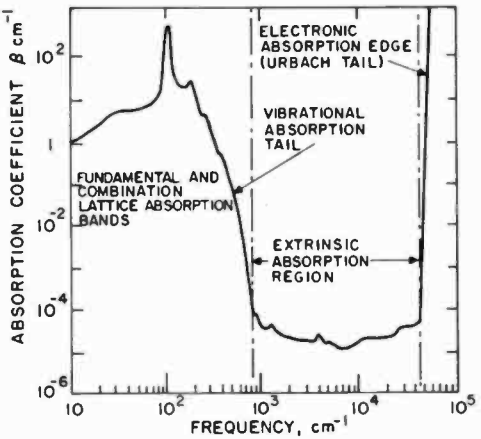

Fig. 15—Schematic plot[79] of the optical absorption coefficient β versus optical frequency for a typical material that would be a good candidate for a high-power-laser window by virtue of its low extrinsic absorption ($\beta < 10^{-4}$). The extrinsic-absorption-region spectrum of a good window material has never been scanned and is drawn here entirely from imagination. The exponential forms of the intrinsic vibrational absorption tail and the electronic absorption tail appear to be universal.

Heavy-particle impurities have vibrational frequencies so low that the wing of their vibrational absorption contributes negligibly at 10.6 μm and shorter wavelengths. However, such impurities may still absorb radiation in the infrared via the electronic absorption tail. This has been estimated[79] to be of the order of 10^{-18} cm^2 in the infrared if the line is Lorentzian in its low-frequency tail. Fig. 15 shows schematically[79] how the extrinsic absorption of a typical material might behave in the transparent wavelength region. However, whether or not the bumps in Fig. 15 actually exist is not yet known. The absorption below 10^{-2} cm^{-1} is too low to be scanned by usual techniques. It would be of great value to the understanding of window material absorption to know the absorption over a wide range of frequencies in this low-absorption region.

(b) Intrinsic absorption

At present, very little is known of the fundamental lower limit on the absorption of crystals at wavelengths where they are most transparent to radiation. The intrinsic absorption mechanisms are those that give rise to the electronic and vibrational absorptions that would exist in an ideal crystal or glass of some specified composition and possessing the stucture and vacancy system appropriate to its ambient temperature. In general, the extrinsic absorption mechanism seems to dominate in the best contemporary materials.

In addition to these mechanisms, absorption at the surface and in coatings can affect high-power-window performance. At present, our knowledge in these regards is not very clear.

4.2 Damage in Windows

Several research programs were undertaken during the past few years to develop high-power IR windows. In this section we discuss only two key studies,[81-85] which are most extensive and cover most of the important findings.

One important phenomenon that can occur when a high-power laser beam is incident on a window material is thermally induced optical distortion.[81] An incident laser beam having its greatest intensity at the center of the window causes a corresponding temperature gradient in the window. The bulging of the window and the change in the index of refraction cause the window to act as a lens with finite focal length and aberration. The effect of thermal lensing distorts the optical quality of the beam; this usually occurs before material damage sets in. A similar effect[82] is caused by a pressure differential across the windows.

Sparks[83] studied these effects systematically and discussed in detail the limitations of weak absorption in window materials at 10.6 μm. For 10-cm diameter (D) windows and with an applied 7.3 psi pressure differential, he defined a figure of merit on the basis of the maximum intensity that could be transmitted through a given material without experiencing thermal fracture or undue distortion. The latter can arise either due to thermal- or pressure-induced distortion (bowing). His results are shown in Tables 9 and 10. The first column of figures in Table 9 on the left shows the value l_f of window thickness required to keep the window from fracturing under pressure $P = 7.3$ psi with a safety factor of 4. The values of l_o are those required to keep the pressure-induced optical distortion from halving the beam intensity at the target. Of the materials studied, ZnSe was identified as the

Table 9—Minimum Window Thickness*[83]

Material	Fracture l_f/D values below	Pressure-induced optical distortion l_o/D values below for $D = 1$ cm	$D = 10$ cm	$D = 100$ cm
ZnSe	0.030	0.0123	0.0196	0.031
KCl	0.129	0.0140	0.0221	0.0351
CdTe	0.0803	0.0166	0.0263	0.0417
NaCl	0.125	0.0125	0.0199	0.0315
GaAs	0.0165	0.0126	0.020	0.0318
KRS-5 (TlBr-TlI)	0.0380	0.0223	0.0353	0.0560
$Ge_{28}Sb_{12}Se_{60}$ glass	0.0427	0.0184	0.0292	0.0463
Ge	0.0201	0.0124	0.0196	0.0310
KBr	0.185	0.0149	0.0236	0.0374

* Here $\lambda = 10.6$, pressure differential = 7.3 psi, pressure safety factor = 4, D = diameter of window, l = clamped window thickness, l_f = thickness required to prevent pressure-induced fracture, and l_o = thickness required to prevent pressure-induced optical distortion causing a reduction by half in target intensity. The minimum usable thickness is the greater of l_o and l_f. Underscores indicate cases when $l_o > l_f$.

most promising at 10.6 μm, allowing a power density of 3.76 kW/cm² to be transmitted with a pressure safety factor of 4 limited by the pressure-induced fracture of the window (Table 10).

At present, there is considerable confusion concerning the appropriate value of the absorption coefficient for various materials.

Table 10—Figures of Merit or Maximum Intensity for Pulse Mode in 10-cm Diameter Windows*[83]

Material	Measured values of β in cm^{-1}	$<I>_{lf}$ kW/cm²	$<I>_{l_f}$ kW/cm²	$<I>_{l_o}$ kW/cm²	$<I>_{1cm}$ kW/cm²
ZnSe	5×10^{-3}	20.4	3.76	5.76	1.13
KCl	4.8×10^{-4}	3.02	37.8	220.	48.8
CdTe	1.5×10^{-3}	14.6	1.07	3.25	0.859
NaCl	1.3×10^{-3}	0.971	23.1	145.	29.0
GaAs	5×10^{-3}	40.5	1.15	0.949	0.190
KRS-5	5×10^{-3}	3.62	0.377	0.406	0.143
$Ge_{28}Sb_{12}Se_{60}$ glass	0.02	1.56	0.171	0.251	0.073
Ge	0.025	4.9	0.149	0.154	0.030
KBr	4×10^{-3}	0.144	3.75	29.6	6.98

* Here $\lambda = 10.6$, pressure differential = 7.3 psi and pressure safety factor = 4, l_f and l_o are the same as in Table 9 for $D = 10$ cm and $<I>$ is the maximum intensity value given in the table for thermal fracture or pressure fracture or distortion or for a window thickness of 1 cm. The underscore denotes the minimum $<I>$ of the former three.

threshold values of various substrates (Mo, Cu, Ni, Quartz, etc.), metal films (Au, Ag, and Cu) and dielectric coating ($ThF_4/CdTe$) were performed using a pulsed CO_2 laser. The mirror samples were exposed to 10.6 μm pulses of 1 to 10 μsec duration with energy fluxes of up to 200 J/cm^2. A typical high-power mirror designed to operate in a cw mode is shown in Fig. 16. The calculated power and energy

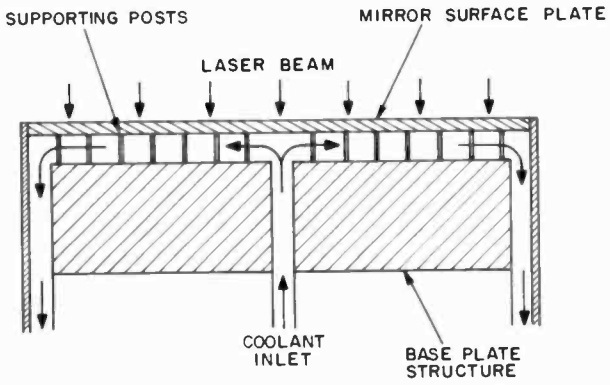

Fig. 16—CW water-cooled mirror.[87]

density limitations of this type of mirror over a wide range of pulse lengths are shown in Fig. 17. This figure illustrates that the pulse response characteristics can be divided into the following three regions, namely (a) quasi-cw limited ($\tau > 10^{-2}$ sec, region C), (b) face plate distortion limited ($10^{-4} < \tau < 10^{2}$, region B) and (c) surface thermal effect limited ($\tau < 10^{-4}$ sec, region A). Results of the measurements for various types of mirrors are shown in Tables 12, 13, and 14. The status of the three types of mirrors tested has been summarized in Table 15. It shows that at present, simple metal mirrors have exhibited the highest resistance to damage, with threshold values in excess of 140 J/cm^2 for 8 to 10 μsec pulses. A simple extrapolation of these results indicates that an incident flux in excess of 500 J/cm^2 for pulses of 50 μsec can be handled with simple mirrors. For thin metal mirrors the threshold values are between 75 and 140 J/cm^2.

The thermal and mechanical bond of the thin film to the substrate plays an important role in the performance of these mirrors. The poor performances of multilayer dielectric mirrors are attributed to local absorption centers within the dielectric, which nucleate damage

Table 12—Metal Mirrors[87]

Substrate	Coating	Absorption	Tested Energy Density (± 30%) at Threshold & Pulse Length
Copper	None	~ 2%	> 140 J/cm² (10 μsec)
Mo	None	2%	> 140 J/cm² (2 μsec)
Electroless Nickel	None	8.6%	10-30 J/cm³ (1 μsec)

Table 13—Thin Film Metallic Mirrors[87]

Substrate	Coating	Absorption	Tested Energy Density (± 30%) at Threshold & Pulse Length
Copper	Sputtered Cu	~ 2%	> 140 J/cm² (10 μsec)
Copper	Vacuum deposited Cu	1%	~ 140 J/cm² (10 μsec)
Copper	Ag/ThF_4	1%	40-70 J/cm² (10 μsec)
Mo/braze	50 μin Au	1.5%	~ 75 J/cm² (10 μsec)
Mo	Vacuum deposited Cu	1%	75-140 J/cm² (10 μsec)
Electroless Nickel	Ag	0.7%	20-40 J/cm² (2 μsec)
Quartz	Ag/ThF_4	1%	~ 10 J/cm² (2 μsec)

Table 14—Dielectric Mirrors[87]

Substrate	Coating (no. of Dielectric Layers)	Absorption	Tested Energy Density (± 30%) at Threshold & Pulse Length
Electroless Nickel	Cu/ThF_4/CdTe (2)	0.5%	10 J/cm² (2 μsec)
Electroless Nickel	Ag/ThF_4/CdTe (6)	0.2%	10 J/cm² (1 μsec)
Electroless Nickel	Ag/ThF_4/CdTe (6)	0.2%	10 J/cm² (8 μsec)
Molybdenum	Cu/ThF_4/CdTe (2)	0.5%	10 J/cm² (10 μsec)

Table 15—Summary of Measurements[87] on Mirrors With a CO_2 Laser Beam (8-10 μsec)

	Metal	Thin Film Coated Metal	Multilayer Dielectric
Mirror Material	Cu	Cu on Cu	CdTe-ThF_4-Cu on Mo
Absorption	~ 2%	~ 1%	~ 0.5%
Measured Threshold (Av)	> 140 J/cm²	75-140 J/cm²	7-10 J/cm²

sites in the dielectric. However, it is expected that if the low absorption of these mirrors is uniformly maintained and the absorption centers removed, the ultimate performance of these mirrors may be far superior to metal reflectors, especially at short pulse lengths ($\sim 10^{-9}$ sec). Damage in mirrors were also studied by Horrigan et al.[85] Tables 16, 17, and 18 summarize their results.

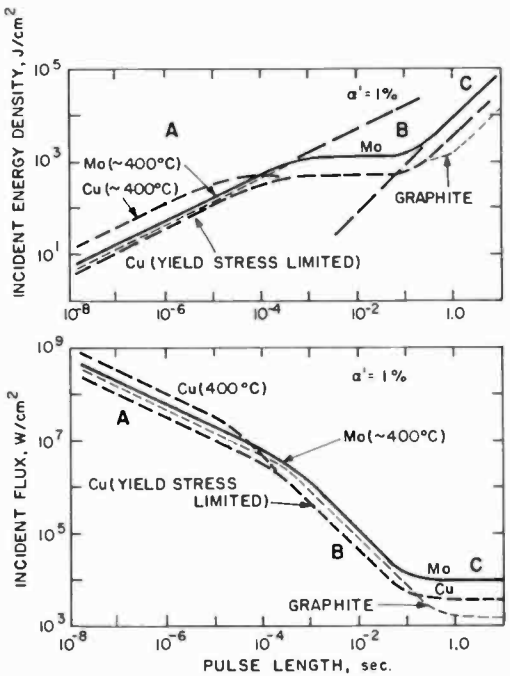

Fig. 17—Calculated[87] maximum mirror loading versus pulsewidth. The regions A, B, and C are discussed in the text and α' is the coefficient of thermal expansion.

4.4 Damage in Nonlinear Optical Materials

Nonlinear optical materials, generally in crystalline form, are used for modulation, Q-switching, and frequency multiplication in high-power laser systems. The operation of nonlinear devices involves exposure of these materials to high values of light intensity. For frequency multiplication the efficiency of conversion is strongly dependent on the incident power level.

Table 16—Deformation of Mirror Substrates[85]

Material	α' (°C^{-1})	K (cal/s, cm, °C)	Figure of Merit (K/α')
Pyrolytic a axis	-0.15×10^{-6}	1.00	6650×10^3
Graphite (PG) c axis	28×10^{-6}	0.008	0.285×10^3
Invar	0.15×10^{-6}	0.023	153×10^3
Tungsten	4.4×10^{-6}	0.40	91×10^3
Silicon	2.4×10^{-6}	0.20	84×10^3
Molybdenum	4.2×10^{-6}	0.34	82×10^3
Beryllium	9.0×10^{-6}	0.396	44×10^3
Copper	17.7×10^{-6}	0.948	54×10^3
Silver	19.4×10^{-6}	1.00	52×10^3
Gold	14.2×10^{-6}	0.70	49×10^3
Germanium	5.5×10^{-6}	0.14	25.4×10^3
Aluminum	28.8×10^{-6}	0.57	20×10^3

Table 17—Destruction of Reflective Coatings[85]

Material	β Avco	β AIP Handbook	T_{dest} (°C)	Figure of Merit T_{dest}/β	
Ag	0.0042	0.011	1234	2.9×10^5	1.1×10^5
Au	0.0065	0.016	1336	2.1×10^5	0.8×10^5
Cu	0.0053	0.012	1357	2.6×10^5	1.2×10^5
Dielectric*	0.002		400	2×10^5	
Dielectric**	0.0065		~ 1300	2×10^5	

* Spectrum System coating
** Laser Optic coating

Table 18—Figure of Merit for Solid Mirrors[85]

Material Parameters*

Material	R (%)	$\beta = 1 - R$ (cm^{-1})	K (cal/s, cm, °C)	c (cal/gm, °C)	α' (°C^{-1})	$T_{dest} = T_{melt}$ (°C)
Ag	99.58	0.0042	1.006	0.06	19.4×10^{-6}	1234
Au	99.35	0.0065	0.705	0.03	14.2×10^{-6}	1336
Cu	99.47	0.0053	0.918	0.09	16.8×10^{-6}	1357

Figures of Merit

	Deformation	Destruction	
Material	$K/\alpha'\beta$	Quasi cw KT_{melt}/β	Transient cT_{melt}/β
Ag	12.3×10^6	29.4×10^4	1.76×10^4
Au	7.6×10^6	14.5×10^4	0.62×10^4
Cu	10.0×10^6	23.5×10^4	2.30×10^4

* R = reflectivity at 10.6 μ, β = absorption coefficient, K = thermal conductivity, c = specific heat, and α' = coefficient of thermal expansion.

In the 1971 Damage Symposium, several authors[55,88] observed that the damage levels observed in harmonic generation were far lower in the presence of the harmonic than those observed with just the fundamental present. Thus, in barium sodium niobate exposed to 1.065 μm radiation, only the surface damage was observed at 3 MW/cm^2, while in the presence of the green harmonic, damage occurred[88] at 10 kW/cm^2. Table 19 shows some of the results obtained by Bass and Barrett.[55] Hanna et al[89] made damage threshold measurements with

Table 19—Critical Power for Surface Damage in Nonlinear Optical Materials[55]

Material	GW/cm^2
ADP	6.4
KDP	14.4
Crystal quartz	6.4
$LiNbO_3$	11.1
$Ba_2NaNb_5O_{15}$	6.4
$LiIO_3$	3.2
$SrTiO_3$	6.4

All data taken in 15 nsec pulse at 1.065 μm

Q-switched lasers for prousite, pyrargyrite, cinnabar, silver thiogallate, tellurium, and GaAs at wavelengths of 0.694, 1.06, 2.098 and 10.6 μm. Their results at 10.6 μm are summarized in Table 20. Damage is found to be confined to the surface of the crystals and occurs for intensities between 3 and 75 MW/cm^2. Particular care is needed in cutting and polishing tellurium crystals if a high damage threshold is to be achieved. Other phase-matchable crystals studied by various workers[90-92] are $ZnGeP_2$, $CdGeAs_2$, and CdSe. For the first two materials the damage thresholds are low. In contrast, much better quality CdSe crystals show a high threshold of 60 MW/cm^2.

5. Conclusions

The status of present knowledge regarding high-power laser damage to solids has been discussed. Depending on the laser power level and pulse duration, various metal-target damage thresholds such as melting, vaporization, composite effect and plasma shielding, may be defined. It appears that data on the CO_2 laser-metal interaction is very meager. Damage in transparent solids may occur either in bulk or at the surfaces. The bulk damage arises from one or more of the following physical effects: particulate inclusions within the solid, sub-

Table 20—CO_2 Laser Damage Threshold[89] (Pulse Width = 200 ns, Pulse Repitition Frequency = 200 pps)

Number of Pulses	Prousite	Pyrargyrite	Silver Thiogallate	Gallium Arsenide	Tellurium*		
					Type a	Type b	Type c
1	< 76MW/cm²	< 76MW/cm²	—	< 107MW/cm²	—	—	63MW/cm²
100	53MW/cm²	—	—	76MW/cm²	—	—	—
300	—	53MW/cm²	—	—	—	—	—
1000	—	—	25MW/cm²	—	10MW/cm²	—	43MW/cm²
10,000	—	—	—	—	—	63MW/cm²	—
> 30,000	> 46MW/cm²	> 46MW/cm²	—	> 63MW/cm²	> 30MW/cm²	> 30MW/cm²	> 43MW/cm²

* Tellurium type a are WACKER samples mechanically cut and etched,
type b are CNET samples mechanically cut and etched, and
type c are HOBOKEN samples chemically cut and etched.

focusing of the radiation, electron avalanche breakdown, or stimulated Brillouin scattering. The surface damage occurs both on the front and back surfaces, with plasma formation and spalling. Compressional waves, Fresnel reflection effects, micropores, and surface cracks are contributing factors.

Acknowledgments

This study was jointly supported by Defense Research Establishment, Valcartier, Quebec and by RCA. The author wishes to acknowledge constant help and encouragement from Dr. I. P. Shkarofsky in all phases of the program.

References

[1] P. J. Klass, "Special Report: Laser Thermal Weapons," **Aviation Week and Space Tech.**, Vol. 97, p. 12, Aug. 14 (1972).

[2] M. C. Richardson, A. J. Alcock, K. Leopold, and P. Burtyn, "A High Power High Energy TEA CO_2 Laser," presented at 7th Int. Conf. on Quant. Elec., Montreal (1972).

[3] A. J. Glass and A. H. Guenther, "Laser induced damage of optical elements," **Proc. Japan-US Seminar on 'Laser Interaction with Matter'**, (C. Yamanaka, editor), p. 119 (1973).

[4] J. F. Ready, **Effects of High-Power Laser Radiation,** Academic Press, N.Y., Chap. 3 (1971).

[5] S. I. Anisimov, "Vaporization of metal absorbing laser radiation," **Sov. Phys. JETP,** Vol. 27, p. 182 (1968).

[6] S. I. Anisimov, A. B. Bonch-Bruevich, M. A. Elyashevich, Ya. A. Imas, N. A. Pavlenko, and G. S. Romanov, "Effect of powerful light fluxes on metals," **Sov. Phys. Tech. Phys.**, Vol. 11, p. 945 (1967).

[7] A. M. Bonch-Bruevich and Ya. A. Imas, "Recoil Momentum and Ejection of Metal Particles Under the Action of a Giant Laser Pulse," **Sov. Phys. Tech. Phys.**, Vol. 12, p. 1407 (1968).

[8] C. Adams and G. A. Hardway, "Fundamentals of Laser Beam Machining and Drilling," **Trans. IEEE Indust. Gen. Appl.**, Vol. IGA-1, p. 90 (1965).

[9] M. K. Chun and K. Rose, "Interaction of High-Intensity Laser Beams with Metals," **J. Appl. Phys.**, Vol. 41, p. 614 (1970).

[10] P. Veyrie, "Breakdown, Shock and Radiation Waves in Plasma Created by Lasers," AIAA Fluid and Plasma Dynamics Conf., Los Angeles, Calif., June (1968).

[11] F. P.Gagliano, R.M. Lumley, and L. S. Watkins, "Lasers in Industry," **Proc. IEEE**, Vol. 57, p. 114 (1969).

[12] R. D. Haun, Jr., "Laser applications," **IEEE Spectrum,** Vol. 5, p. 82 (1968).

[13] E. V. Locke, E. D. Hoag, and R. A. Hella, "Deep Penetration Welding with High-Power CO_2 Lasers," **J. Quadt. Elec.**, Vol. 8, p. 132 (1972).

[14] R. F. Schneidmiller and J. H. Richardson, "Laser Damage of Materials," Aerospace Corp., El Segundo, Report No. TDR-469 (5250-10)-5 (1965).

[15] M. I. Cohen, "Melting of a Half-Space Subjected to a Constant Heat Input," **J. Franklin Inst.**, Vol. 283, p. 271 (1967).

[16] J. N. Gonsalves and W. W. Duley, "Interation of CO_2 Laser Radiation with Solids. I Drilling of Thin Metallic Sheets," **Can. J. Phys.**, Vol. 49, p. 1708 (1971).

[17] J. F. Asmus and F. S. Baker, "Nonlinear Surface Phenomena Associated with Laser Beam Penetration," 10th Symp. on Electron, Ion and Laser Beam Tech. (L. Marton, editor), San Francisco Press, p. 241 (1969).

[18] J. F. Ready, "Effects Due to Absorption of Laser Radiation," **J. Appl. Phys.**, Vol. 36, p. 462 (1965).

[19] S. I. Anisimov, "Evaporation of a Light-Absorbing Metal," **High Temperature (USSR),** Vol. 6, p. 110 (1968).

[20] H. G. Landau, "Heat Conduction in a Melting Solid," **Quart. J. Appl. Maths.**, Vol. 8, p. 81 (1950).

[21] Yu. V. Afanasev and O. N. Krokhin, "Vaporization of Matter Exposed to Laser Emission," **Sov. Phys. JETP,** Vol. 25, p. 639 (1967).

[22] P. I. Ulyakov, "Some Laws Governing the Breakdown of Solids by Laser Radiation," **Sov. Phys. JETP,** Vol. 25, p. 537 (1967).

[23] C. M. Leech, "The Prediction of Thermodynamic Damage of Materials Irradiated by Intense Laser Beam," DREV Report R-672/72, Project 99-10-44, Nov. (1972).
[24] J. F. Ready, "Development of Plume of Material Vaporized by Giant-Pulse Laser," **Appl. Phys. Lett.**, Vol. 3, p. 11 (1963).
[25] F. W. Dabby and U.-C. Paek, "High Intensity Laser-Induced Vaporization and Explosion of Solid Material," **J. Quant. Elec.**, Vol. 8, p. 106 (1972).
[26] M. V. Akmanova, V. A. Kaygorodov, and A. V. Karayakin, "Investigation of Vaporization of Processes and the Development of a Plasma During Laser Irradiation of Various Materials," **Zh. Prikl Spektrosk. USSR (J. Appl. Spectroscopy)**, Vol. 8, p. 584 (1968); A. I. Korunchikov, V. V. Pantileyev, O. I. Puterenko, and A. A. Yankovskiy, "Some Trends in Metal Ejection by Laser Radiation," **Zh. Prikl. Spektrosk. USSR (J. Appl. Spectroscopy)**, Vol. 12, p. 819 (1970).
[27] F. P. Gagliano and U. C. Paek, "Explosion of Solid Materials," IEEE/OSA Conf. on 'Laser Engineering and Applications', Wash., D.C. (1973).
[28] V. A. Komotoskii, "Maximum Evaporation Rate from a Metal Surface," **Sov. Phys. Tech. Phys.**, Vol. 16, p. 168 (1971).
[29] B. M. Zhiryakov, N. N. Kykalin, A. A. Uglov, and A. K. Fannibo, "Metal Destruction Caused by Focussed Laser Radiation," **Sov. Phys. Tech. Phys.**, Vol. 16, p 815 (1971).
[30] S. I. Andreev, I. V. Verskikovskii, and Yu. I. Dymshits, "Plasma Formation in a Solid Target by a Single-Shot Laser," **Sov. Phys. Tech. Phys.**, Vol. 15, p. 1109 (1971).
[31] G. R. Levinson and V. I. Smilga, "Experimental Study of Damage Threshold in Thin Metal Films from Effects of Laser Radiation," **Fizika i Khimiya Obrat. Materiolov**, No. 4, p. 124 (1971).
[32] A. J. Glass and A. H. Guenther, Eds., **Damage in Laser Glass**, ASTM Special Tech. Publ. 469 (1969).
[33] A. J. Glass and A. H. Guenther, Eds., **Damage in Laser Materials**, NBS Special Publ. 341 (1970).
[34] A. J. Glass and A. H. Guenther, Eds., **Damage in Laser Materials**, NBS Special Pub. 356 (1971).
[35] A. J. Glass and A. H. Guenther, Eds., **Laser Induced Damage in Optical Materials**, NBS Special Pub. 372 (1972).
[36] A. J. Glass and A. H. Guenther, "Laser Induced Damage of Optical Elements—a Status Report," **Applied Optics**, Vol. 12, p. 637 (1973).
[37] M. Hercher, "Laser Induced Damage in Transparent Media," **J. Opt. Soc. Amer.**, Vol. 54, p. 563 (1964).
[38] E. Bernal, "Absorption of Laser Radiation by Transparent Crystalline Solids," **J. Opt. Soc. Amer.**, Vol. 55, p. 602 (1965).
[39] B. M. Ashkinadze et al, "Breakdown in Transparent Dielectrics Caused by Intense Laser Radiation," **Sov. Phys. JETP**, Vol. 23, p. 788 (1966).
[40] N. V. Volkova, V. A. Likhachev, S. M. Ryvkin, V. M. Salmanov, and I. D. Yaroshetskii, "Fracture of LiF Single Crystals under the Action of Laser Radiation," **Sov. Phys.—Solid State**, Vol. 8, p. 2133 (1967).
[41] N. P. Novikov, S. S. Saluenya, F. N. Chernyavskii, and Yu. I. Yudin, "Laser Radiation-Induced Breakdown Processes in Polymers at the Load Limit," **Sov. Phys. Solid State**, Vol. 10, p. 2990 (1969).
[42] H. Bennet, "Absorption Centers in Laser Glasses," p. 51 In Ref. 33.
[43] R. W. Hopper, C. Lee and D. R. Ullmann, "The Inclusion Problem in Laser Glass," p. 55 in Ref. 33.
[44] E. S. Bliss, "Pulse Duration Dependence of Laser Damage Mechanism," **Opto-Electronics**, Vol. 3, p. 99 (1971) (also in Ref. 33, p. 105).
[45] T. Isumitani, K. Hosaka, and C. Yamanaka, "Laser Damage of HOYA Laser Glass, LCG-11," in Ref. 35, p. 3.
[46] R. Y. Chiao, E. Garmire, and C. H. Townes, "Self Trapping of Optical Beams," **Phys. Rev. letters**, Vol. 13, p. 479 (1964).
[47] S. A. Akhmanov, A. P. Sukhorov, and R. V. Khoklov, "Self-Focussing and Diffraction of Light in a Nonlinear Medium," **Sov. Phys. USPEKHI**, Vol. 10, p. 609 (1968).
[48] J. Margurger, "Theory of Self-Focussing for Fast Nonlinear Response," In Ref. 34, p. 51.
[49] E. L. Kerr, "Electrostrictive Laser Beam Focusing in Glass and Small Scale Track Formation," in Ref. 34, p. 61.
[50] C. R. Giuliano, "Time Evolution of Damage Tracks in Sapphire and Ruby," in Ref. 35, p. 44.
[51] D. W. Fraden, Eli Yablonovitch, and M. Bass, "Comparison of Laser Induced Bulk Damage in Alkali-Halides at 10.6, 1.06 and 0.69 Microns," in Ref. 35, p. 27.
[52] Eli Yablonovitch, "Optical Dielectric Strength of Alkali-Halide Crystals Obtained by Laser-Induced Breakdown," **Appl., Phys. Letters**, Vol. 19, p. 495 (1971).
[53] T. P. Belikova, A. N. Savchenko, and E. A. Sviridenkov, "Optic Breakdown in Ruby and Related Effects," **Sov. Phys. JETP**, Vol. 27, p. 19 (1968).
[54] A. Wasserman, "A Mechanism for Damage in Solids by Intense Light," **Appl. Phys. Letters**, Vol. 10, p. 132 (1967).
[55] M. Bass and H. H. Barrett, "The Probability and Dynamics of Damaging Optical Materials With Lasers," in Ref. 34, p. 76.

[56] W. Shockley, "Problems Related to P-N Junctions in Silicon," **Czeck, J. of Phys.**, Vol. B11, p. 81 (1961).
[57] C. R. Giuliano, "Laser-Induced Damage to Transparent Dielectric Materials," **Appl. Phys. Lett.**, Vol. 5, p. 137 (1964).
[58] A. I. Ritus and A. A. Manenkov, "Stimulated Mandelshtam-Brillouin Scattering in Fused and Crystalline Quartz Without Damage to Samples at T = 300°K," **Sov. Phys. JETP Lett.**, Vol. 6, p. 349 (1967).
[59] D. A. Kramer and R. E. Honig, "Evidence of Laser-Induced Brillouin Scattering in CdS," **Appl Phys. Lett.**, Vol. 13, p. 115 (1968).
[60] R. Y. Chiao, E. Garmire, and C. H. Townes, "Raman and Photon Masers," p. 326, **Proc. E. Fermi Int. School of Physics, Course XXXI**, ed, C. H. Townes and P. A. Miles, Academic Press, N.Y. (1964).
[61] R. Y. Chiao, C. H. Townes, and B. P. Stoicheff, "Stimulated Brillouin Scattering and Coherent Generation of Intense Hypersonic Waves," **Phys. Rev. Lett.**, Vol. 12, p. 592 (1964).
[62] N. M. Kroll, "Excitation of Hypersonic Vibrations by Means of Photoelastic Coupling of High Intensity Light Waves to Elastic Waves," **J. Appl. Phys.**, Vol. 36, p. 34 (1965).
[63] E. E. Hagenlocker, R. W. Minck, and W. G. Rado, "Effects of Photon Lifetime on Stimulated Optical Scattering in Gases," **Phys. Rev.**, Vol. 154, p. 226 (1967).
[64] G. M. Zverev, T. N. Mikhailova, V. A. Pashkov, and N. M. Soloveva, "Mechanisms of Destructions of Ruby and Lenco Sapphire Crystals by Powerful Laser Radiation," **Sov. Phys. JETP**, Vol. 26, p. 1053 (1968).
[65] C. R. Giuliano and L. D. Hess, "Damage Threshold Studies in Ruby and Sapphire," p. 76 in Ref. 33.
[66] L. D. Khazov, A. N. Shestov and G. P. Tikhomirov, "Luminous Discharge on Non-absorbing Surfaces Produced by a Single Pulse Laser," **Sov. Phys. Tech. Phys.**, Vol. 13, p. 1112 (1969).
[67] I. A. Fersman and L. D. Khazov, "Damage of Transparent Dielectric Surfaces by a Laser Beam," **Sov. Phys. Tech. Phys.**, Vol. 15, p. 835 (1970).
[68] C. R. Giuliano, "The Relation Between Surface Damage and Surface Plasma Formation," p. 46 in Ref. 35.
[69] N. L. Boling and R. W. Beck, "Laser Glass Damage Threshold Studies at Owens-Illinois," p. 15 in Ref. 34.
[70] N. L. Boling, M. D. Crisp, and G. Dube, "Laser Induced Surface Damage," **Appl. Optics**, Vol. 12, p. 651 (1973).
[71] N. L. Boling and G. Dube, "Laser Induced Damage to Glass Surfaces," p. 40 in Ref. 35.
[72] M. D. Crisp, N. L. Boling, and G. Dube, "Importance of Fresnel Reflections in Laser Surface Damage of Transparent Dielectrics," **Appl. Phys. Lett.**, Vol. 21, p. 364 (1972).
[73] N. Bloembergen, "Role of Cracks, Pores and Absorbing Inclusions on Laser Induced Damage Threshold at Surfaces of Transparent Dielectrics," **Appl. Optics**, Vol. 12, p. 661 (1973).
[74] J. E. Swain, "Surface-Damage Threshold Measurements for Several Laser Glasses," p. 69 in Ref. 32.
[75] Darlt, J., "Laser Damage in Optical Glasses," p. 100 in Ref. 32.
[76] A. H. Guenther, "Air Force Weapon Laboratory Commander's Report," (AFWL, Kirtland AFB N.M. 1971), p. 8.
[77] C. R. Giuliano, "Ion Beam Polishing as a Means of Increasing Surface Damage Thresholds in Sapphire," p. 55 in Ref. 35.
[78] Laser Focus, Vol. 9, p. 12, Aug. (1973).
[79] R. Hellwarth, "Fundamental Absorption Mechanisms in High Power Laser Window Materials," p. 165 in Ref. 35.
[80] **Proc. Conf. on High Power Infrared Laser Window Materials**, (Oct. 1971), Ed. by C. S. Sahaglan and C. A. Pitha (AFCRL Special Report No. 127, Dec. 1971).
[81] M. Sparks, "Optical Distortion by Heated Windows in High Power Laser Systems," **J. Appl. Phys.**, Vol. 42, p. 5029 (1971).
[82] M. Sparks and M. Cottis, "Pressure-Induced Optical Distortion in Laser Windows," **J. Appl. Phys.**, Vol. 44, p. 787 (1973).
[83] M. Sparks, "Recent Developments in High-Power Infrared Window Research," p. 172 in Ref. 35.
[84] F. A. Horrigan, C. A. Klein, R. I. Rudko, and D. T. Wilson, "High Power Gas Laser Research," Raytheon (Waltham, Mass.) Report DA-AH01-67-1589, AD676226 (1968).
[85] F. A. Horrigan and R. I. Rudko, "Materials for High Power CO_2 Lasers," Raytheon Waltham, Mass.) Report DA-AH01-69-0038, AD693311 (1969).
[86] "High Power Infrared Laser Windows," National Materials Advisory Board (NAS-NAE) AD-745-927 (July 1972).
[87] V. Wang, A. I. Braunstein, M. Braunstein, and J. Wada, "Investigation of Pulsed CO_2 Laser Damage of Metal and Dielectric-Coated Mirrors," **Proc. 1972 Symp. ASTM on 'Laser Induced Damage in Optical Materials'** (A. J. Glass and A. H. Guenther, editors), NBS Special Publ. 372, p. 183 (1972).

[88] R. Webb, "Catastrophic Surface Damage Produced in $Ba_2NaNb_5O_{15}$ Crystals During Intracavity Frequency Doubling," p. 98 in Ref. 34.

[89] D. C. Hanna, B. Luther-Davies, H. N. Rutt, R. C. Smith, and C. R. Stanley, "Q-Switched Laser Damage of Infrared Nonlinear Materials," **IEEE J. Quant. Elec.**, Vol. QE-8, p. 317 (1972).

[90] G. D. Boyd, E. Buehler, and F. G. Storz, "Linear and Nonlinear Optical Properties of $ZnGeP_2$ and CdSe," **Appl. Phys. Lett.**, Vol. 18, p. 301 (1971).

[91] R. L. Byer, H. Kildal, and R. S. Feigelson, "$CdGeAs_2$—A New Nonlinear Crystal Phase Matchable at 10.6 μm," **Appl. Phys. Lett.**, Vol. 19, p. 237 (1971).

[92] R. L. Herbst and R. L. Byer, "Efficient Parametric Mixing in CdSe" (to be published).

Errata Notice

In the December 1973 issue of RCA Review, Fig. 14 (p. 626) in the paper, "The Chemical Polishing of Sapphire and Spinel," by P. H. Robinson and R. O. Wance is incorrect. The concentrations of Al_2O_3 in the melt shown for each curve should be as shown in the corrected figure given here.

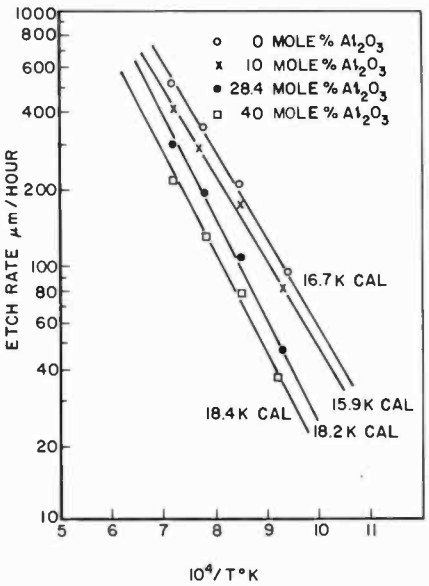

FIG. 14

Fig. 14—Etch rate versus temperature.

Recent Papers by RCA Authors

Listing is alphabetical by name of primary author. For copies of reprints, the reader should contact the publication directly.

K. Ametani, "Estimation of Chlorine Content in Single Crystals of Chromium Chalcogenide Spinels by Atomic Absorption Spectrophotometry," **Bull. Chem. Soc. of Japan,** Vol. 47, No. 1, p. 242, Jan. 1974.

J. Blanc, "Diffusion Coefficients Varying with a Power of the Concentration: Convenient Solutions and a Reexamination of Zn in GaAs," **J. of Appl. Phys.,** Vol. 45, No. 5.

J. E. Carnes, "Charge-Coupled Imaging: State of the Art," Proc. 3rd European Solid State Device Research Conf., p. 83-107, 1973.

G. C. Cody and G. W. Webb, "Superconductivity: Phenomena, Theory, Materials," **CRC Critical Reviews in Solid State Sciences,** Vol. 4, No. 1, p. 27-84, 1973.

M. S. Corrington, "Effectiveness of Continuous Spatial Average in a Diffuse Sound Field," **J. Acoust. Soc. Amer.,** Vol. 54, No. 3, p. 813, Sept. 1973.

M. S. Corrington, "Comments on 'Rytov's Method and Large Fluctucation'," Acoust. Soc. Amer., Vol. 54, No. 4, p. 15, Dec. 1973.

R. S. Crandall, "Lifetime of Surface-State Electrons on Liquid He," **Phys. Rev. A,** Vol. 9, No. 3, p. 1297, March 1974.

G. W. Cullen, M. T. Duffy, and C. C. Wang, "Materials Integration through Heteroepitaxial Growth on Insulating Substrates," **Chemical Vapor Disposition,** Fourth Int'l Conf., Boston, Oct. 1973.

J. G. Davy and J. J. Hanak "RF Bias Evaporation (Ion Plating) of Nonmetal Thin Films," **J. Vac. Sci. & Tech.,** Vol. II, No. 1, p. 43, Jan. 1974.

J. P. Dismukes and B. J. Curtis "An Investigation of Convective Effects," **Chemical Vapor Disposition,** 4th Int'l Conf., Boston, Oct. 1973.

J. P. Dismukes, J. Kane, B. Binggeli, and H. P. Schweizer, "Chemical Vapor Deposition of Cathodoluminescent Phosphor Layers," **Chemical Vapor Disposition,** 4th Int'l Conf., Boston, Oct. '73.

R. H. Dean, A. B. Dreeben, J. J. Hughes, R. J. Matarese, and L. S. Napoli, "Broad-Band Microwave Measurements on GaAs 'Traveling-Wave' Transistors," **IEEE Trans. Microwave Theory and Tech.,** Vol. MTT-21, No. 12, Dec. 1973.

R. H. Dean and B. B. Robinson, "Space-Charge Waves in Partially Depleted Negative Mobility," **IEEE Trans. Electron Dev.,** Vol. ED-21, No. 1, p. 61, Jan. 1974.

D. A . deWolf, "Strong Irradiance Fluctuations in Turbulent Air, III. Diffraction Cutoff," **J. Opt. Soc. Amer.,** Vol. 64, No. 3, p. 360, March 1974.

F. A. Eble, "Pocket Programs for Reliability Computation," **Proc. Reliability and Maintainability Symp.,** Los Angeles, Calif., Jan. 29-31, 1974.

M. Ettenberg, "Effects of Dislocation Density on the Properties of Liquid Phase Epitaxial GaAs," **J. Appl. Phys.,** Vol. 45, No. 2, p. 901, Feb. 1974.

M. Ettenberg, K. C. Hudson and H. F. Lockwood, "High-Radiance Light-Emitting Diodes," **IEEE J. Quantum Electronics,** Vol. QE-9, No. 10, p. 987, Oct. 1973.

M. Glicksman, R. E. Enstrom, S. A. Mittleman and J. R. Appert, "Electron Mobility in In(x)Ga(1–x)As Alloys," Phys. Rev., Vol. 9, No. 4, p. 1621, Feb. 15, 1974.

J. M. Hammer and W. Phillips, "Low-Loss Single-Mode Optical Waveguides and Efficient High-Speed Modulators of LiNb(x)Ta(1–x)O(3)" **Appl. Phys. Letters,** Vol. 24, No. 11, June 1974. (1)

J. J. Hanak and B. F. T. Bolker, "Calculation of Composition of Dilute Cosputtered Multicomponent Films," **J. Appl. Phys.,** Vol. 4, No. 11, Nov. 1973.

W. J. Hannan, R. E. Flory, M. Lurie and R. J. Ryan, "HoloTape: A Low-Cost Prerecorded Television System Using Holograph Storage", **J. SMPTE,** Vol. 82, No. 11, p. 905, Nov. 1973

T. T. Hitch, "Adhesion, Phase Morphology, and Bondability of Reactively Bonded and Frit-Bonded Gold and Silver Thick-Film Conductors," **J. Electronic Materials,** Vol. 3, No. 2, p. 552, 1974.

T. T. Hitch and J. J. Nunes, "A Method for the Rapid Orientation of Black-Reflection Laue X-ray Photographs for Zinc," **J. Appl. Crystallography,** Vol. 7, No. 1, Feb. 1974.

H. O. Hook, "The Capabilities and Limitations of Photolithography," **J. Vac. Sci. Tech.,** Vol. II, No. 1, Jan. 1974.

E. F. Hockings, "Selection of Scientific Periodicals in an Industrial Research Library," **J. of Amer. Soc. for Information Sci.,** Vol. 25, No. 2, March 1974.

W. Kern, "Characterization of Localized Structural Defects in Dielectric Films," **RCA Review,** Vol. 34, No. 4, p. 655, Dec. 1973.

R. W. Klopfenstein and R. K. Wehner, "The Electrostatic Field Near Weakly Deformed Conducting Surfaces," **RCA Review,** No. 4, Vol. 34, p. 630, Dec. 1973.

H. Kressel and H. F. Lockwood, "A Review of Gradual Degradation Phenomena in Electroluminescent Diodes," **J. de Physique,** Vol. 35, No. 4, p. C3-223, April 1974.

I. Ladany, C. C. Wang, "Properties of GaP Light-Emitting Diodes Grown on Spinel Substrates," **Solid State Electronics,** Vol. 17, p. 573, 1974.

H. W. Lehmann and R. Widmer, "RF Sputtering of ZnO Films," **J. Vac. Sci. & Tech.,** Vol. II, No. 1, Jan./Feb. 1974.

B. J. Levin and G. G. Weidner, "A Distributed Pin Diode Phaser for Millimeter Wavelengths," **Microwave J.,** Vol. 16, No. 11, p. 42, Nov. 1973.

R. S. Mezrich and W. C. Stewart, "Heterodyne Readout for Read-Write Holographic Memories," **App. Optics,** Vol. 12, No. 11, Nov. 1973.

V. A. Mikenas, H. Kawamoto, H. J. Prager and E. L. Allen Jr., "Advances in High Power S-Band Trapatt Diode Amplifier Design," **Microwave J.** Vol. 17, No. 2, Feb. 1974.

F. H. Nicoll, "Room-Temperature Lasing of CdS Crystals in a Glow Discharge," **IEEE Trans. Electron Devices,** Vol. ED-10, p. 905, Oct. 1973.

F. Okamoto, "Chemical Etchants for the Fabrication of Thin Film Patterns of Silver on Acid- and Base-Sensitive Oxides," **Japan J. Appl. Phys.,** Vol. 13, No. 2, p. 383, 1974.

J. I. Pankove, J. E. Berkeyheiser, and E. A. Miller, "Properties of Zn-doped GaN: 1. Photoluminescence," **J. Appl. Physics,** Vol. 45, No. 3, March 1974.

W. Phillips and D. L. Staebler, "Control of the Fe^{2+} Concentration in Iron-Doped Lithium Nobate," **J. Electronic Materials,** Vol. 3, No. 2, p. 601, 1974.

E. B. Priestley and P. S. Pershan, "Investigation of Nematic Ordering Using Raman Scattering," **Molecular Crystals and Liquid Crystals,** Vol. 23, p. 369, 1973.

W. Rehwald, "The Study of Structural Phase Transitions by Means of Ultrasonic Experiments," **Advances in Physics,** Vol. 22, No. 6, p. 721, Nov. 1973.

R. L. Rodgers, "Charge-Coupled Imager for 525-Line Television," **IEEE Intercon,** New York, New York; 3/26/74 (Session 2).

R. S. Ronen and L. Strauss, "The Silicon-on-Sapphire MOS Tetrode—Some Small-Signal Features, LF to UHF," **IEEE Trans. Electron Devices,** Vol. ED-21, No. 1, p. 100, Jan. 1974.

L. Schiff, "Burst Synchronization of Phase-Locked Loops," **IEEE Communications Tech.,** Vol. COM-21, No. 10, p. 1091, Oct. 1973.

E. J. Schmitt, "The Impact of Surface Wave Technology on Future Military Systems," **Signal,** Vol. 28, No. 3, p. 16, Nov. 1973.

H. S. Sommers, Jr., and D. O. North, "Spontaneous Power and the Coherent State of Injection Lasers," **J. Appl. Phys.,** Vol. 45, No. 4, April 1974.

W. A. Soper, Jr., "AEGIS Weapon System Simulation," **Proc. 1974 Winter Simulation Conf.,** New York, N.Y., Jan. 14-16, 1974.

D. L. Staebler and W. Phillips, "Fe-Doped $LiNbO_3$ for Read-Write Applications," **Appl. Optics,** Vol. 13, No. 4, April 1974.

C. W. Struck and W. H. Fonger, "Recursion Analysis of the Configurational Coordinate Model for Equal Force Constants," **J. Chem. Physics.,** Vol. 60, No. 5, March 1, 1974.

G. A. Swartz, Y. Chiang, C. P. Wen and A. Gonzalez, "Performance of P-type Epitaxial Silicon Millimeter Wave IMPATT Diodes," **IEEE Trans. Electron Devices.,** Vol. ED-21, No. 2, p. 165, Feb. 1974.

N. A. Teixeira and P. Bokros, "Current Status and Activities on Automotive ATE," **Proc. IEEE Intercon,** N.Y.C., March 29, 1974.

J. C. Turbull and W. H. Silvers, "Vacuum Devices," **Sixth International Vacuum Congress,** Kyoto, Japan, March 25-29, 1974.

D. Vilkomerson, "Acoustic Imaging with Thin Annular Apertures," **Acoustical Holography,** Vol. 5, p. 283, Plenum Publishing Corp., N.Y., N.Y.
J. L. Vossen, G. L. Schnable and W. Kern, "Process for Multilevel Metallization," **J. Vac. Sci. & Tech.,** Vol. 11, No. 1, Jan./Feb. 1974.
C. C. Wang, F. C. Dougherty, P. J. Zanzucchi and S. H. McFarlane III, "Epitaxial Growth and Properties of GaAs on Magnesium Aluminate Spinel," **J. Electrochem. Soc.,** Vol. 121, No. 4, April 1974.
G. W. Webb and R. E. Miller, "A Simple 2100 C 600-Watt Tube Furnace," **Rev. Sci. Instr.,** No. 10, Vol. 44, p. 1542, Oct. 1973.
K. P. Weller, A. B. Dreenben, H. L. Davis and W. M. Anderson, "Fabrication and Performance of GaAs p+n Junction and Schottley Barrier Millimeter Impatts," **IEEE Trans. Electron Devices,** Vol. ED-21, No. 1, p. 25, Jan. 1974.
R. Williams, "Image Force Interactions at the Interface Between an Insulator and a Semiconductor," **J. Appl. Phys.,** Vol. 45, No. 3, p. 1239, March 1974.
W. M. Yim and R. J. Paff, "Thermal Expansion of AIN Sapphire, and Silicon," **J. Appl. Phys.,** Vol. 45, No. 3, p. 1456, March 1974.

Patents Issued to RCA Inventors First Quarter 1974

January

B. B. Adams, Jr. Filamentary Cathode Mount and Mounting Method (3,783,327)
P. R. Ahrens High Voltage Protection Circuit (3,789,260)
L. R. Avery Frequency Comparator System (3,783,394)
R. L. Barbin Electron Beam and Deflection Yoke Alignment for Producing Convergence of Plural In-Line Beams (3,789,258)
L. J. Bazin Apparatus for Automatic Color Balancing of Television Camera Signals (3,786,177)
O. E. Bessette High Density Isolated Multi-Channel Magnetic Circuit Transducer (3,789,156)
G. T. Burton Optical Recorder with Intensity Control (3,787,887)
K. K. N. Chang, H. J. Prager and S. Weisbrod Broadband Apparatus Using High Efficiency Avalanche Diodes Operative in the Anomalous Mode (3,784,925)
T. J. Chirstopher Television Deflection Circuit with Low Power Requirement (3,784,857)
R. A. Crane Gas Discharge Device and Electrode for use Therein (3,784,928)
D. P. Dorsey Protection Circuit (3,784,870)
S. S. Eaton, Jr. Control Circuit Employing Digital Techniques for Loads Such As Balance Wheel Motors (3,787,715)
C. J. Fassbender Storage Circuits (3,784,918)
R. P. Fillmore and R. C. Heuner Electronic Firing Circuit (3,788,226)
H. M. Fox Constant Pulse Width Generator (3,783,304)
R. H. Godfrey Methods of Manufacture of Color Picture Tubes (3,788,847)
R. J. Gries Instant-On Circuit for a Television Receiver Offering Independent Filament Voltage Control (3,783,335)
W. A. Grill Method for Depositing Refractory Metals (3,785,862)
W. J. Hannan Playing Back Redundant Holograms by Scanning (3,785,712)
W. A. Hatsell Printing Apparatus (3,787,722)
M. W. Hill Dynamic Convergence Circuits (3,786,300)
W. L. Hurford Fade-to-Black Video Signal Processing Apparatus (3,783,188)
E. E. Janson and M. W. Muterspaugh Switchable Antenna Circuit for Television Providing for Reception of UHF and VHF Signals Utilizing a Single Built-In Monopole Antenna or Two External Antennas (3,787,773)
P. F. Joy, Jr., and D. G. Herzog Thermally-Controlled Crystalline Lasers (3,784,929)
R. Kaysen and F. R. Dimeo Control Unit for an Antenna Rotator (D229,942)
A. L. Limberg Apparatus for Distinguishing Between Various FM Broadcast Multiplex Transmissions (3,787,629)
H. F. Lockwood Method for Depositing a Semiconductor Material on the Substrate from the Liquid Phase (3,785,884)
E. Luedicke Magnetically-Focussed Cathode-Ray Tube Comprising a Tilted Skewed Off-Axis Electron Gun (3,783,326)
E. E. Mayaud and S. Pearlman Method for Printing Negative Tolerance Matrix Screen Structure for a Cathode-Ray Tube (3,788,846)
E. P. McGrogan, Jr. Constant Current Circuit (3,784,844)
A. M. Morrell Methods of Manufacture of Color Picture Tubes (3,788,848)
J. I. Pankove Electroluminescent Semiconductor Device Capable of Emitting Light of Three Different Wavelengths (3,783,353)

J. A. Powell Electron Tube Having Internal Glass Member Coated with Crystalline Ceramic Material (3,787,780)
J. O. Preisig and A. Presser Insulated Dual Gate Field-Effect Transistor Signal Translator Having Means for Reducing Its Sensitivity to Supply Voltage Variations (3,789,246)
A. C. N. Sheng Circuit for Supplying Regulated Power Upon Demand (3,787,757)
T. M. Shrader Cathode-Ray Tube-Yoke Platform—Yoke Combination and Method of Assembling the Combination (3,786,185)
T. O. Stanley High-Density Capacitive Information Records and Playback Apparatus Therefor (3,783,196)
G. A. Swartz and R. E. Chamberlain Encapsulated Semiconductor Device Assembly (3,783,348)
L. P. Thomas Leakage Detector for Determining Possible Shock Hazards to Humans (3,784,903)
F. Van Hekken Color Television Picture Tube Screening Method (3,782,253)
J. A. Van Raalte and V. Christiano Method of Producing a Window Device (3,788,892)
P. K. Weimer Bucket Brigade Scanning of Sensor Array (3,789,240)
C. F. Wheatley, Jr. Semiconductor Amplifier Protection (3,786,364)
C. R. Wronski, W. M. Yim and J. Dresner Photosensitive Charge Storage Electrode Having a Selectively Conducting Protective Layer of Matching Valence Band On Its Surface (3,783,324)

February

E. J. Boleky, III Fabrication of Monolithic Integrated Circuits (3,791,024)
F. J. Campbell Focus-Grill Cathode-Ray Tube Image Reproducer Modulation with Grill Voltage (3,790,845)
D. J. Carlson High Frequency Automatic Gain Control Circuits (3,792,359)
P. L. Chapman Electronic Time Measurement (3,789,600)
A. S. Clorfeine Circuit for Operating an Avalanche Diode in the Anomalous Mode (3,793,539)
R. S. Degenkolb, T. R. Allington, Y. H. Wand and M. Oakes Method of Controlling Resistance Values of Thick-Film Resistors (3,793,717)
I. Gorog System for Recording and Playing Back Color Encoded Holograms (3,790,701)
F. B. Griswold Wide Band Phase-Coherent Self-Calibrating Translation Loop (3,793,594)
P. E. Haferl Pal-Type Color Signal Processing Apparatus (3,794,754)
W. J. Hannan and J. R. Frattarola Double-Sided Holographic Replicas (3,790,245)
R. E. Hanson and H. E. Fineman Signal Sensing and Storage Circuit (3,794,854)
W. F. Hingston Frequency Shift Oscillator Which Avoids the Generation of Transients (RE27924)
J. J. Maley and D. W. Bartch Cathode-Ray Tube Having Conductive Internal Coating Comprised of Iron Oxide and Graphite (3,791,546)
J. T. Mark Means for Ensuring Starting of Gas Laser (3,792,372)
L. S. Napoli and J. J. Hughes Coaxial Magnetic Slug Tuner (3,792,385)
C. S. Oh and E. F. Pasierb Novel Liquid Crystal Electro-Optic Devices (3,792,915)
J. I. Pankove Semiconductor Light Ray Deflector (3,790,853)
E. G. Ramberg Optical System For Orthogonalizing Image Field of Projection Lens (3,790,267)
J. R. Sank Ultradirectional Microphone (3,793,489)
L. E. Smith and D. L. Neal Jitter Immune Transistorized Vertical Deflection Circuit (3,794,877)
C. F. Wheatley, Jr. Differential Amplifier and Bias Circuit (3,790,897)
E. K. Yu Gated Flip-Flop Employing Plural Transistors and Plural Capacitors Cooperating to Minimize Flip-Flop Recovery Time (RE27928)

March

G. A. Alphonse and G. E. Bodeep Process of Making Acousto-Optic Devices (3,798,746)
B. Astle and J. M. Guiot Thick Film Inductor with Ferromagnetic Core (3,798,059)
A. R. Balaban Signal Limiter for Exalted Carrier AM Detector (3,796,963)
J. A. Bauer Pulse Modulation and Detection Communications System (3,796,831)
D. J. Channin Voltage Induced Optical Waveguide Means (3,795,433)
L. S. Cosentino Page Composer Translating Information from Electrical to Optical Form (3,798,620)
R. E. Debrecht and L. S. Napoli Microwave Transmission Line and Devices using Multiple Coplanar Conductors (3,798,575)

E. H. Del Rio Card Stacker having Rotatable Bumper to Stop Card Travel (3,799,539)
P. L. Farina Multi-Indicia Display Device (3,800,231)
J. Gross and W. H. Barkow Self-Converging Color Image Display System (3,800,176)
K. G. Hernqvist Metal Vapor Laser Discharge Device (3,798,846)
M. C. Johnson Power Supply over Voltage Protection System (3,796,919)
A. L. Limberg Multiplex Decoding System (3,798,376)
L. W. Martinson and R. J. Smith Fast Fourier Transform Stage using Floating Point Numbers (3,800,130)
T. R. Mayhew LSI Array and Standard Cells (RE27935)
W. R. McClellan Automatic Gain Control Circuit (3,796,866)
R. M. Mehalso and D. I. Harris Manufacture of Video Discs (3,795,534)
D. K. Morgan and R. C. Heuner Signal Detection in Noisy Transmission Path (3,795,823)
F. G. Nickl and J. F. Schanne Optical Scanning Arrangement and Article useful Therewith (3,796,863)
W. Phillips and D. L. Staebler Holographic Recording on Photochromic Lithium Niobate (3,799,642)
J. H. Pratt Automatic Frequency Control for Pulse Radar and Communication Systems (3,798,552)
J. H. Pratt Doppler Tracker Receiver (3,800,178)
I. Shidlovsky Cathodochromic Cathode Ray Tube and Method for Preparing Cathodochromic Sodalite for said Tube (3,799,881)
J. C. Sondermeyer Amplifier Protection Circuit (3,796,967)
R. K. Waltner and M. N. Norman High Voltage Protection Circuit (3,795,767)
J. A. Weisbecker Computer System with Program-Controlled Program Counters (3,798,615)
D. H. Willis Plural Operating Mode Television Receivers (3,795,762)

AUTHORS

Jan Conradi graduated in 1962 from Queen's University with a B.Sc. in Engineering Physics. He then received an Athlone Fellowship for two years' study in England and spent one year at Imperial College, London and one year at the University of Birmingham where he obtained his M.Sc. in Solid State Electronic Engineering in 1964. In 1968 he received the Ph.D. degree from Simon Fraser University for work on luminescence in single crystals and evaporated thin films of CdS. Dr. Conradi joined RCA Research Laboratories in January 1969, where he has been involved in work on lithium-drifted germanium for gamma ray detectors, planar germanium photodiodes, avalanche multiplication processes in silicon, position sensitive detectors and photodetectors with spectrographic capabilities.

He is a member of the Canadian Association of Physicists.

Asoke K. Ghosh graduated in 1956 from the University of Calcutta with honors in physics. In the same year he entered the Institute of Radio Physics and Electronics, Calcutta for his M.Sc. (Technology) degree receiving that degree in 1959 with Advanced Electronics as special paper. In 1963-64 he obtained his Ph.D. degree in physics for his thesis entitled, "On Some Aspects of Electrical Discharge Phenomena", from Jadavpur University, Calcutta. The content of this thesis covers low frequency and radio frequency breakdown in gases with and without magnetic field, measurement of Townsend's second coefficient in the presence of and absence of magnetic field, and rf conductivity of plasma. During the year 1962-63 Dr. Ghosh worked as a Senior Lecturer in Physics in the University of North Bengal, India. In January 1964, he joined the University of Liverpool as a Department of Scientific and Industrial Research (D.S.I.R.) scholar. During his stay he worked on the measurement of electron energy distribution in Townsend discharge. Dr. Ghosh joined the staff of RCA Limited Research Laboratories in March 1965 where he has worked on the study of electrochemical properties of seeded plasma flow fields, attachment and detachment processes of electronegative gases, plasma diagnostics, properties of turbulent plasma flow fields, radar backscattering from turbulent plasma and re-entry physics (turbulence and antenna breakdown). His present activities involve plasma arc technology, high power gas lasers and its interaction with matter, and atmospheric pollution measuring techniques.

Robert J. McIntyre graduated Summa Cum Laude in Physics from St. Francis Xavier University in 1950. He remained there the following year as Instructor in Physics. In 1951 he commenced graduate studies at Dalhousie University, where he worked in the field of beta-ray spectroscopy, receiving his M.Sc. degree in 1953. He then moved to the University of Virginia where in 1956 he obtained his Ph.D. with a theoretical thesis on the surface energies of monovalent metals. Dr. McIntyre joined the Research Laboratories of RCA Limited in 1956 where he engaged in solid state and semiconductor physics research, in particular studies of infrared photoconductivity, transistor physics, avalanche effects in semiconductor diodes, variable capacitance diodes, photodiodes, radiation detectors, transport properties of semiconductors at low temperatures, and ion-pairing in semiconductors. He was for one year (1958) on loan to Electronics Wing of the Canadian Armament Research and Development Establishment at Valcartier, Quebec. In 1967 he became director of the Semiconductor Electronics Laboratory, where he is directing research programs in advanced semiconductor sensors, microwave integrated circuits, computer-aided design, and acoustic surface wave devices.

He is a member of the Canadian Association of Physicists, and a Senior Member of IEEE.

Lubomyr S. Onyshkevych received a B.E.E. degree from City College of New York in 1955. He worked at the MIT Research Laboratory of Electronics in the area of multi-aperture magnetic logic from 1955 to 1957, receiving a M.S. degree in Electrical Engineering in 1957. In 1957 he joined RCA Laboratories to work in the areas of magnetic logic and memory systems, parametric oscillators, and tunnel diodes. He received an RCA Laboratories Achievement Award in 1959. In 1959 he returned to MIT, where he received the professional E.E. degree in 1962. During the period 1961-1963 he worked at the MIT Lincoln Laboratories, in the field of thin magnetic film memories. In September 1963 he rejoined RCA Laboratories, where he worked in the area of sonic film memories. For this work he received another Achievement Award in 1967, and an IR-100 Award in 1969. Since 1971, he has worked on magnetic bubble device design and construction.

Mr. Onyshkevych is a senior member of the Institute of Electrical and Electronic Engineers, Tau Beta Pi, Sigma Xi, and Eta Kappa Nu.

F. L. Putzrath received a BS degree with high distinction in EE and a BA in Liberal Arts from the State University of Iowa. Mr. Putzrath has 24 years of experience in engineering which has included a broad circuit development background in audio, video, and RF circuits involving tubes, semi-conductors, and magnetic amplifiers. Typical of his many accomplishments was the founding of an engineering team responsible for the abstraction of information from visual and speech patterns using electronic modules and systems organized according to the structure of living Prototype (Bionics). Since 1959, Mr. Putzrath has been engineering leader responsible for the development, design, fabrication, and testing of a series of aerospace video recorders and associated ground equipments. He is presently in charge of several development programs for magnetic recording and alternate data storage techniques such as magnetic domain memories.

Mr. Putzrath is a member of IEEE, Eta Kappa Nu, and Tau Beta Pi.

Rabah Shahbender received the BEE from Cairo University, Cairo, Egypt, the MSEE from Washington University, St. Louis, Missouri, and the PhD from the University of Illinois. From 1946 to 1948, he worked for tne Anglo-Egyptian Oilfields Ltd. in seismic exploration. From 1951 to 1955, he was on the staff of Honeywell Controls Division where he conducted research in the behavior of nonlinear closed loop systems. He joined RCA in Camden in 1955 and worked in the areas of adaptive systems, nonlinear filters, electron beam devices, ultrasonic devices, and airborne fire control systems. He transferred to RCA Laboratories, Princeton, N.J., in 1959, and has been active in the area of digital devices and systems. In 1961 he was appointed Head. Digital Research. He is presently head of the Applied Electronics Research Group, Physical Electronics Research Laboratory. Dr. Shahbender received IR-100 Awards in 1964 and 1969, and RCA Laboratories Achievement Awards in 1960 and 1963. From 1960 to 1966 he was Chairman of the Department of Electronic Physics, at La Salle College, Evening Division. Dr. Shahbender is a Fellow of IEEE, a member of AAAS, Sigma Xi and Eta Kappa Nu, and a Fellow of the University of Illinois.

Fred Sterzer received his B.S. degree in Physics from the College of the City of New York in 1951, and his M.S. and Ph.D. degrees in Physics from New York University in 1952 and 1955, respectively. From 1952 to 1953, he was employed by the Allied Control Corporation in New York. During 1953 and 1954, he was an instructor in Physics at the Newark College of Engineering, Newark N. J., and a research assistant at New York University. Dr. Sterzer joined RCA in 1954 and is now Director of the Microwave Technology Center of the RCA Laboratories in Princeton, N. J. His work has been in the field of microwave spectroscopy, microwave tubes, light modulators and demodulators, and microwave solid state devices.

Dr. Sterzer is a member of Phi Beta Kappa, Sigma Xi, the American Physical Society, and is a Fellow of the IEEE.

Alan Sussman received the bachelors degree in chemistry from Rensselear Polytechnic Institute. Troy, N.Y., and the Ph.D. degree in physical chemistry from Yale University, New Haven, Conn. He then joined the David Sarnoff Research Laboratory (RCA), working on solid state light amplification, organic thin film rectifiers, and liquid crystal display devices. For the latter two projects, he received RCA Achievement Awards. After serving as a technical consultant for Hewlett-Packard, N.E.L.C. San Diego, and Optel Corporation, he joined the RCA Solid State Division in Somerville, N.J., continuing his involvement in liquid-crystal displays.

S. A. Tomkiel received a BEE degree with high honors from Lehigh University in 1972. In July of that year, he joined RCA Recording Systems where he began work in analog/digital design. More recently, he has worked on exploratory magnetic bubble devices, concentrating his efforts on system implementation and device testing. His current assignment is a video processing system intended for longitudinal multitrack recording of digitized color television signals. Mr. Tomkiel is enrolled as a part-time student at the University of Pennsylvania where he is working toward the MSE degree. He is a member of Eta Kappa Nu and Tau Beta Pi honor societies, and the IEEE professional society.

Paul P. Webb received the B. Eng. in Engineering Physics from McGill University in 1955 and was awarded an Athlone Fellowship to study in the United Kingdom from 1955 to 1957. He received the M.Sc. in Engineering from the University of London, and the Diploma of Imperial College in 1957. At the University of London he was engaged in research in semiconductors, with particular interest in the vapor diffusion process for the introduction of impurity layers into germanium. An outcome of the research was the construction of a very high frequency transistor. Mr. Webb joined the Research Laboratories of RCA Limited in February 1958, upon his return to Canada from England. Since then he has been engaged in research on semiconductor devices including the study of voltage breakdown phenomena in diffused silicon p-n junctions and the development of silicon-junction nuclear particle detectors. He was also responsible for the development of lithium-drifted germanium diodes for high-resolution gamma spectroscopy, and was involved in a study of material problems related to their manufacture.

He is presently engaged in a program to develop large-area silicon avalanche photodiodes. He is a member of the IEEE.

James P. Wittke received the M.E. degree from Stevens Institute of Technology, Hoboken, New Jersey in 1949, and the M.A. and Ph.D. degrees in physics from Princeton University, Princeton, N.J. in 1952 and 1955, respectively. His doctoral research was a precision microwave determination of the hyperfine splitting in atomic hydrogen. He was an instructor in physics at Princeton University for one year before joining the technical staff of RCA Laboratories, Princeton, N.J. At RCA he has engaged in paramagnetic resonance and microwave maser studies, in research on optically excited crystal lasers, and in investigations of the motions and properties of impurities in rutile. He has also worked on various classified projects. In 1967 Dr. Wittke was awarded an RCA Fellowship for a year of study abroad, which he spent at the Clarendon Laboratory at Oxford, England. Since then, he has studied the luminescence of heavily doped GaAs, helped develop new infrared-stimulated light emitting phosphors, and worked on the generation of ultra-short laser pulses, using mode-locking techniques. He is currently studying optical fiber communications systems, including making measurements of the characteristics of fast light-emitting diodes and of various low-loss fibers.

Dr. Wittke is a Fellow of the American Physical Society and a member of the Optical Society of America, of IEEE, and of Tau Beta Pi.